# INFORMATION TO USERS

University of Alberta

**Size and Shape of Low Momentum Jet Diffusion Flames in Cross Flow**

by

Adrian Jason Majeski  © 

A thesis submitted to the Faculty of Graduate Studies and Research in partial
fulfillment of the requirements for the degree of Master of Science

Department of Mechanical Engineering

Edmonton, Alberta
Fall 2000

Canada

<div align="center">

University of Alberta

Library Release Form

</div>

**Name of Author:** Adrian Jason Majeski

**Title of Thesis:** Size and Shape of Low Momentum Jet Diffusion Flames in Cross Flow

**Degree:** Master of Science

**Year this Degree Granted:** 2000
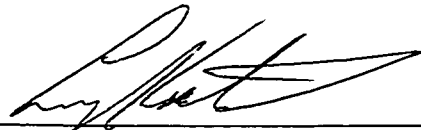
Adrian Jason Majeski
203 Wakina Drive,
Edmonton, Alberta,
Canada T5T 2X6

Date: September 27, 2000

# University of Alberta

## Faculty of Graduate Studies and Research
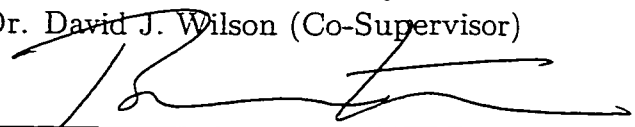
The undersigned certify that they have read, and recommend to the Faculty of Graduate Studies and Research for acceptance, a thesis entitled Size and Shape of Low Momentum Jet Diffusion Flames in Cross Flow submitted by Adrian Jason Majeski in partial fulfillment of the requirements for the degree of Master of Science.

_____
Dr. Larry W. Kostiuk (Supervisor)

_____
Dr. David J. Wilson (Co-Supervisor)

_____
Dr. Brian Fleck

_____
Dr. Suzanne Kresta

Date: ___September 22, 2000___

# Abstract

An objective, quantitative technique for measuring the size and position of a jet diffusion flame in cross flow is presented. A model for predicting the flame length of low momentum jet diffusion flames in cross flow is developed and compared with measurements. Results showed two types of flame trajectory over the test range of jet to cross flow momentum flux ratios: a buoyancy dominated "rising" trajectory and a recirculating wake "trapped" trajectory. A model for flame length, based on diffusion-limited combustion at the surface of a geometrically similar cylindrical flame, showed two regimes characterised by the lengthening or the shortening of the flame with increasing cross flow velocity. The flame length model also successfully correlated both rising and trapped flame length observations.

# Contents

# List of Figures

# Nomenclature

$A$  Area, m$^2$

$C$  Concentration

$C_P$  Pressure coefficient

$d$  Diameter, m

$Fr$  Froude number

$g$  Acceleration due to gravity, 9.81 m/s$^2$

$K$  Constant

$L$  Length, m

$\dot{m}$  Mass flow rate, kg/s

$\dot{m}''_{O_2}$  Mass flux of oxygen, O$_2$, into flame surface, kg/m$^2$s

$M$  Molecular mass, kg/kmol

$P$  Pressure, Pa

$R$  Momentum flux ratio

$r$  Radius, m

$Re$  Reynolds number

$Ri$  Richardson number

$t$  time, s

$U$  Mean horizontal (in the $x$-direction) velocity, m/s

$u'$  Fluctuation from the mean horizontal velocity $U$, m/s

$V$  Mean vertical (in the $y$-direction) velocity, m/s

$v'$  Fluctuation from the mean vertical velocity $V$, m/s

**Greek Symbols**

$\eta$  Efficiency

$\nu$ Kinematic viscosity, m$^2$/s

$\psi$ Shape factor, (kg s/m$^2$)$^{1/2}$

$\rho$ Density, kg/m$^3$

$\tau$ Timescale, s

$\theta$ Angle, degrees

**Subscripts**

$c$ Property of the combustion process

$CL$ Property of the centreline

f Property of the fuel

$f$ Property of the flame

$G$ Geometry

$j$ Property of the jet

$M$ Mixing

O$_2$ Oxygen

$S$ Stoichiometry

$s$ Property of the stack

$t$ Property of the trapped part of the flame

$U$ Attributed to the velocity of the cross flow

*wake* Property of the wake of the stack

$\infty$ Property of the cross flow

# Chapter 1

# Introduction

Flaring is a common practice in the energy industry, used to dispose of unwanted flammable gases. Flaring typically occurs in either of two basic modes. Short duration, high flow rate flares are used to quickly depressurise process units in case of shutdown or emergency. Continuous flares typically operate at much lower flow rates and are used in processing units to destroy gas that leaks past safety valves, or is an unused byproduct of the manufacturing process. Solution gas flaring is a particular case of the continuous flaring process.

The need for solution gas flares arises because during the oil recovery process gases dissolved in the oil come out of solution, as the oil is brought to the surface and its pressure reduced. In most cases, solution gas is recovered for sale or use near the well-site. However, if recovery is not economical and if regulations permit, solution gas is disposed of by flaring. While this appears to be a very specific case, it is important because in 1999 in Alberta, solution gas flaring accounted for about 63 % of the volume of gas flared at about 4500 different sites (AEUB, 2000).

There are several unresolved engineering issues associated with flare design and operation for the widespread practice of solution gas flaring. These issues relate to being able to reliably predict operating parameters such as flame trajectory and

length, combustion efficiency, and the production of toxic species. Brzustowski (1976) pioneered much of the work on flame trajectory and length as well as flare tip design, smoke suppression, and noise. The flame trajectory and length results Brzustowski (1976) produced, have been found to be applicable only in high flow rate flares. Only in the past several years have investigations produced results that can be applied to solution gas (i.e., continuous) flares (e.g., Huang and Chang (1994b); Strosher (1996); Kostiuk et al. (2000)).

The study reported in this thesis addresses flame trajectory and length as they relate to solution gas flares.

## 1.1   Scope of the Investigation

The three most basic variables that affect solution gas flares are the fuel composition and stack exit velocity ($V_j$), and the crosswind speed ($U_\infty$). In practice, the composition of solution gas can vary significantly, including several different hydrocarbons and non-organic compounds such as hydrogen sulfide, even to the point of including liquid droplets (possibly in the form of hydrocarbons or brine). For simplicity, the current study dealt with relatively pure commercial grade fuel gases, combined with an inert diluent. The exit velocities of the actual fuel jets of flares are typically in the range of 0.5 m/s to 6.0 m/s (Kostiuk et al., 2000). The range considered here is $0.5 \leq V_j \leq 2.0$ m/s due to the physical limitations of the laboratory test facility. This falls within the range of the system being modelled. Wind speed averages in Alberta vary between 2 m/s and 5.5 m/s with location (Canadian Meteorological Centre, 1998). The range of $1 \leq U_\infty \leq 14$ m/s covered by this study is a realistic range of conditions.

2

Another parameter that is important to address is that of stack size. Typical solution gas flare stacks are constructed from 4 inch schedule 40 pipe with inner diameter, $d_s = 0.10$ m. The wind tunnel facility limitations prohibit using a stack this large, so scaled down models were used instead. Four stacks with inside diameters ($d_s$) from 10.8 mm to 33.3 mm were used, so the issue of scaling to full size flares now becomes important, and it is addressed in Chapters 2 and 3.

## 1.2 The Fundamental Problem

Having set the scope of the investigation, we now address some of the existing knowledge that will apply to this set of conditions. In its most basic form, the problem at hand is an exothermic reacting jet in a cross flow. A common non-dimensional quantity by which both reacting and non-reacting flows are characterised is the ratio of the momentum flux of the jet to that of the cross flow. This momentum flux ratio ($R$) is given by:

$$R = \frac{\rho_j V_j^2}{\rho_\infty U_\infty^2}$$
(1.2.1)

where $\rho_j$ and $\rho_\infty$ are the densities of the jet and cross flow respectively. It will be used throughout this dissertation to qualify published results with respect to the results presented here. The momentum flux ratios for solution gas flares are typically around or below unity.

A good starting point is to consider non-reacting momentum jets in cross flow. This is a great simplification of the actual flame, but it is reasonable to suggest that conserved factors such as mass flow and momentum flux that affect non-reacting jets will also affect reacting ones.

The non-reacting (or cold) jet in cross flow has been studied extensively from a number of perspectives. Prompted by industry, jet trajectories have been measured (e.g., Pratte and Baines (1967)) to help determine downstream concentration profiles. There are now many models for predicting jet trajectories. One of the more commonly used is that by Briggs (1975) because it is reasonably accurate, yet simple enough to yield analytical results. From this model comes the well accepted $\frac{1}{3}$ and $\frac{2}{3}$ Laws which state that momentum and buoyancy dominated jets and plumes will rise as downstream position, $x^{1/3}$ for momentum jets and $x^{2/3}$ for buoyant plumes.

Another phenomenon observed in non-reacting flows by Sherlock and Stalker (1941) was that at low momentum flux ratios, $R < 2.5$, part of the plume is drawn downwards on the leeward face of the stack. This is known as downwash, and will be shown in the present investigation to be an important mode of flame behaviour.

## 1.3 The Reacting Jet in Cross Flow

Allowing the flow to react introduces several new phenomena and characteristic regimes. Since solution gas flares operate by introducing a jet of fuel to an oxidising environment (i.e., cross flowing air), combustion occurs only after the fuel has mixed by molecular diffusion with a stoichiometric amount of oxygen (air). The discussion will be limited to these non-premixed diffusion flames.

The broadest classification of jet diffusion flames is "lifted" versus "non-lifted". Lifted flames occur when the momentum flux ratio is sufficiently high that the base of the flame sits away from the stack exit. While the mechanism of stability in lifted flames is not yet understood, it was observed by Huang and Chang (1994b) that if the flame was ignited below some critical cross flow velocity ($U_\infty$), then raising $V_j$

may result in the lift-off of the flame base. Conversely, if the fuel jet was ignited above some critical value of $U_\infty$ then the flame would not lift-off, regardless of $V_j$, before blow-off. The latter were called "never-lift" flames. Only non-lifted flames were observed during the course of this investigation. Figure 1.1 illustrates the difference between lifted and non-lifted flames.

Non-lifted flames have been broken down into subcategories. Huang and Chang (1994b) first identified six characteristic flame modes, based on direct visual inspection and short and long term photographs. At a given cross flow velocity, from the lower to upper stability limits (i.e., as a function of increasing $V_j$), Huang and Chang (1994b) denote the flame modes as:*down-washed, flashing, developing, dual, flickering,* and *pre-blowoff.* Figure 1.2 illustrates a representative flame from each mode. *Down-washed flames* are confined to the near-wake region of the stack. *Flashing flames* have a time-varying intermittent flame downstream of the stack, and in *developing flames,* this intermittency stabilises so that a constant axisymmetric flame extends from the wake-stabilised portion, which is shrinking with increased $R$. *Dual-flames* are characterised by a shortening and splitting of the downstream part of the flame. In *flickering flames,* the downstream part of the flame begins to flicker and its cross-stream dimension grows. The wake-stabilised part of the flame continues to shrink, and eventually disappears in *pre-blowoff* flames. These modes were further characterised by temperature and concentration measurements by Huang and Yang (1996).

While these modes are descriptive, it is not the author's opinion that such a detailed attempt to categorise these flames is well founded. Having observed flames over the range of conditions between *flashing* and *flickering,* there are clearly no well defined changes in flame shape which would allow so many classes to be distinguished.

5

At similar conditions, Gollahalli and Nanjundappa (1995) also did *not* observe the repeatable existence and demarcation of these flame modes. The reader is also pointed to Figures 4 and 10 of Huang and Chang (1994b) where the change between the modes can be seen to be gradual, and the boundaries delimiting the different modes overlap, suggesting uncertainty in the application of these limits by Huang and Chang (1994b). An attempt at clarifying these modes was made by Huang and Wang (1999), redefining them in terms of the relative jet and cross flow momentums. Their five modes and range of applicability are: *down-wash* ($R < 0.1$), *cross-flow dominated* ($0.1 < R < 1.6$), *transitional* ($1.6 < R < 3.0$), *jet dominated* ($3.0 < R < 10$), and *strong jet* ($R > 10$). While these limits are certainly clearer than the previous descriptive ranges, the basic problem is that changes in flame structure over this range are not sudden, so a *transitional* flame at high $R$ is not significantly different (if observably different at all) than a low $R$ *jet dominated* flame. For this reason, these descriptive categories will not be used in the current investigation.

Gollahalli and Nanjundappa (1995) adopt a much simpler approach to flame classification and identify only two types of flames: Type I and Type II. The Type I flame exists entirely in the recirculation zone of the stack (similar to the *down-washed flames* discussed above), and the Type II flame has a downstream axisymmetric flame stabilised by the flame in the recirculation zone. If this idea were extended, a third type of flame, Type III, could be identified by the extinction of the wake-trapped part of the flame as illustrated in Figure 1.3. These are the only significant differences in flame structure observed in the present investigation, and seem a more logical choice for flame description. In the present study only Type II and the proposed Type III flames were observed.

Models of reacting jets in cross flows are limited in number, and those that do

exist, apply in regimes where the momentum of the jet dominates its buoyancy (e.g., Escudier (1972); Brzustowski (1975)). Only experimental results exist for the low momentum flux ratio range considered in the present study (i.e., $R \lesssim 1$). Huang and Chang (1994a,b) report flame trajectories and Huang and Chang (1994b); Kostiuk et al. (2000) present results for flame length. These will be discussed further in the text.

## 1.4 Translating Results to Full Scale Conditions

As mentioned previously, an important issue to be dealt with is that of scaling. Since it was not practical to use full size stacks in the facility, stacks $\frac{1}{9}$ to $\frac{1}{3}$ the size were used and a method had to be found to allow the current results to translate to full scale. One way to approach this is to examine flame structure at a variety of smaller scales, in hope of finding a similarity between them.

A multi-scale study was done for non-reacting flows by Smith and Mungal (1998). For the range of source sizes, $d_s = 2.0$ mm to 10 mm, it was found that the trajectory and physical size of the jet and the centreline concentration decay all scale with $\sqrt{R}d_s$. These results were similar to those found by Pratte and Baines (1967) for the trajectory and the cross-stream dimension of a non-reacting, non-buoyant jet.

For reacting flows, Kalghatgi (1983) collapsed flame length and cross-stream dimension of flames for a variety of fuels, a factor of 4 in stack sizes, and a range of momentum flux ratios of $3 < R < 7 \times 10^3$, as a linear function of stack diameter.

Closer to the range of $R$ values of interest, Kostiuk et al. (2000) considered a factor of 3 change in $d_s$ and found that for fixed values of cross flow velocity ($U_\infty$) and fuel jet exit velocity ($V_j$), flame length scales linearly with $d_s$. The cross-stream dimension of

7

the plume of the products of combustion scales with $d_s^{2/3}$ and combustion inefficiency scales with $d_s^{1/3}$. Johnson and Kostiuk (2000) found however, that the visible flame at very small $d_s$ (e.g., $d_s = 5.0\,\text{mm}$, Huang and Chang (1994b)) was noticeably different in colour than at $d_s = 22.1\,\text{mm}$. This may represent a lower limit on the scalability of the visible flame, because all flames in the current investigation scaled quite well with these parameters. It is believed that current results will apply to the full scale case.

## 1.5 Present Results

This dissertation is composed primarily of two papers (Chapters 2 and 3) that have been written for submission to refereed journals dealing with combustion or fluid dynamics. The first paper will be titled "Measuring the Trajectory and Length of a Jet Diffusion Flame in Cross Flow". As suggested by the title, this paper focusses on the experimental methodology developed for measuring the trajectories and lengths of jet diffusion flames in cross flow. Also presented in this paper are some initial results for these parameters and short discussions about them.

The second paper will be titled "Modelling the Length of a Jet Diffusion Flame in Cross Flow". It details the development of a new physical model for the size of the flame, and compares the results of this model with a set of data. A discussion on some phenomenological aspects of flame structure is also presented.

A final chapter (Chapter 4) summarises the results and presents conclusions. A series of appendices offer more technical detail on the experiments and data processing methodology.

# References

AEUB (2000), Upstream Petroleum Industry Flaring Report, 1999, Technical Report ST 2000-60B, Alberta Energy and Utilities Board.

Briggs, G. A. (1975), Plume Rise Predictions, In *Lectures on Air Pollution and Environmental Impact Analyses*, chapter 3, pages 59–111. American Meteorological Society.

Brzustowski, T. A. (1975), The Turbulent Diffusion Flame in a Cross-Wind, *Proceedings of the Fifth Canadian Congress of Applied Mechanics*, pages 605–606.

Brzustowski, T. A. (1976), Flaring in the Energy Industry, *Progress in Energy and Combustion Science*, 2:129–141.

Canadian Meteorological Centre (1998), Canadian Climate Normals 1961-1990, Environment Canada.

Escudier, M. P. (1972), Aerodynamics of a Burning Turbulent Gas Jet in a Crossflow, *Combustion Science and Technology*, 4:293–301.

Gollahalli, S. R., Brzustowski, T. A., and Sullivan, H. F. (1975), Characteristics of a Turbulent Propane Diffusion Flame in a Cross-Wind, *Transactions of the CSME*, 3(4):205–214.

Gollahalli, S. R. and Nanjundappa, B. (1995), Burner Wake Stabilized Gas Jet Flames in Cross-Flow, *Combustion Science and Technology*, 109:327–346.

Huang, R. F. and Chang, J. M. (1994a), Coherent Structure in a Combusting Jet in Crossflow, *AIAA Journal*, 32(6):1120–1125.

Huang, R. F. and Chang, J. M. (1994b), The Stability and Visualized Flame and Flow Structures of a Combusting Jet in Cross Flow, *Combustion and Flame*, 98(3):267–278.

Huang, R. F. and Wang, S. M. (1999), Characteristic Flow Modes of Wake-Stabilized Jet Flames in a Transverse Air Stream, *Combustion and Flame*, 117:59–77.

Huang, R. F. and Yang, M. J. (1996), Thermal and Concentration Fields of Burner-Attached Jet Flames in Cross Flow, *Combustion and Flame*, 105:211–224.

Johnson, M. R. and Kostiuk, L. W. (2000), Efficiencies of Low Momentum Jet Diffusion Flames in Crosswinds, *Combustion and Flame*, In Press.

Kalghatgi, G. T. (1983), The Visible Shape and Size of a Turbulent Hydrocarbon Jet Diffusion Flame in a Cross-wind, *Combustion and Flame*, 52:91–106.

Kostiuk, L. W., Majeski, A. J., Poudenx, P., Johnson, M. R., and Wilson, D. J. (2000), Scaling of Wake-Stabilized Jet Diffusion Flames in a Tansverse Air Stream, *Proceedings of the Combustion Institute*, 28, In Press.

Pratte, B. D. and Baines, W. D. (1967), Profiles of the Round Turbulent Jet in a Cross Flow, *Proceedings of the ASCE, Journal of the Hydraulics Division*, 93:53–64.

Sherlock, R. H. and Stalker, E. A. (1941), A Study of Flow Phenomena in the Wake of Smokestacks, Engineering Research Bulletin 29, University of Michigan.

Smith, S. H. and Mungal, M. G. (1998), Mixing, Structure and Scaling of the Jet in Crossflow, *Journal of Fluid Mechanics*, 357:83–122.

Strosher, M. (1996), Investigation of Flare Gas Emissions in Alberta, Technical report, Alberta Research Council.
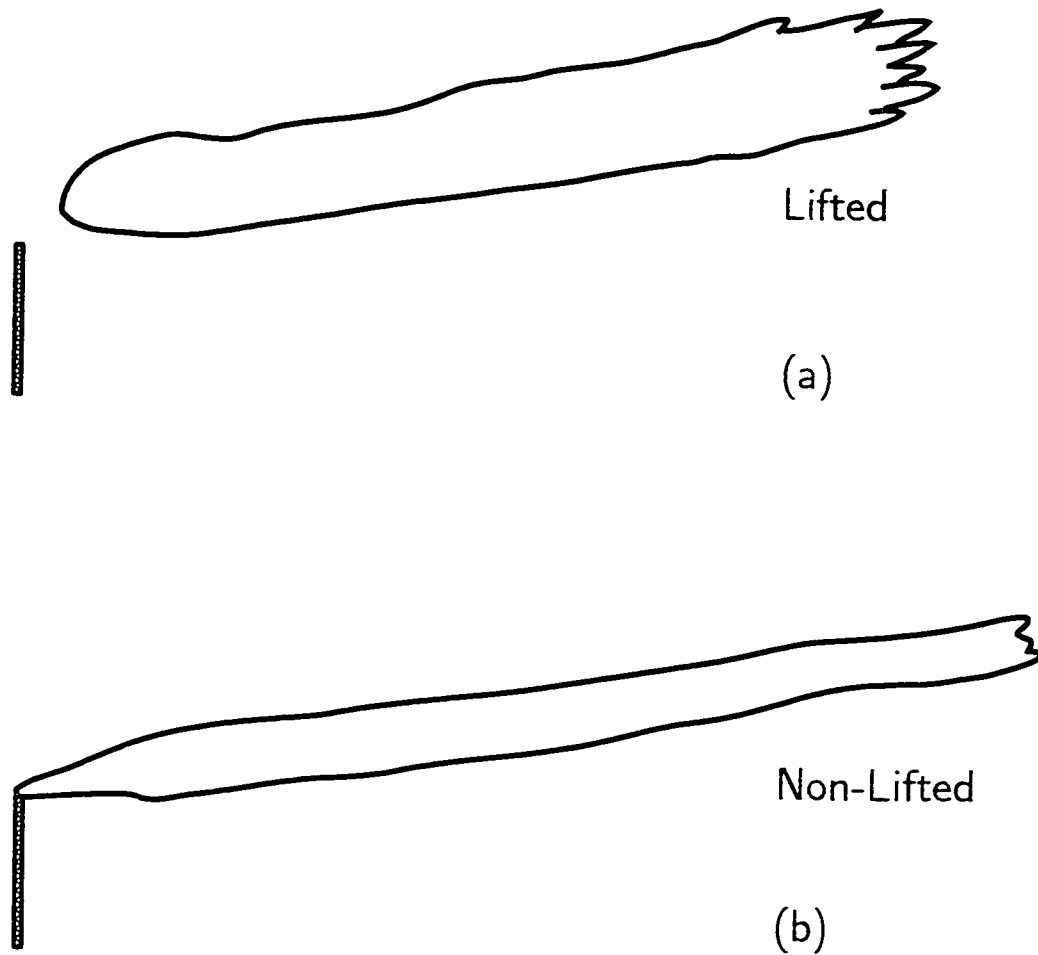
Figure 1.1: Lifted flames (a) have a flame base that is away from the fuel source exit, whereas non-lifted flames (b) have a flame base attached to the source exit. Sketches are based on observations by Gollahalli, Brzustowski and Sullivan (1975).
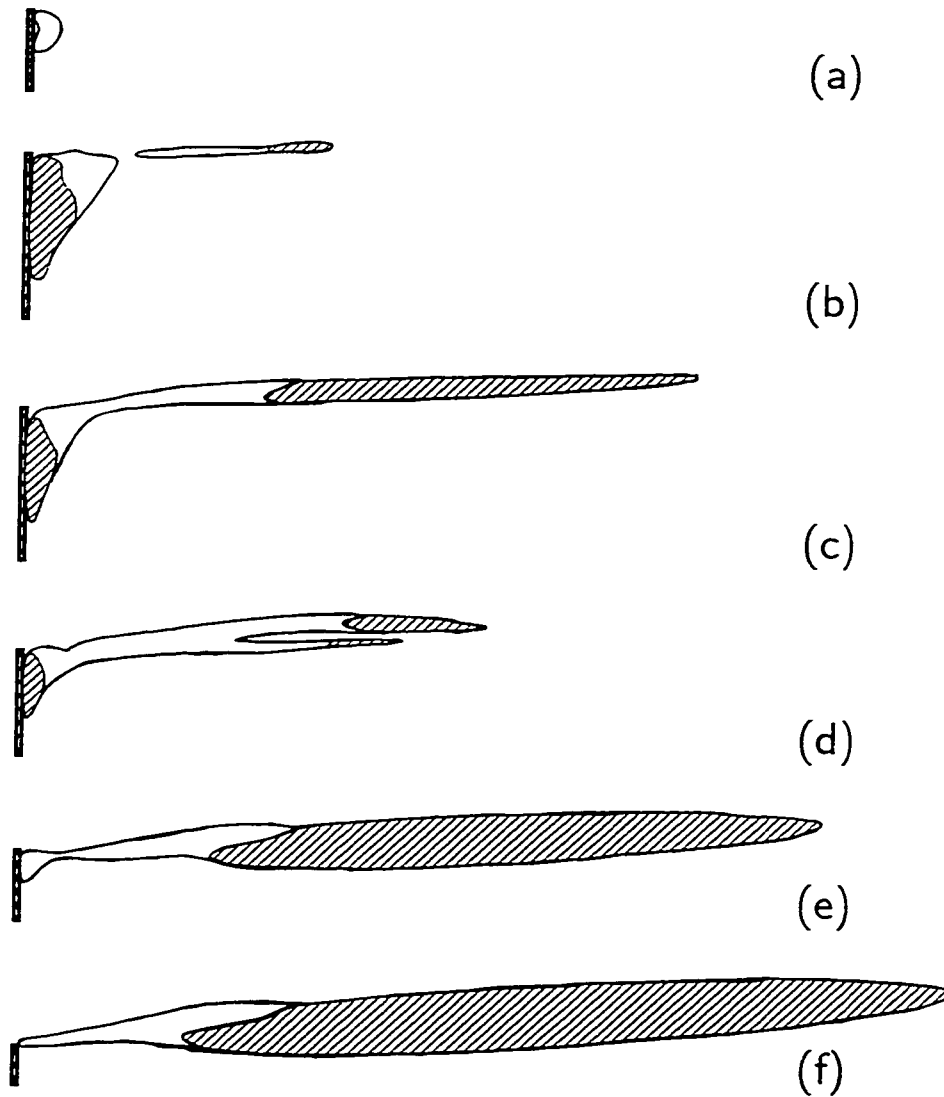
Figure 1.2: The six different flame modes observed by Huang and Chang (1994b). (a) *down-washed*, (b) *flashing*, (c) *developing*, (d) *dual*, (e) *flickering*, and (f) *pre-blowoff*. Hatch marks indicate yellow flame, and no-hatch is blue. Sketches are based on observations by Huang and Chang (1994b).
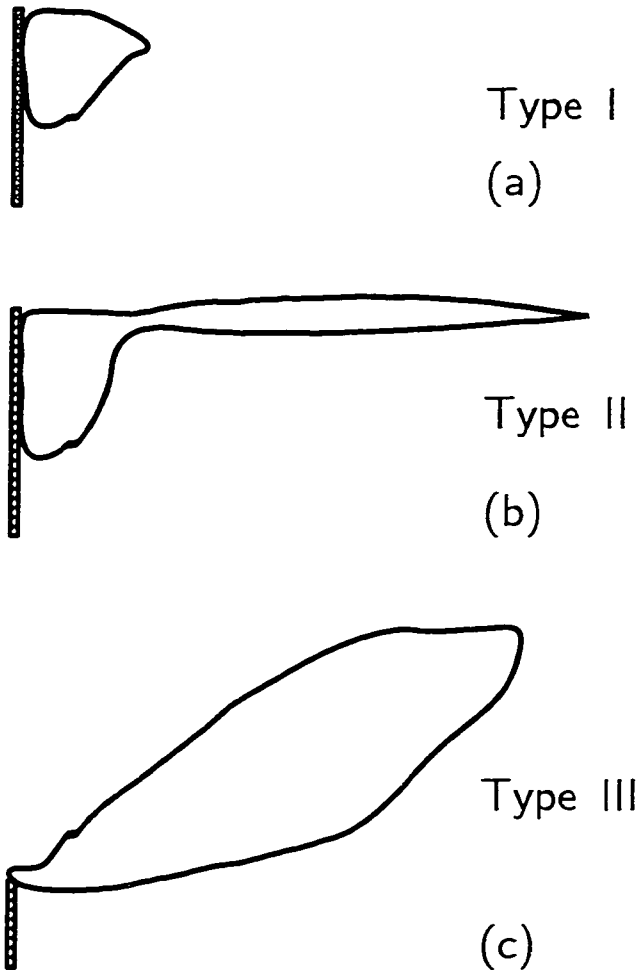
Figure 1.3: Parts (a) and (b) are the Type I and II flames observed by Gollahalli and Nanjundappa (1995). The Type I flame exists entirely in the recirculation region of the stack and the Type II flame has the wake-trapped flame in the recirculation zone which continuously ignites a downstream axisymmetric flame. (c) is an extension of this idea, with a Type III flame described as having no wake-trapped flame. The sketches in (a) and (b) are based on observations by Gollahalli and Nanjundappa (1995).

# Chapter 2

# Measuring the Trajectory and Length of a Jet Diffusion Flame in Cross Flow

## 2.1 Introduction

There are several technical problems involved in measuring the trajectory and length of a jet diffusion flame in cross flow. An appropriate facility must be established, and a methodology developed that will produce results that are accurate and repeatable. Since instantaneous flame trajectory and length are time-dependent fluctuating parameters, it was also necessary to develop a procedure by which to analyse the data obtained to derive statistically relevant results.

The methodology presented here describes an unambiguous way to determine the mean trajectory and length of jet diffusion flames in cross flow. Initial data are presented for a range of momentum flux ratios, $0.014 < R < 1.3$, where $R$ is the momentum flux ratio, defined as

$$R = \frac{\rho_j V_j^2}{\rho_\infty U_\infty^2} \tag{2.1.1}$$

where $\rho_j$ and $\rho_\infty$ are the densities of the cold jet and cross flow respectively, and

$V_j$ and $U_\infty$ are the velocities of the jet and cross flow respectively. This range of momentum flux ratios has not been thoroughly examined in previously published studies.

The purpose of these measurements is to shed light on the physical processes which dominate in establishing the trajectory and length of low momentum jet diffusion flames in relatively high momentum cross flow. The data from these measurements will also assist in the development and validation of models for predicting flame trajectory and length. This is important because no such reliable techniques or models exist that can be applied in this regime of $R$, which is applicable to continuous gas flaring in the energy and petroleum industries.

## 2.2 Review of Relevant Literature

Previous studies of jet diffusion flames in cross flow have reported the size and position of the visible flame, temperature, local velocity, reactant and product concentrations, and combustion efficiency.

### 2.2.1 Flame Trajectory Measurements

Trajectories of jet diffusion flames have been measured by different investigators. The most common method has been to estimate the trajectory from long exposure photographs. Brzustowski, Gollahalli and Sullivan (1975) used this method to determine the trajectories of hydrogen flames, and Gollahalli, Brzustowski and Sullivan (1975) for propane flames. Huang and Chang (1994a,b) took a similar approach, but used schlieren imaging, rather than conventional colour photographs. The resulting trajectory, using schlieren images, was essentially that of the fuel jet and the plume of

15

the hot products of combustion, rather than that of just the visible flame. Both of these methods have the same limitation because they are based on single long exposure photographs. In order to determine the trajectory from these photographs, the geometric centreline had to be determined. This can be difficult to do because the orientation of the coordinate system can bias the results. Examples of this problem are illustrated in Appendix B.

Huang, Savas and Gollahalli (1992) present a discussion on different methods of determining the trajectory of the flame. From the mean velocity field measured by laser Doppler velocimetry, they were able to determine mean streamlines. This is the least ambiguous description of jet trajectory. The other definitions considered were trajectory based on the loci of maxima of velocity or tracer concentration. Local maxima in velocity were only detected near the source and did not follow the visible flame. This was a similar behaviour to that of the streamline in the near field, however the streamline could be traced further downstream, but no conclusions were made as to how well it followed the visible flame in this far field. Without presenting results for trajectory based on concentration maxima, it was concluded that the maxima in tracer concentration would fall below the geometric centreline. This concentration method may be a valid approach, since the visible flame is essentially a surface of constant concentration, and it is the trajectory of the visible flame that is of interest for determining such things as radiation exposure and potential flame impingement on nearby structures.

## 2.2.2   Flame Length Measurements

Burke and Schumann (1928) were the first to report quantitative measurements on diffusion flames, including flame length, in a quiescent environment. Flame lengths of

jet diffusion flames in cross flow have also been reported by several other researchers. The most common method is to take the measurement from an image recorded by a long exposure photograph (Brzustowski, Gollahalli and Sullivan, 1975; Gollahalli, Brzustowski and Sullivan, 1975; Huang and Chang, 1994b; Huang and Wang, 1999). Kalghatgi (1983) used a similar approach in that measurements were taken from recorded images, except that the images were recorded using a colour video system (presumably 30 fps, with shutter speed 1/60 s). A mean flame shape was determined by fitting the frustum of a cone to five randomly chosen *near-instantaneous* images from a data set, and taking the average of these frustums. In some cases the flame shape fluctuated too much for this average to be useful and these cases were not reported within the final data set. Kalghatgi (1983) also stated that for the cases selected for reporting, the measured shape parameters all agreed within 6 % as observed by two independent observers. Kostiuk et al. (2000) presented a new method for measuring flame length. It is essentially an extension of the concept used by Kalghatgi (1983) except that the mean flame shape is determined statistically by the probability of flame occurrence, so it inherently allows for relatively large fluctuations in instantaneous flame size and shape. This method will be discussed further in Section 2.6.

### 2.2.3 Temperature, Velocity, and Concentration Measurements

Other investigators have studied the mean temperature profile of the flame and the plume (Birch et al., 1989; Huang, Savas and Gollahalli, 1992; Gollahalli and Nanjundappa, 1995; Huang and Yang, 1996; Savas, Huang and Gollahalli, 1997; Tacke et al.,

1998; Kostiuk et al., 2000). Kostiuk et al. (2000) demonstrated that the growth of the plume of products in reacting flows follows the same scaling relations as non-reacting flows, suggesting that a good starting point in modelling the trajectories of reacting flows is the associated non-reacting flow situation. Huang, Savas and Gollahalli (1992) showed that the mean temperature surface corresponded to the outline of a long exposure photograph of the visible flame. This approach presents an alternate method for measuring the size and position of the flame.

Velocity measurements made in tandem with temperature measurements by Huang, Savas and Gollahalli (1992) showed that only the lower edge of the visible flame consistently produces a local maximum velocity in the stream-wise direction. They found no correlation between the visible flame and the velocity profile in the vertical direction. Velocity measurements are therefore not useful for defining the visible flame. Velocity measurements made by Huang and Wang (1999) were useful to characterise different modes of flame shape.

Concentration measurements made in tandem with temperature measurements occur more frequently in the literature (Birch et al., 1989; Gollahalli and Nanjundappa, 1995; Huang and Yang, 1996). It was observed by Gollahalli and Nanjundappa (1995) that the concentration profile of carbon dioxide is similar in shape to that of temperature, and oxygen concentration reflects the inverse, as expected. Askari et al. (1990) made concentration measurements on a field size ($d_s = 300\,\text{mm}$) flare to compare with a numerical model at high momentum flux ratios (e.g., $R > 100$).

Savas, Huang and Gollahalli (1997) reported congruent measurements of temperature, velocity, and concentration. Similar results for temperature and concentration of $CO_2$ profiles as found by Gollahalli and Nanjundappa (1995) were observed. Velocity measurements were used to find turbulence shear stress and kinetic energy

18

production along the jet trajectory and at other points in the flame.

## 2.2.4 Efficiency and Soot Measurements

Several investigators have also examined the combustion efficiency of an open flame. This efficiency, $\eta_C$, is defined as the percent conversion of the carbon in the hydrocarbon fuel into carbon dioxide by the flame. Pohl et al. (1986) conducted measurements on free flames from stacks with diameters of 0.076 m to 0.305 m. It was found that combustion efficiency was above 98 % for stable flames. Strosher (1996) carried out field experiments to determine the effect of burning the flame in a crosswind and found combustion efficiencies as low as 64 %. More recently Bourguignon, Johnson and Kostiuk (1999); Johnson and Kostiuk (2000); Kostiuk et al. (2000) have done a thorough investigation of the combustion efficiencies of low momentum ratio (i.e., $0.0069 < R < 3.5$) flames in cross flows. It was found that combustion *inefficiency* $(1 - \eta_C)$ scales with cross flow velocity, $U_\infty$, jet exit velocity, $V_j$, and stack diameter, $d_s$ according to $U_\infty / (V_j d_s)^{1/3}$ (Johnson and Kostiuk, 2000; Kostiuk et al., 2000). The dependency of inefficiency on this parameter is non-linear, remaining small over a wide range of low cross flow velocities, and increases significantly after some critical cross flow velocity. Inefficiency can be an important parameter in trying to model the length and trajectory of the flame because a compositional analysis by Kostiuk et al. (2000) showed that much of the inefficiency is in the form of unburned fuel. It can therefore be expected that flame length will decrease if the flame consumes less fuel as $(1 - \eta_C)$ increases.

Soot measurements have also been made, but not nearly as extensively. Pohl et al. (1986) captured soot coincident with efficiency measurements and found that soot accounts for less than 0.5 % of the unburned hydrocarbons in the product stream at

the test conditions considered. Ellzey et al. (1990) collected soot from propane flames and found that much less soot is produced with cross flowing than co-flowing air. More recently Prybysh, Checkel and Kostiuk (2000) identified selected poly-aromatic hydrocarbons in the soot of wake-stabilised propane flames. Sooting is indirectly important in this study because it is responsible for the high luminosity of the flames currently investigated.

## 2.3 Experimental Facility

The experiments presented in this chapter were conducted at the University of Alberta Flare Research Facility. The three main components that form the experimental facility are the closed-loop wind tunnel, the flare (stack and fuel delivery system), and flame image acquisition system. Figures 2.1 and 2.2 show the arrangement of these units.

### 2.3.1 Closed-Loop Wind Tunnel

The flame shape and trajectory experiments were conducted in a closed-loop wind tunnel, shown in Figure 2.1, that has an internal volume of approximately $350\,\mathrm{m^3}$. The cross flow was produced by a 3 m diameter fan driven by a 150 kW DC motor. The flow was stable and had low turbulence over the range $U_\infty = 1.0\,\mathrm{m/s}$ to 35 m/s. A 6.3:1 area ratio convergent nozzle precedes the test section, which measures 2.44 m wide and 1.17 m tall, to produce a uniform plug flow at the test section. The velocity field in the test section was characterised with a hotwire anemometer, as reported by Johnson and Kostiuk (2000) and is shown in Figure 2.3. They measured the r.m.s stream-wise turbulence intensity as less than 0.4 % at mean speeds $U_\infty > 2\,\mathrm{m/s}$.

This intensity rises to about 1.8 % at lower wind tunnel speeds because of small, low frequency oscillations that have been associated with motor control circuitry, and not turbulence. In the present study, mean cross flow velocity was measured with a pitot-static tube located in the test section at the same downstream position as the stack. The boundary layer at the test section was about 0.15 m, which can be important because it may influence the shape of wake-trapped flames if the stack is too short. The closed nature of the wind tunnel has both advantages and disadvantages. By recirculating the air in the wind tunnel, low but stable cross flow velocities can be achieved because of the momentum of the flow. This required, however, that gas composition in the wind tunnel be monitored and test durations be kept to a minimum to ensure that the combustion process was not adversely affected by the depletion of oxygen in the wind tunnel.

## 2.3.2 The Flare

The fuel stream was introduced perpendicular to the cross flow through round stacks made of commercial steel tubing. These stacks cover the range of inside diameters $d_s = 10.8, 16.7, 22.1$, and 33.3 mm. All tubes were machined to have a constant inside to outside diameter ratio of 0.9. This ratio was chosen because it is the same ratio as a typical full scale flare stack manufactured from 4 inch schedule 40 pipe. A plug, 0.6 inside diameters long, with central orifice (0.3 inside diameters) was placed 8 inside diameters upstream of the stack exit to produce similar mean and turbulence velocity profiles among the stacks. Figure 2.4 shows a diagram of the generalised stack as a function of $d_s$. Characteristic dimensions of all stacks were scaled linearly with $d_s$. The presence of the plug and its location upstream also promotes the establishment of fully developed turbulent flow at the stack exit, similar to what is expected in the full

21

size situation. Figure 2.5 shows the typical velocity profile at the exit of the 22.1 mm stack. A more detailed discussion of the flow inside the stacks is in Appendix A. These profiles were measured by laser Doppler velocimetry.

The length of the stack extending into the test section was adjusted from 0.322 m to 0.880 m, in order to position the flame outside both the ceiling and the floor boundary layers. Sales grade propane, (97.7 % $C_3H_8$, 1.8 % $C_2H_6$, 0.5 % other, molecular weight $M = 44$ kg/kmol) was used as the fuel. Flame measurements were conducted on propane flames because of their high luminosity and strong contrast with background light levels. In some cases the propane fuel was diluted with carbon dioxide, $CO_2$ ($M = 44$ kg/kmol). Since $CO_2$ and propane have the same molecular weight, it was possible to study the effects of reducing the energy density ($J/m^2$) of the flow without changing either the flow rate or the momentum flux ratio. The flow rates of both the fuel and diluent were set by calibrated mass flow controllers.

### 2.3.3 Flame Image Acquisition System

Optical access to the test section was through a 2.09 m wide and 0.867 m tall tempered glass window, see Figure 2.2 (a). Images of the luminous flame were collected by a monochrome Hitachi model KP-M1 CCD (charge-coupled device) video camera with an infrared filter to block radiation below the visible range. The lens was a 12.5 to 75 mm zoom lens with aperture F1.8 to F22 which was set to a focal length of 12.5 mm and an aperture of F1.8. The amount of light incident on the CCD element was controlled by adjustments to the shutter speed of the camera, which could vary from 1/60 s to 1/10000 s. Depending upon the amount of light available, images were collected with a shutter speed of 1/500 s or 1/1000 s in order to obtain *instantaneous* realisations of the flame.

22

The analogue signal from the camera was digitised by a computer video board (Matrox Pulsar version 1.0) to produce images with light intensity resolution of 10-bits (1024 intensity levels available) and spatial resolution of 640 pixels horizontally, and 480 (interlaced) vertically. The camera was placed normal to the cross flow (see Figure 2.2 (b)) to produce a field-of-view measuring 1.8 m by 1.3 m in the plane of the stack, so that pixel resolution was 2.8 mm horizontally and 5.6 mm vertically. Pixel size was determined by focussing the camera in the plane of the stack and grabbing an image of a plus sign (i.e., +) shaped object measuring 1.000 m wide and 0.750 m tall. The length of each arm was measured in pixels and compared to its actual size to calculate the average height and width of a pixel. Since these values were very close (i.e., within 0.37 %), pixels were assumed to be square with a side length found from the geometric mean. This procedure is accurate to 1 pixel in 0.750 m, or 0.37 %. Figures 2.6 (a) and (b) respectively show the odd and even fields of a single frame captured by this system. All greyscale images are presented in inverted colours (i.e., luminous regions appear dark) and as individual fields, with missing rows filled in with values from the next (for odd fields) or previous (for even fields) line.

## 2.4 Experimental Methodology for Collecting Flame Images

For each test condition, 200 full frame images were collected about 0.75 s apart over a period of 2.5 minutes. This number of images was collected to ensure that the mean flame characteristics were well captured (compared to five images by Kalghatgi (1983)). A much faster rate of data collection was possible, however consecutive images were spaced out over a longer period of time as an effort to ensure independence

between them. This concept of independence of the images stems from the time scale associated with the length of the flame. The time scale of a particle of fuel travelling the length of the flame ($\tau_f$) is the length of the flame ($L_f$) divided by the cross flow velocity (i.e., $\tau_f = L_f/U_\infty$). The closely spaced (in time) photographs in Figures 2.6 (a) and (b) show the persistence of structures in the flame. Spacing photographs by 0.75 s, which is the same magnitude as $\tau_f$ helps to ensure that any flow structures are swept away before the next image is taken.

Image collection began approximately 2 minutes after ignition of a steady flow of fuel from the stack. This was done in order to allow time for any preheating effects on the steel stack to come to steady state. These preheating effects occurred predominantly when the flame was trapped in the wake of the stack, and combustion occurred directly on the leeward side of the stack as in Figures 2.7 (c) - (h). Heating by the flame caused the leeward side of the stack to expand, bending the stack tip slightly upwind. This effect was not accounted for in any quantitative way, but the stack was allowed time to come to steady state for consistency and repeatability of the data. Invariably the fuel jet was heated as it flowed through the heated stack prior to its entering the cross flow. This may be a problem for trying to use a parameter like the momentum flux ratio to characterise the flow (e.g., Huang and Wang (1999)) because the density of the fuel stream is not well described by its cold flow conditions. Fortunately, in the present flame length model (Chapter 3), jet density ($\rho_j$) and exit velocity ($V_j$) appear only as a mass flow rate, which is independent of this heating effect.

Experiment duration was kept to a minimum (i.e., less than 5 minutes) because the sealed nature of the wind tunnel adversely affected long experiments. As a test progresses, more of the oxygen resident in the $350\,m^3$ of air in the wind tunnel is

consumed in the reaction with the fuel. One would then expect the length of the flame to increase over the duration of the experiment because more ambient air must be entrained into the fuel plume in order to achieve a stoichiometric mixture. For a 5 minute test at the maximum flow rate of propane of 44 litres per minute, it was calculated that the concentration of $O_2$ in the wind tunnel decreases from 21.0 % to 20.7 %. We therefore do not expect any problems for short tests. The wind tunnel was purged by exhaust fans between experiments to return it to an atmospheric composition.

For particularly long flames, the stack was moved to the upstream position shown in Figure 2.1. Only the tip of the flame was imaged, however the location of stack exit was known relative to the field-of-view, and only the location of the flame tip was required to determine flame length.

## 2.5  Observations of Instantaneous Flame Images

Before continuing discussion on the methods for measuring flame trajectory and flame length, it is illustrative to comment on the general flame structures that are seen in instantaneous flame images. Figure 2.7 shows the change in the size and shape of a $V_j = 1\,\text{m/s}$ jet of commercial grade propane issuing from the $d_s = 22.1\,\text{mm}$ stack as cross flow velocity is increased.

### 2.5.1  The Effects of a Cross Flow

Several observations can be made about the size and position of the flame as cross flow velocity is increased. The first thing that is noticed is in the trajectory of the flame. In Figure 2.7 (a), where $R = 1.3$, the trajectory of the flame appears to bend

upward along its entire length as buoyancy is added during combustion. As the cross flow velocity is increased any apparent curvature in the trajectory is reduced until the flame is essentially straight, at a fixed angle from the stack centreline. With further increases to $U_\infty$ this angle approaches 90° from the vertical, at which point the flame is perpendicular to the stack axis.

It is also observed that at a low momentum flux ratio (i.e., between $R = 0.37$ and $R = 0.16$) fuel becomes trapped and burned directly in the wake of the stack, and this phenomenon becomes more pronounced as $U_\infty$ increases ($R$ decreases). Sherlock and Stalker (1941) observed significant downwash in non-reacting momentum dominated jets when the momentum flux ratio, $R$, was less than 2.5. Since the entire range of conditions considered falls into this category, the term *wake-stabilised* will be used to describe a flame in which some part of the combustion is occurring directly on the leeward side of the stack. With the growth of the wake-stabilised region, the structure of the flame can be divided into 3 parts as described by Gollahalli and Nanjundappa (1995) and Johnson and Kostiuk (2000): the *planar recirculation zone* that is attached to the stack, the *axisymmetric tail*, and a *transition* zone between the two. As $U_\infty$ is increased, the length of the planar region grows along the length of the stack (Figures 2.7 (c)-(h)) because of the low pressure zone in the wake of the stack.

In the series of tests discussed here, the boundary layer on the stack is laminar because the external Reynolds number ($Re_d = U_\infty d_s / \nu_\infty$) remains below the critical Reynolds number of $300 \times 10^3$ over the range of cross flow velocities considered. It actually falls into the region where the coefficient of drag due to pressure,

$$C_P = \frac{P_{wake} - P_\infty}{\frac{1}{2}\rho_\infty U_\infty^2} \qquad (2.5.1)$$

26

where $P_{wake}$ and $P_\infty$ are the wake and free stream pressures respectively, is relatively constant ($10^3 < Re < 300 \times 10^3$). It can be shown that in this regime, the difference in pressure between the free stream and the wake of the stack increases as $U_\infty^2$, so it is expected that with increasing $U_\infty$, more fuel will be drawn into this near-wake region and will react there.

The same monotonic behaviour is not observed in the length of the axisymmetric tail of the flame. Figures 2.7 (a)-(e) show that the flame tail becomes narrower and longer as $U_\infty$ increases. This coupling in the changes of both dimensions can be expected, because in a diffusion flame the rate of fuel consumption is directly related to the surface area of the flame. Since the rate of fuel supply is held constant, it is expected that the flame surface area is also constant, providing that the rate of air entrainment to the flame surface does not vary significantly.

A different trend for the flame tail is observed in Figures 2.7 (e)-(h). After an apparent local maximum in flame length around cross flow velocity of 4 to 5 m/s, the flame begins to shorten with increasing wind speed, but it does not widen as one might expect. At these cross flow speeds, however, the planar wake-stabilised region is growing, so this may compensate in part for the lost surface area in the axisymmetric tail. A more extensive discussion of lengthening and shortening mechanisms is presented in Chapter 3.

The transition region between the planar wake circulation zone and the axisymmetric tail described by Gollahalli and Nanjundappa (1995), and observed by Huang and Chang (1994a) and Johnson and Kostiuk (2000), can be clearly seen developing in Figures 2.7 (e)-(h). Since the images are presented in greyscale, the blue colour that is characteristic of this transition region appears as a light shade of grey, relative to the highly luminous yellow of the recirculation zone and tail that appears as black.

27

Between cross flow velocities of 2 and 6 m/s ($0.37 \leq R \leq 0.039$) coherent structures similar to those observed by Huang, Savas and Gollahalli (1992) and Huang and Chang (1994a) can be distinguished on the upper surface of the flame. These structures may be caused by the vertical shear ($dU/dy$) of the cross flow as the higher speed (in the $x$-direction) cross flow mixes with the lower speed (in the $x$-direction) plume. The $dU/dy$ shear creates vortices in the $-z$-direction (into the page), which are predicted to grow linearly with $x$ in a non-reacting flow (Panton, 1998). As $U_\infty$ increases further, the strength of the vortices increase and so does their growth rate. Eventually the vortices become large enough to penetrate the entire plume, resulting in separate independent pockets of flame that are advected at nearly the cross flow speed. This fragmentation of the flame is clearly visible in Figures 2.7 (e)-(h). The location where the flame is first fully penetrated (i.e., the onset of fragmentation) moves toward the stack as wind speed is increased. The underside of the flame is relatively smooth compared to the top. A likely reason for this is that the pair of counter-rotating vortices (Smith and Mungal, 1998) are smoothing the bottom surface as they draw fluid up into the plume.

## 2.5.2   Scaling With $V_j$ and $d_s$

Figure 2.8 shows the effects of varying both jet exit velocity and stack size on single instantaneous flame images. In Figure 2.8 (b), the jet exit velocity is half of that in Figure 2.8 (a). Several observations can be made about the differences and similarities in the shapes and sizes of the two flames. Overall, the length and width of the flame are both less in Figure 2.8 (b) compared to Figure 2.8 (a). This could be expected because only half as much fuel is being consumed in Figure 2.8 (b) compared to Figure 2.8 (a). The length (along the stack) of the wake-stabilised region appears to

be the same in Figures 2.8 (a) and (b), suggesting that as long as there is a minimum amount of fuel present, the size of the wake-stabilised zone is dominated by the flow-field around the stack (i.e., it is dependent on cross-flow velocity, $U_\infty$, and stack outer diameter). There are also differences in the axisymmetric tails of the flames. The coherent structures on the upper surface of the flame are much more prominent in Figure 2.8 (b) or, conversely, the mixing layer eddies are eroding the fuel plume much more in Figure 2.8 (b) than in Figure 2.8 (a). The onset of fragmentation is also much nearer the stack in Figure 2.8 (b). These observations are consistent with a shear mechanism $(dU/dy)$ being responsible for the erosion and fragmentation of the flame because the size of the flame should scale with fuel flow rate, and a smaller flame will respond to the effects of this erosion more dramatically.

The differences between Figures 2.8 (c) and (a) are comparable to those between Figures 2.8 (b) and (a). Again the flame is shorter and narrower, because only a quarter as much fuel is being supplied in Figure 2.8 (c) compared to Figure 2.8 (a). The size of the planar wake-stabilised zone is noticeably different than that in Figure 2.8 (a), unlike in Figure 2.8 (b) where the size of the wake-stabilised zone is similar to Figure 2.8 (a). The length along the stack is about half that in Figures 2.8 (a) and (b); this supports the supposition that the size and shape of the planar wake-stabilised region is independent of fuel flow rate, and depends only on cross flow velocity, $U_\infty$ and stack outer diameter. The onset of fragmentation in Figure 2.8 (c) is also much nearer the stack than in Figure 2.8 (a), and even than in Figure 2.8 (b), again supporting the shear mechanism for fragmentation.

## 2.5.3 Unsteady Flame Size and Shape

One important issue about the size and shape of the flame, which has been dealt with only in passing (Kalghatgi, 1983) is the unsteadiness of the flame. Figure 2.9 shows three randomly sampled images from a single data set (i.e., same experimental conditions). Here, the flame length varies about 20 % in Figures 2.9 (b) and (c), compared with Figure 2.9 (a). This unsteadiness raises some important questions when trying to describe the shape and size of the flame. Clearly individual realisations of the flame are adequate only in making general observations. Long exposure photographs are an attempt to compensate for this phenomenon, however a single long exposure photograph does not provide any insight into the distribution of the occurrences of these different shapes, nor can the imaged flame itself really be considered a mean shape, since portions of the flame with different luminosity will be weighted differently. Also, a long exposure image does not provide any information that can be used to determine the trajectory in any way other than a geometric centreline.

Birch et al. (1989) also reported the effects of flame intermittency, when light-back positions (i.e., the down or cross-stream location at which a cold-jet can be ignited to from a stable flame, instead of simply blowing out) were found to have mean fuel concentrations much lower (about half) than the lower flammability limit, implying large concentration fluctuations in the fuel-air mixing layer.

## 2.6 Processing Instantaneous Images to Produce the Mean Flame Image

The unsteadiness of flame shape observed in Figure 2.9 suggests that flame shape would best be described statistically. Flame measurements in the present study were based on a mean flame shape that was produced from the 200 independent images collected for each test condition. A threshold was applied to the recorded pixel intensity of each image, identifying flame as those points with an intensity equal to or greater than the threshold. The choice of threshold was based on whether trajectory or length was being measured, as described in the following sections. It is important to note that despite the common use of flame luminosity as a measure of flame position, it is inherently a line-of-sight technique. As a result, all information across the width of the plume is integrated. Figure 2.10 shows the resulting binary image, when a threshold of 188 is applied to Figure 2.6 (a), where the measured intensity ranged from 11 in the background to the 10-bit overload level of 1023 in the luminous core of the flame. The mean flame is obtained by summing the binary images and normalising them by the number of images in the series. Pixel intensity in these mean flame images, then represents the probability of finding flame at that location. Figure 2.11 shows one of these mean flame images with contours bounding the regions where the probability of flame occurrence is greater than 90 %, 50 %,and 10 %.

### 2.6.1 Calculating Flame Trajectory

Several techniques that have been used to describe jet and flame trajectory were discussed earlier. Since the primary focus of this research is the luminous flame, flame

trajectory was determined from the flame images collected, rather than from temperature or concentration fields. A new definition for flame trajectory was developed based on the probability of finding flame at a given point.

Figure 2.11 shows that the shape of the flame can be described as regions of flame occurrence probability. Similar to concentration (Johnston and Wilson, 1997) or velocity (Huang, Savas and Gollahalli, 1992) profiles, where trajectory follows the maxima, the probability method follows the downwind *peaks* of flame occurrence probability. By fitting a parametric $2^{nd}$ order polynomial to the rightmost portion of the probability contour, the point of maximum curvature, or *peak*, can be found (see Appendix C). The trajectory is then defined as the set of line segments that join the peaks of the contours. Figure 2.11 shows the trajectory defined in this way using the peaks at every percentile from 90 % to 10 %.

Defining flame trajectory in this way (i.e., based upon a mean scalar field) offers a couple of advantages over the other possible alternative for an imaged flame, which is a geometric centreline. Firstly, this definition has more physical meaning than simply taking slices of the mean flame image; because at a given distance from the stack exit, or origin, one is choosing the point most likely to be flame and this is a natural point to follow if you want to pursue the flame over its full extent. The second advantage is that the reported trajectory is not subject to the biases often present in geometric centrelines, due to the orientation of the coordinate system, and even in some cases, the probability contour for which the centreline is being found. A more detailed discussion is found in Appendix B. The primary limitation of the present definition is that its use is limited to the far field of the flame. In the near field, the flame is present all of the time over a wide region and the most probable contour is not defined. Flame trajectory, as defined here, should be sufficient to determine if

trends exist in the data.

The choice of threshold to produce the mean flame image was done separately for each image. For each image the distribution of pixels with respect to intensity was determined. From this pdf of intensity it was possible to determine the imaged flame area by the number of pixels with intensity equal to or greater than a given threshold. Since there is only one feature of interest (i.e., the flame), above a certain threshold, only the flame is present in the binary image. However since the apparent size of the flame is itself a function of the threshold, it was necessary to optimise the choice of threshold so that the size of the flame is as close as possible to its actual size. Since the images have a high contrast between background and feature, there is a relatively small range of thresholds over which the apparent flame area decreases dramatically as the background drops out and only the feature is left, so a threshold is chosen shortly after this rapid change in order to maximise flame area, without including any of the background. The threshold was then chosen as the point at which the marginal change in flame area is less than 1.0 %. A more detailed discussion is found in Appendix C.

A second method for describing the position of the flame, is the flame angle, $\theta_f$, shown in Figure 2.12. It is the angle from the vertical (along the stack axis) of a chord connecting the centreline of the stack exit to the flame tip, which is discussed in more detail in the next section. Similar to the definition used by Kalghatgi (1983), the flame angle, $\theta_f$ is sufficient for describing the position of the tip of the flame, once its length ($L_f$) is known.

## 2.6.2 Calculating Flame Length

Having defined the probability trajectory as described above, a natural choice for the location of the flame tip is somewhere along this trajectory. Figure 2.12 shows that the tip of the flame was defined at the 10th percentile contour. This point was chosen because it is the longest flame length that is still reasonably statistically representative of the population of flame shapes collected. Similar trends in flame length, as a function of wind speed or jet exit velocity, are observed when the tip is defined at other contours. See Appendix C for further details. Also shown on Figure 2.12 is that the flame length $(L_f)$ is defined as the linear distance between the flame tip and the centreline of the stack exit. Flame length was defined as this linear distance, instead of the curvilinear distance along the trajectory, because the trajectory is ill-defined near the stack (see Section 2.6.1).

To minimise the ambiguity of threshold choice, camera shutter and aperture settings, and different flame luminosities, flame lengths reported here have been extrapolated to a threshold of zero counts, which removes the effect of the threshold used to filter out the background luminosity. This flame length was determined by calculating flame lengths at several different thresholds for each test condition and projecting back to a threshold of zero. It should be noted, however, that the length of the flame does not drastically change over the range of thresholds considered (e.g., a typical change in flame length over the entire range of thresholds considered is about 5 %). This shows the relative insensitivity of the 10 % contour length to camera settings and flame luminosity as long as some minimum critical amount of light reaches the CCD element. See Appendix C for further details.

Considering the mean flame image as defined here offers advantages over the traditional method of measuring the flame length from a long exposure photograph,

34

see Gollahalli, Brzustowski and Sullivan (1975); Kalghatgi (1983); Huang and Chang (1994b). The projection back to zero intensity negates the effects of varying flame luminosity whereas the long-time exposure is essentially a luminosity weighted mean, where the threshold or the probability of flame occurrence at the tip of the flame is unknown. The present method also provides a true statistical distribution of flame occurrence probability.

### 2.6.3 Length of the Wake-Trapped Part of the Flame

A second characteristic length of the flame is the stack downwash distance, $L_t$, of the trapped part of the flame. Figure 2.12 defines this length. The length of the wake-trapped part of the flame ($L_t$) is important because it can help designers of the flare stack make sure that not only is the stack long enough, but that appropriate materials are used if it is expected that part of the stack will be regularly subjected to direct flame impingement. The length $L_t$ is extrapolated in a similar way to that of flame length, $L_f$, except that no curve is fitted to find $L_t$, rather it is simply taken to be the lowest point of flame at the 10 % probability of occurrence.

## 2.7 Measured Flame Trajectory and Length

### 2.7.1 Flame Trajectory

Over the range of conditions considered, $V_j = 1$ m/s and $1$ m/s $\leq U_\infty \leq 10$ m/s, two types of trajectory were observed. Figures 2.11 and 2.13 show them as a function of $U_\infty$. Because of the relatively large buoyancy associated with the hot products of combustion, as compared with jet momentum or even the buoyancy of the jet itself,

it can be expected that three factors will have significant impact on the trajectory of the flame. These are the buoyancy of the hot products of combustion, the momentum of the cross flow, and the suction pressure of the near wake of the stack. The relative magnitudes of these factors are then visible in the trajectories of the flames. As wind speed is increased from Figure 2.13 (a) to Figure 2.11 to Figure 2.13 (b) it was observed that the slope of the trajectory decreases as the momentum of the cross flow increases. From this, Figure 2.13 (a) represents a buoyancy dominated "rising" trajectory, and Figure 2.13 (b) represents a wake "trapped", cross flow momentum dominated trajectory.

A second method for defining flame trajectory, the flame angle $\theta_f$, was also briefly discussed. Figure 2.14 shows some initial results for flame angle as a function of cross flow velocity. From these data, it appears that flame angle approaches 90° asymptotically, similar to the results of Kalghatgi (1983) which were at much higher velocity ratios. Further investigation is required to determine if $\theta_f = 90°$ is an asymptote, because non-reacting plumes with centreline trajectories below the source exit were observed by Johnston and Wilson (1997).

## 2.7.2 Flame Length Variation with Cross Flow Velocity

Figure 2.15 shows the calculated flame length as a function of cross flow velocity. Over the range of crosswind speeds considered, flame length is *not* monotonic with cross flow velocity. Initially, the effect of increasing cross flow velocity is to increase flame length. This continues until a local maximum in flame length is reached, and after this point, further increases in cross flow velocity cause the length of the flame to decrease. In the present study, it was chosen to describe this as a local maximum because the literature (e.g. Brzustowski, Gollahalli and Sullivan (1975); Gollahalli, Brzustowski

and Sullivan (1975); Kalghatgi (1983)) suggests that there is a maximum in flame length at zero cross flow velocity (i.e., the quiescent case). Similar non-monotonic behaviour in flame length was also observed for propane flames by Kostiuk et al. (2000) at the same experimental conditions, Gollahalli, Brzustowski and Sullivan (1975) for momentum flux ratios, $R > 40$ and Huang and Chang (1994b) for $R < 5$, and for hydrogen flames by Brzustowski, Gollahalli and Sullivan (1975) for $R > 18$. Competing mechanisms for this phenomena are: stretching of the flame by the cross flow and shrinking of the flame due to fragmentation of the flame, growth of the wake-trapped part of the flame, and a decrease in combustion efficiency. More details are presented in Chapter 3. It is interesting to note, that the change in flame length is nearly linear over the range of cross flow speeds considered. When compared with the two best fit lines in Figure 2.15, the data have a root-mean-square departure of only 3 % from linearity. The maximum flame length is predicted to occur at $U_\infty = 4.4\,\text{m/s}$ and the rate of flame length increase is about 50 % greater than its rate of decrease.

This initial discussion was done to demonstrate that measurements using this method are sufficiently clearly defined to resolve small changes ($\sim$ 5 %) in flame length. A more detailed study and model to predict these results are presented in Chapter 3.

### 2.7.3   Length of the Wake Trapped Part of the Flame

As illustrated in Figure 2.7, an increasing amount of fuel was trapped and burned in the recirculating wake of the stack as cross flow velocity was increased. Since there have been no published results regarding the size of this wake trapped flame, it was necessary to turn to the non-reacting flow case as a first attempt at learning about the processes which control the size of the wake trapped part of the flame. Briggs

(1976) used the data of Sherlock and Stalker (1941) and existing photographic data to determine that the non-dimensional downwash distance ($y_d/d_s$) of a non-reacting jet is proportional to the jet to cross flow velocity ratio. Johnston and Wilson (1997) extended this relationship to different fluids by replacing the jet to cross flow velocity ratio with a modified density weighted velocity ratio, resulting in

$$\frac{y_d}{d_s} = 2.0 \left( 1.5 - \sqrt{\alpha_m R} \right) \tag{2.7.1}$$

where $\alpha_m$ is a correction for non-uniform jet exit velocity profile and is typically taken to have a value of unity. Using this correlation as a basis, it can be expected that the length of the wake trapped part of the flame will be a function of the momentum flux ratio. Figure 2.16 shows the length of the wake trapped part of the flame, for the data in Figure 2.15, as a function of $\sqrt{R}$ as in Equation 2.7.1. The result is not linear as in Equation 2.7.1, but rather has the form

$$\frac{L_t}{d_s} = 13.6 \ln \left( \frac{1}{R^{1/2}} \right) - 1.29 \tag{2.7.2}$$

The onset of wake trapping is expected to occur at about $R = 1$. Further investigation with different fuel flow rates is required to determine if buoyancy has any effect on this result.

## 2.8  Summary and Conclusions

A methodology has been presented for acquiring *instantaneous* images of a jet diffusion flame in cross flow. Based on a mean flame image produced from many individual images of the flame at the same test conditions, statistical definitions for flame trajectory and flame length were also developed. Initial results show that the size and shape of the flame change with cross flow velocity, jet exit velocity, and the diameter

of the stack. Using the probability of occurrence definition for flame trajectory, two distinct shapes were observed. These correspond with a buoyancy dominated "rising" plume and a cross flow momentum dominated "trapped" plume. Initial results for flame length show that initially the flame length of a $V_j = 1$ m/s jet of propane issuing from a $d_s = 22.1$ mm increases with cross flow velocity at a rate (i.e., $\partial L_f / \partial U_\infty$) of 0.17 s to a local maximum length of about 1.6 m at $U_\infty = 4.4$ m/s and then decreases at a rate of 0.11 s. Extrapolating flame lengths to an intensity of zero counts resulted in consistent and repeatable (within about 5 %) data. Wake trapping of the flame occurs at about $R = 1$, and the length of the wake trapped part of the flame is related to $R$ by

$$\frac{L_t}{d_s} = 13.6 \ln \left( \frac{1}{R^{1/2}} \right) - 1.29 \tag{2.8.1}$$

# References

Askari, A., Bullman, S. J., Fairweather, M., and Swaffield, F. (1990), The Concentration Field of a Turbulent Jet in a Cross-Wind, *Combustion Science and Technology*, 73:463–478.

Birch, A. D., Brown, D. R., Fairweather, M., and Hargrave, G. K. (1989), An Experimental Study of a Turbulent Natural Gas Jet in a Cross-Flow, *Combustion Science and Technology*, 66:217–232.

Bourguignon, E., Johnson, M. R., and Kostiuk, L. W. (1999), The Use of a Closed-Loop Wind Tunnel for Measuring the Combustion Efficiency of Flames in a Cross Flow, *Combustion and Flame*, 119:319–334.

Briggs, G. A. (1976), Estimation of Downwash Effects, In Noll, K. E. and Davis, W. T., editors, *Power Generation: Air Pollution Monitoring and Control*, chapter 6, pages 65–70. Ann Arbor Science Publishers, Inc.

Brzustowski, T. A., Gollahalli, S. R., and Sullivan, H. F. (1975), The Turbulent Hydrogen Diffusion Flame in a Cross-Wind, *Combustion Science and Technology*, 11:29–33.

Burke, S. P. and Schumann, T. E. W. (1928), Diffusion Flames, *Proceedings of the Combustion Institute*, 1:2–11.

Ellzey, J. L., Berbee, J. G., Tay, Z. F., and Foster, D. E. (1990), Total Soot Yield from a Propane Diffusion Flame in Cross-Flow, *Combustion Science and Technology*, 71:41–52.

Gollahalli, S. R., Brzustowski, T. A., and Sullivan, H. F. (1975), Characteristics of a Turbulent Propane Diffusion Flame in a Cross-Wind, *Transactions of the CSME*, 3(4):205–214.

Gollahalli, S. R. and Nanjundappa, B. (1995), Burner Wake Stabilized Gas Jet Flames in Cross-Flow, *Combustion Science and Technology*, 109:327–346.

Huang, R. F. and Chang, J. M. (1994a), Coherent Structure in a Combusting Jet in Crossflow, *AIAA Journal*, 32(6):1120–1125.

Huang, R. F. and Chang, J. M. (1994b), The Stability and Visualized Flame and Flow Structures of a Combusting Jet in Cross Flow, *Combustion and Flame*, 98(3):267–278.

Huang, R. F., Savas, O., and Gollahalli, S. R. (1992), Flow Field in the Near Burner Region of a Partially Lifted Turbulent Gas Jet Flame in Cross Flow, In Cho, P. and Quintiere, J., editors, *Heat and Mass Transfer in Fire and Combustion Systems*, volume 223 of *HTD*, pages 105–110, The Winter Annual Meeting of the ASME. The American Society of Mechanical Engineers.

Huang, R. F. and Wang, S. M. (1999), Characteristic Flow Modes of Wake-Stabilized Jet Flames in a Transverse Air Stream, *Combustion and Flame*, 117:59–77.

Huang, R. F. and Yang, M. J. (1996), Thermal and Concentration Fields of Burner-Attached Jet Flames in Cross Flow, *Combustion and Flame*, 105:211–224.

Johnson, M. R. and Kostiuk, L. W. (2000), Efficiencies of Low Momentum Jet Diffusion Flames in Crosswinds, *Combustion and Flame*, In Press.

Johnston, C. R. and Wilson, D. J. (1997), A Vortex Pair Model for Plume Downwash into Stack Wakes, *Atmospheric Environment*, 31(1):13–20.

Kalghatgi, G. T. (1983), The Visible Shape and Size of a Turbulent Hydrocarbon Jet Diffusion Flame in a Cross-wind, *Combustion and Flame*, 52:91–106.

Kostiuk, L. W., Majeski, A. J., Poudenx, P., Johnson, M. R., and Wilson, D. J. (2000), Scaling of Wake-Stabilized Jet Diffusion Flames in a Tansverse Air Stream, *Proceedings of the Combustion Institute*, 28, In Press.

Panton, R. L. (1998), *Incompressible Flow*, chapter 3, pages 745–792, John Wiley & Sons, Inc., 2nd edition.

Pohl, J. H., Lee, J., Payne, R., and Tichenor, B. A. (1986), Combustion Efficiency of Flares, *Combustion Science and Technology*, 50:217–231.

Prybysh, R. A., Checkel, M. D., and Kostiuk, L. W. (2000), Collection and Analysis of Toxic Emissions from Continuous Flares, In *2000 Spring Technical Meeting*. The Combustion Institute Canadian Section.

Savas, O., Huang, R. F., and Gollahalli, S. R. (1997), Structure of the Flow Field of a Nonpremixed Gas Jet Flame in Cross-Flow, *Journal of Energy Resources Technology - Transactions of the ASME*, 119:137–144.

Sherlock, R. H. and Stalker, E. A. (1941), A Study of Flow Phenomena in the Wake of Smokestacks, Engineering Research Bulletin 29, University of Michigan.

Smith, S. H. and Mungal, M. G. (1998), Mixing, Structure and Scaling of the Jet in Crossflow, *Journal of Fluid Mechanics*, 357:83–122.

Strosher, M. (1996), Investigation of Flare Gas Emissions in Alberta, Technical report, Alberta Research Council.

Tacke, M. M., Geyer, D., Hassel, E. P., and Janicka, J. (1998), A Detailed Investigation of the Stabilization Point of Lifted Turbulent Diffusion Flames, *Proceedings of the Combustion Institute*, 27:1157–1167.
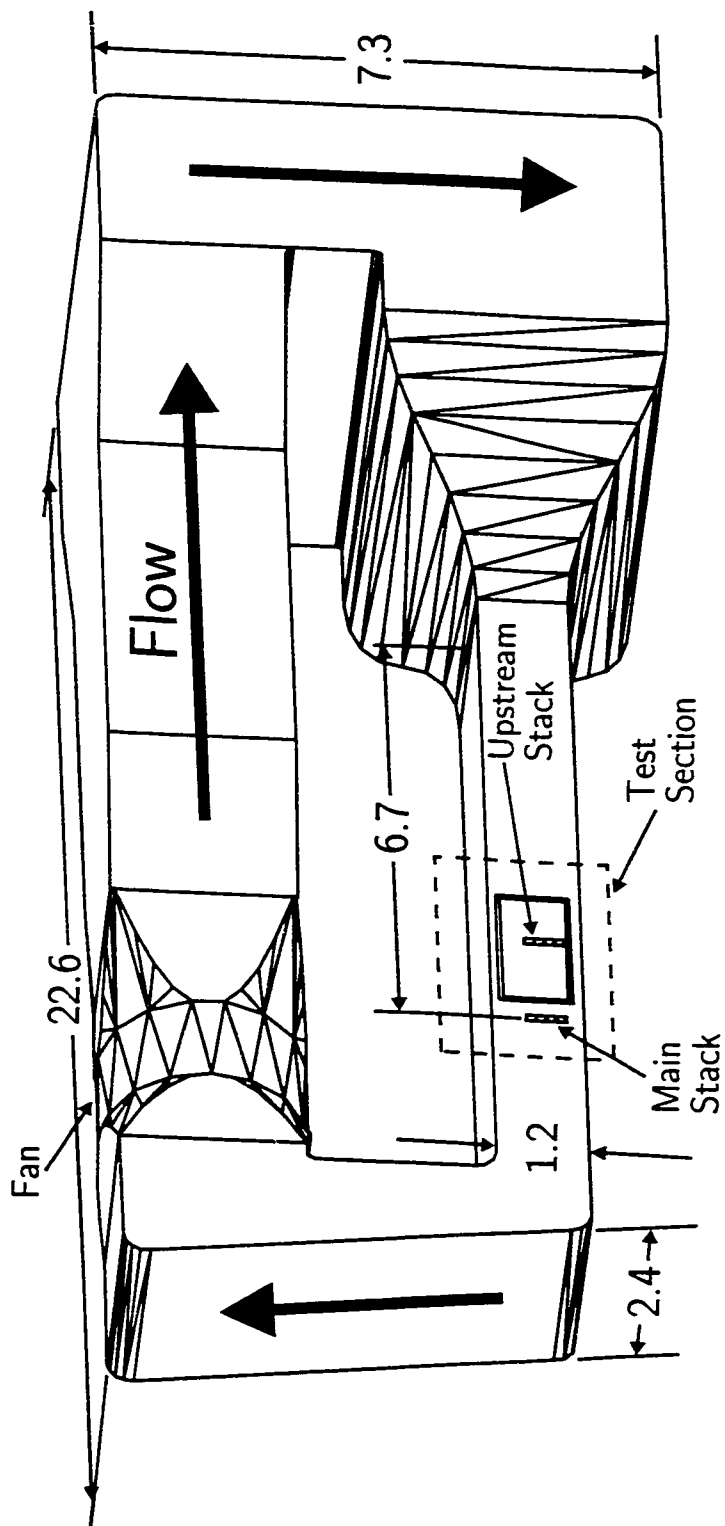
Figure 2.1: Schematic of the closed-loop Combustion Wind Tunnel facility. Only one stack is present during experiments. Figures 2.2 (a) and (b) show the side and end views of the test section. All dimensions are in metres.

43
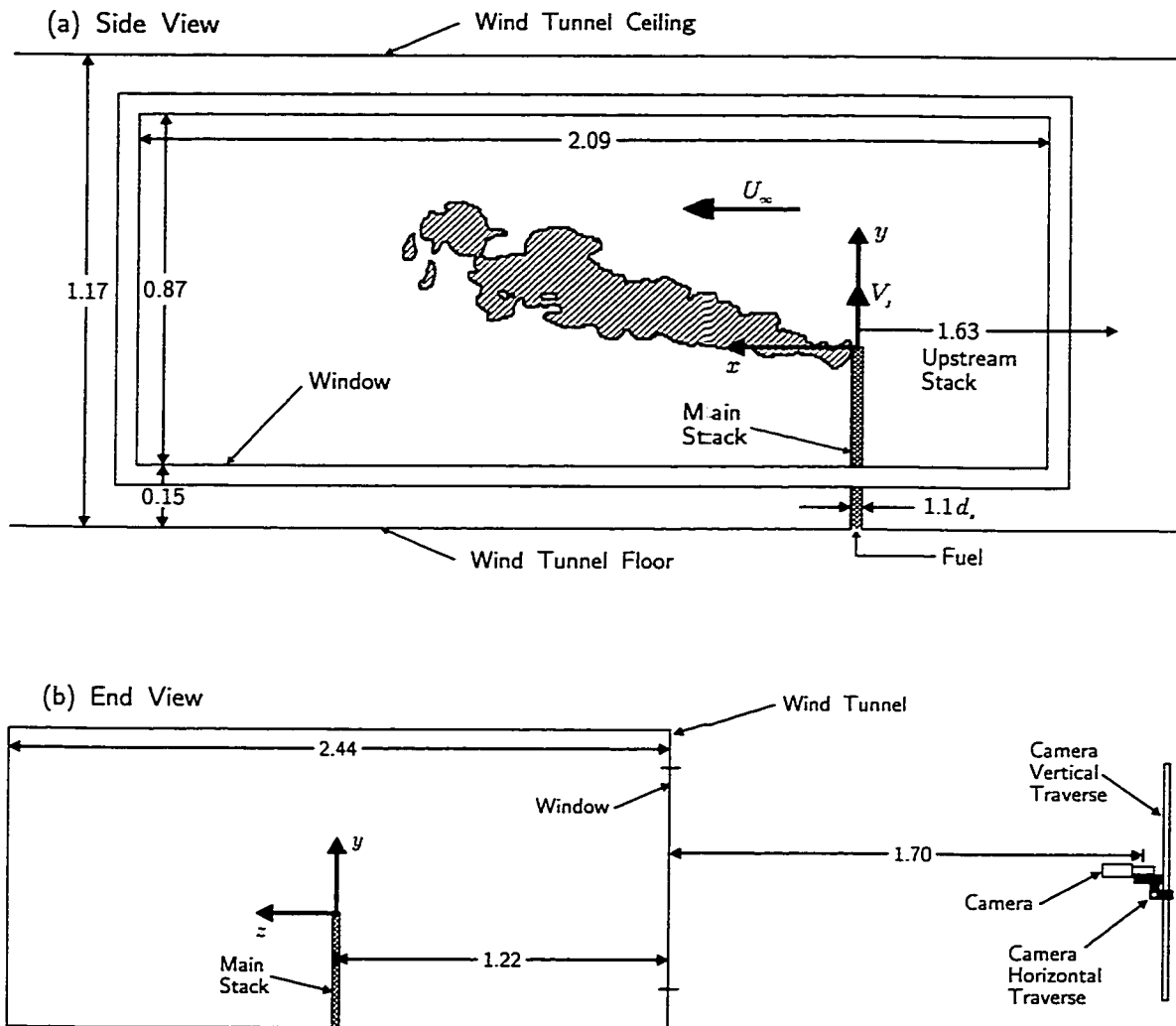
Figure 2.2: Side (a) and end (b) views of the Combustion Wind Tunnel (Figure 2.1) test section. The origin of the coordinate system is at the stack exit centreline. All dimensions are in metres.
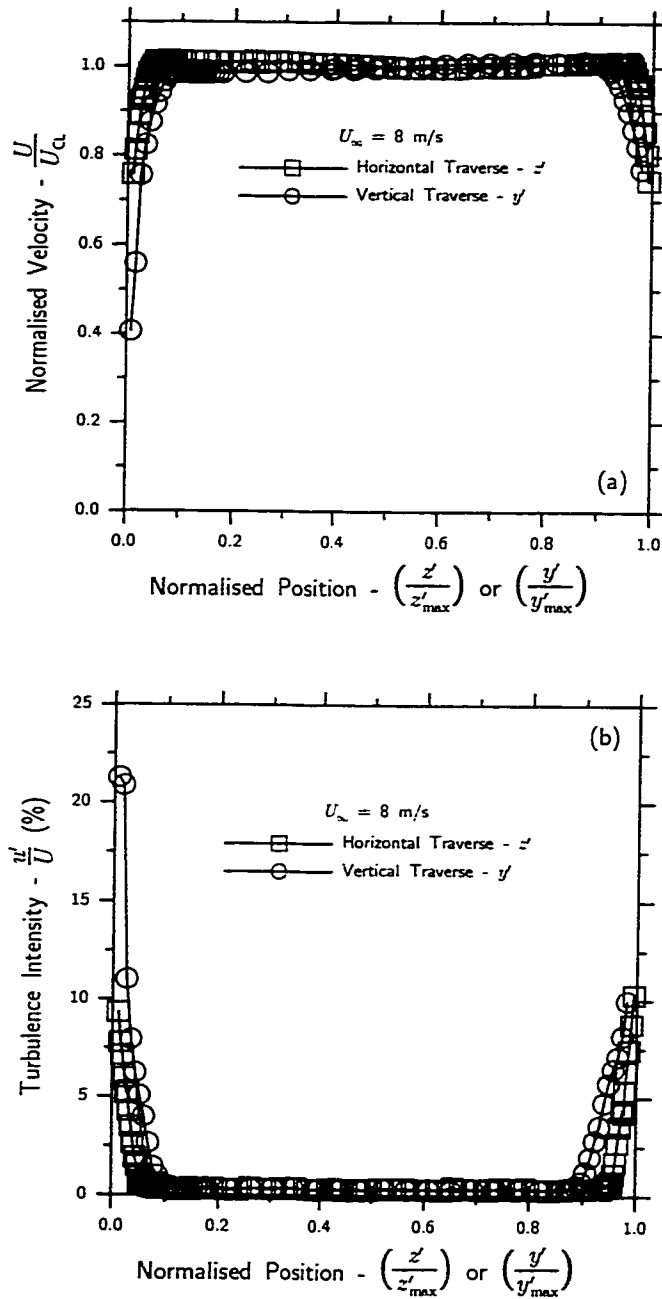
Figure 2.3: Horizontal and vertical mean velocity (a) and turbulence intensity (b) profiles across the test section for an 8 m/s cross flow velocity. Results show a nearly uniform plug flow with little ($<$ 0.4 %) turbulence. $y'$ and $z'$ define the relation to the extreme bottom and camera side of the wind tunnel test section.
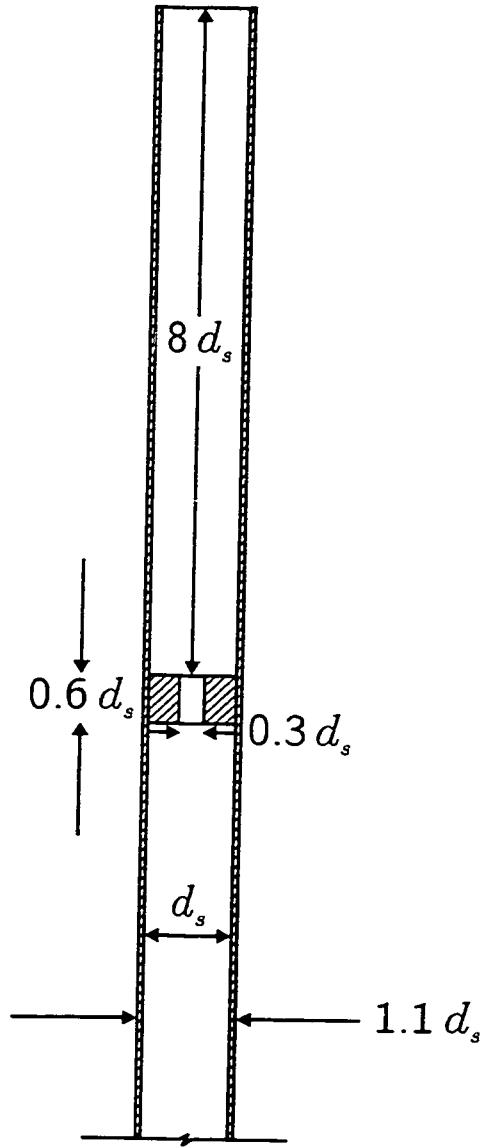
Figure 2.4: Generalised schematic of the stack (burner tube). All model stacks are scaled the same way with their respective inner diameters (i.e., for $d_s$ = 10.8, 22.1, 16.7, and 33.3 mm).
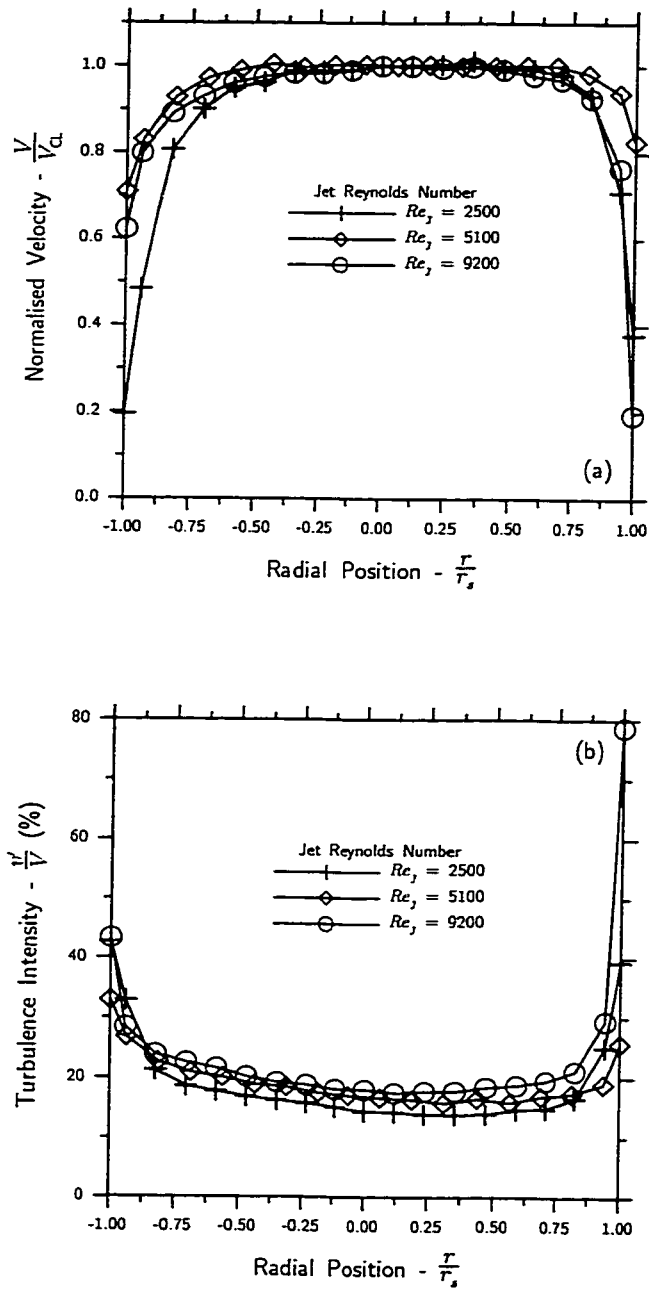
Figure 2.5: The velocity (a) and turbulence (b) profiles at the exit of the 22.1 mm stack with jet Reynolds Number ($Re_j = V_j d_s / \nu_j$) matching to 0.50, 1.0, and 1.8 m/s propane jets. Profiles were done with natural gas as the working fluid, and show a near top-hat turbulent velocity profile at the exit of the stack. Other stacks show similar results, see Appendix A.
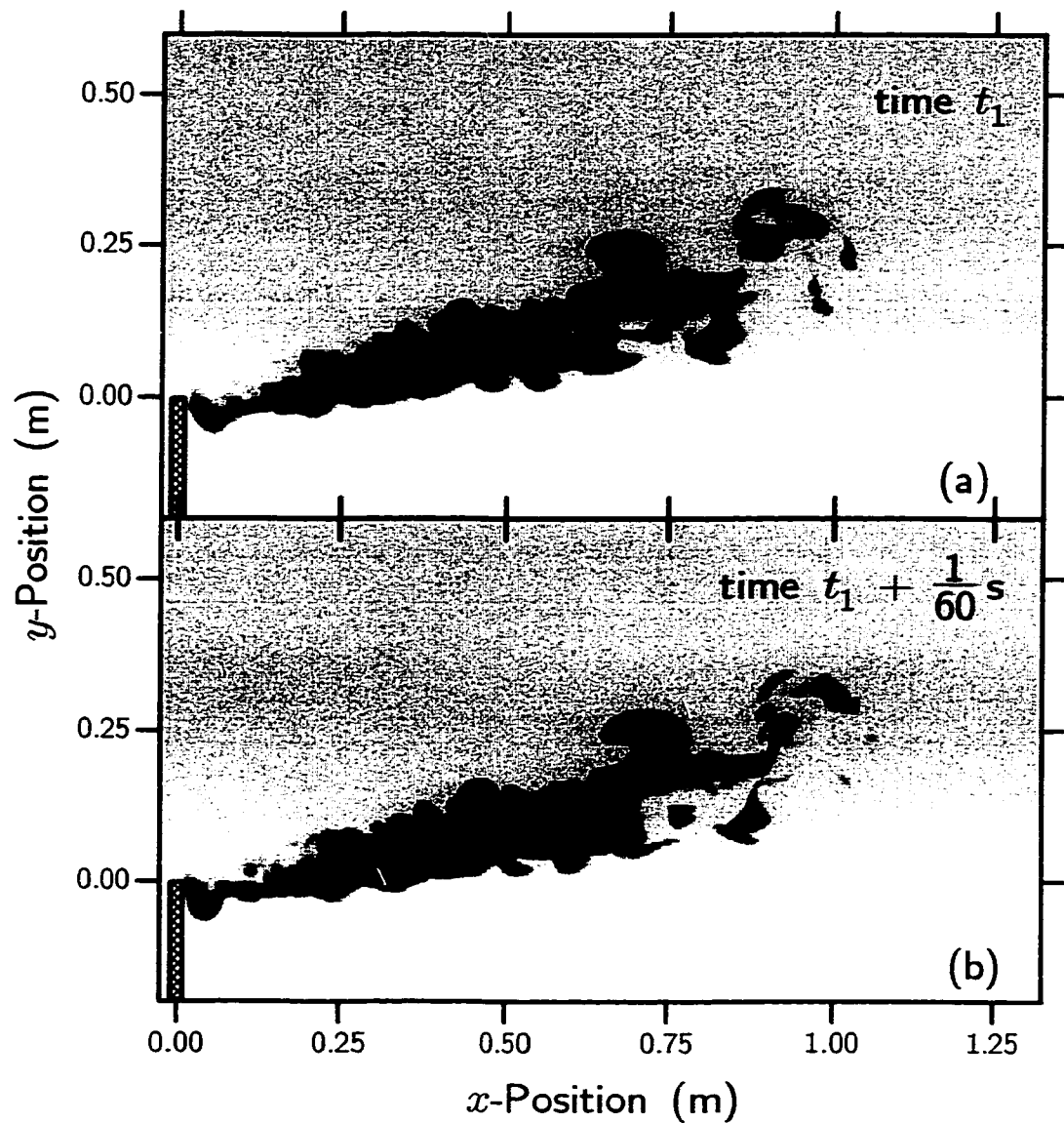
Figure 2.6: These images show the two images extracted from a single interlaced frame and the persistence of the flame shape between them; both have been downsampled to 8-bits for viewing and the colour inverted so that flame appears dark. (b) was captured $1/60$ s after (a). The images were interpolated by filling in missing horizontal lines with the next (odd fields) or previous (even fields) line. This, and all following images were flipped horizontally so that $x$ increases from left to right, as opposed to how the camera views the flame (Figure 2.2).

48
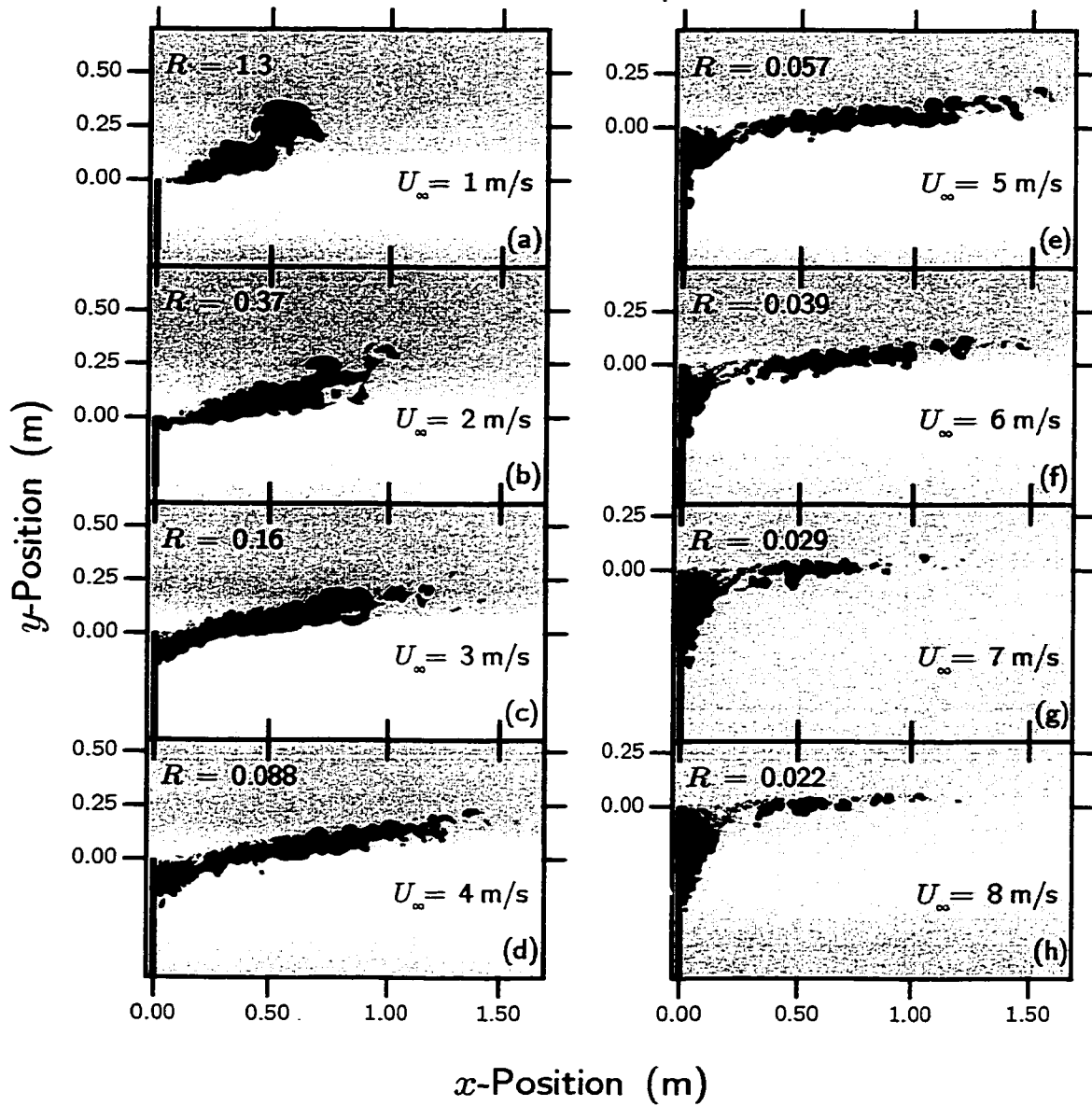
Figure 2.7: The change in flame shape with increasing wind speed for a $V_j = 1\,\text{m/s}$ jet of propane from the $d_s = 22.1\,\text{mm}$ stack (jet Reynolds number $Re_j = 5 \times 10^3$).
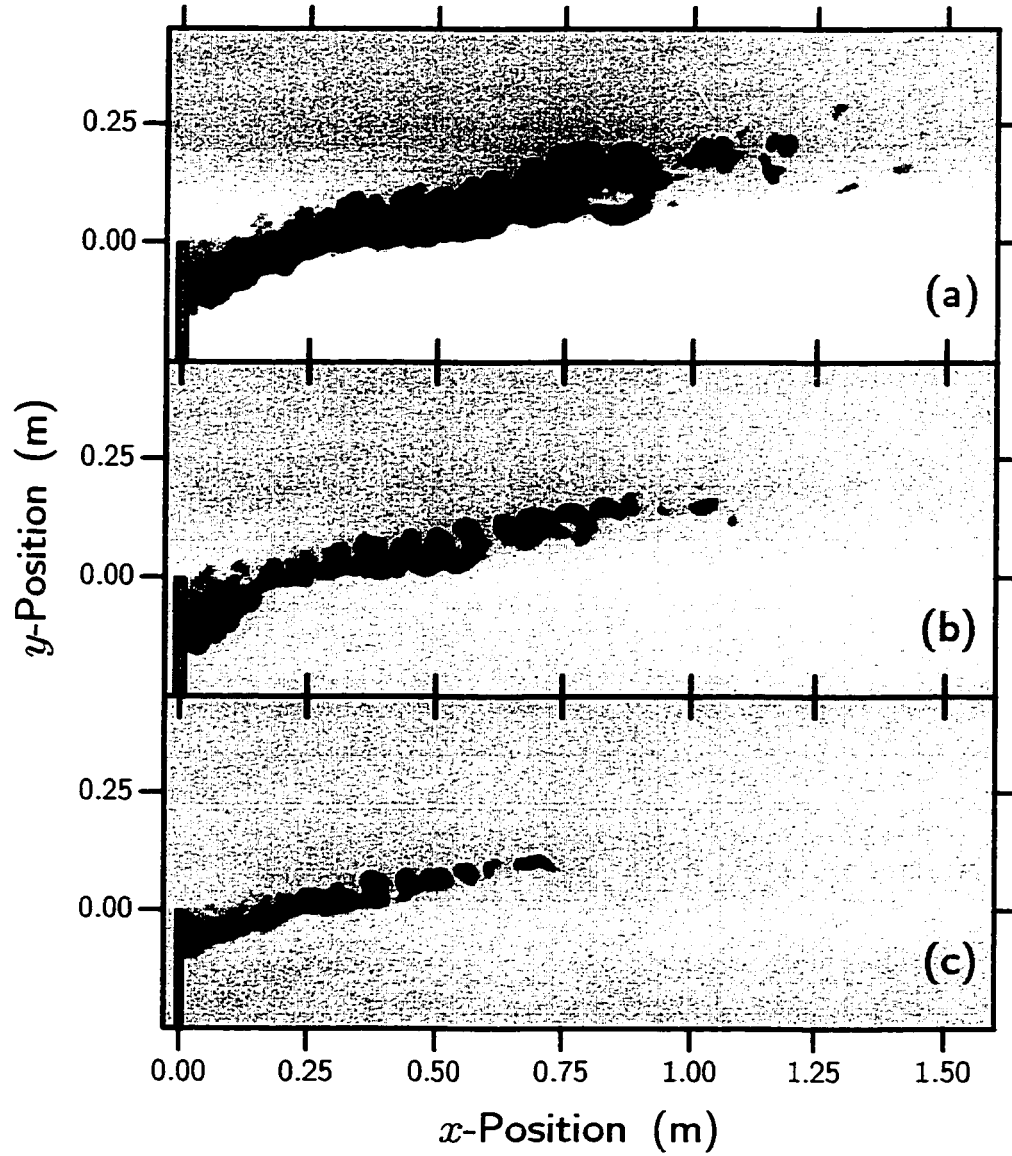
Figure 2.8: Scaling the flame shape with $V_j$ and $d_s$: (a) The *control* case: $U_\infty = 3\,\mathrm{m/s}, V_j = 1\,\mathrm{m/s}, d_s = 22.1\,\mathrm{mm}$;(b) same as *control* with $V_j = 0.5\,\mathrm{m/s}$ :(c) same as *control* with $d_s = 10.8\,\mathrm{mm}$.
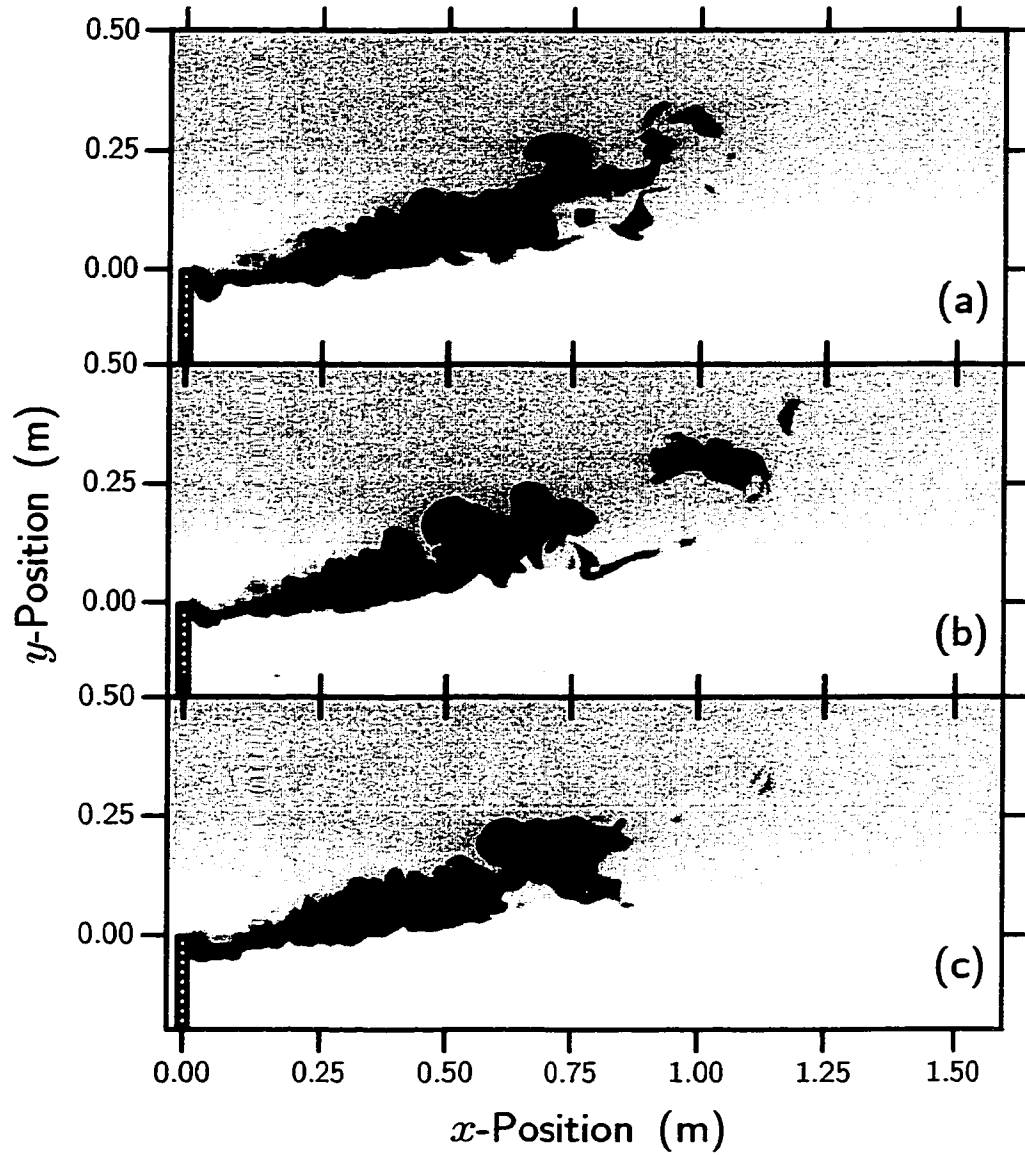
Figure 2.9: Three fields taken from the same data set as those in Figure 2.6. The flame shape and size vary significantly with time despite the fact that test conditions are constant.

51
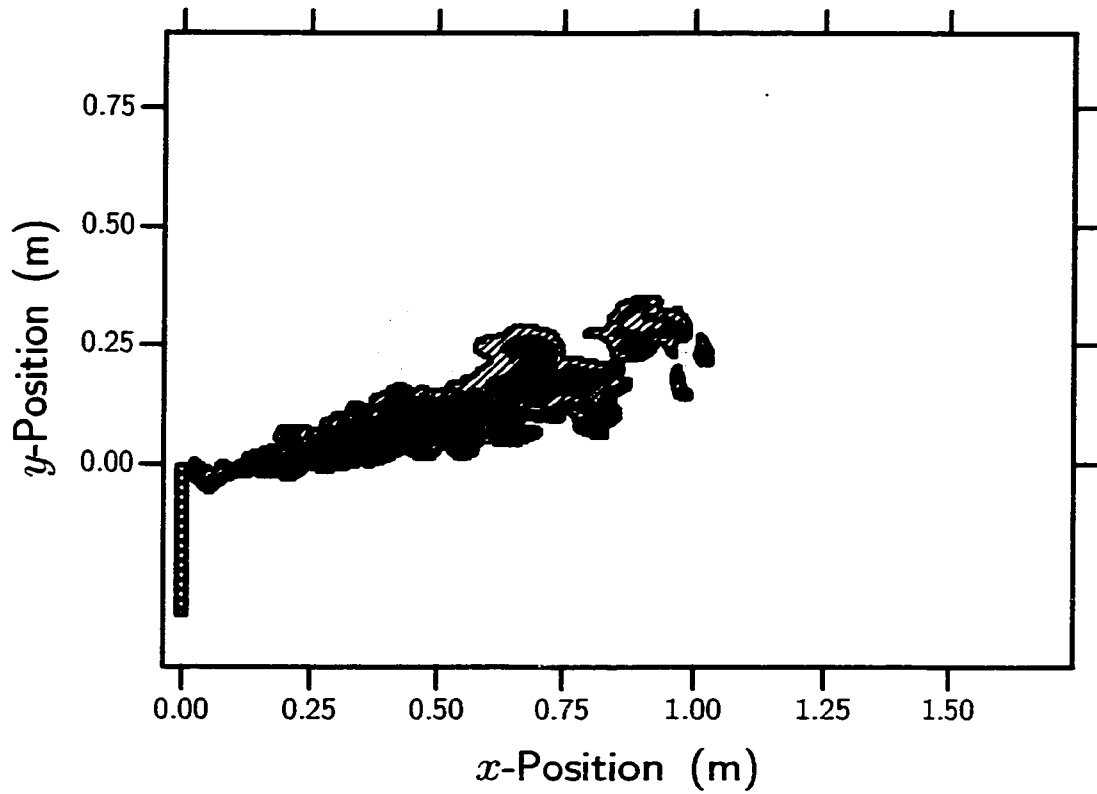
Figure 2.10: Thresholded binary version of Figure 2.6 (a) in outline, overlaying the greyscale image. This binary version was produced by applying a threshold of 188 to Figure 2.6 (a), that ranges in intensity from 11 to 1023, and taking all pixels that have an intensity greater than or equal to that threshold to be flame. Some light regions of flame, which may be difficult to differentiate from the background by eye, are included in the binary image.
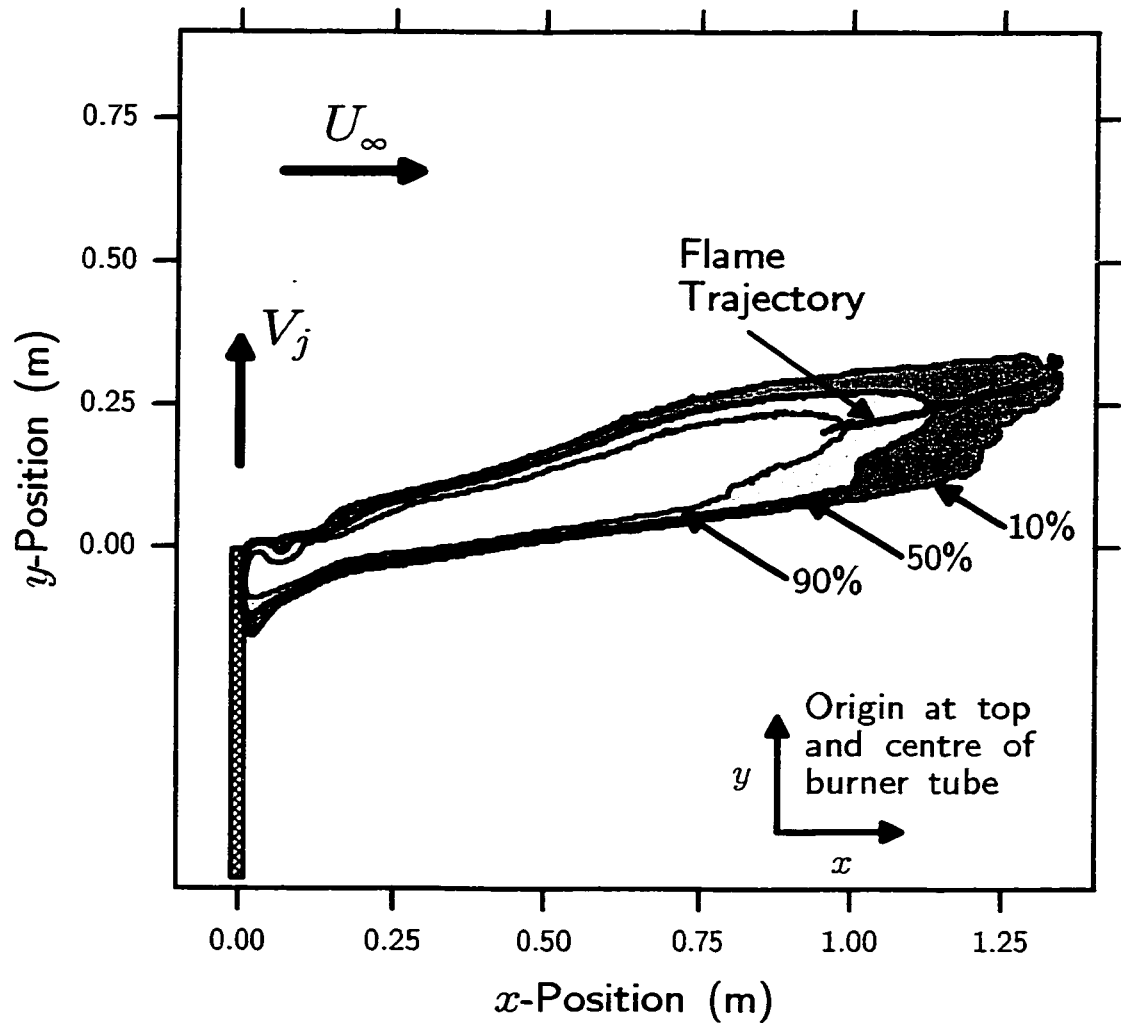
Figure 2.11: Mean flame image of the flame shown in Figure 2.9. It was produced by summing the 200 independent binary images and normalising by the total number of images. The intensity of a pixel in the mean flame image is the probability of flame occurrence at that pixel. Contours are mapped to define the regions of 90 %, 50 %, and 10 % probability of flame occurrence.The trajectory of the mean flame is defined as the curve connecting the peaks (i.e., points of maximum curvature) of the contours of flame occurrence probability.
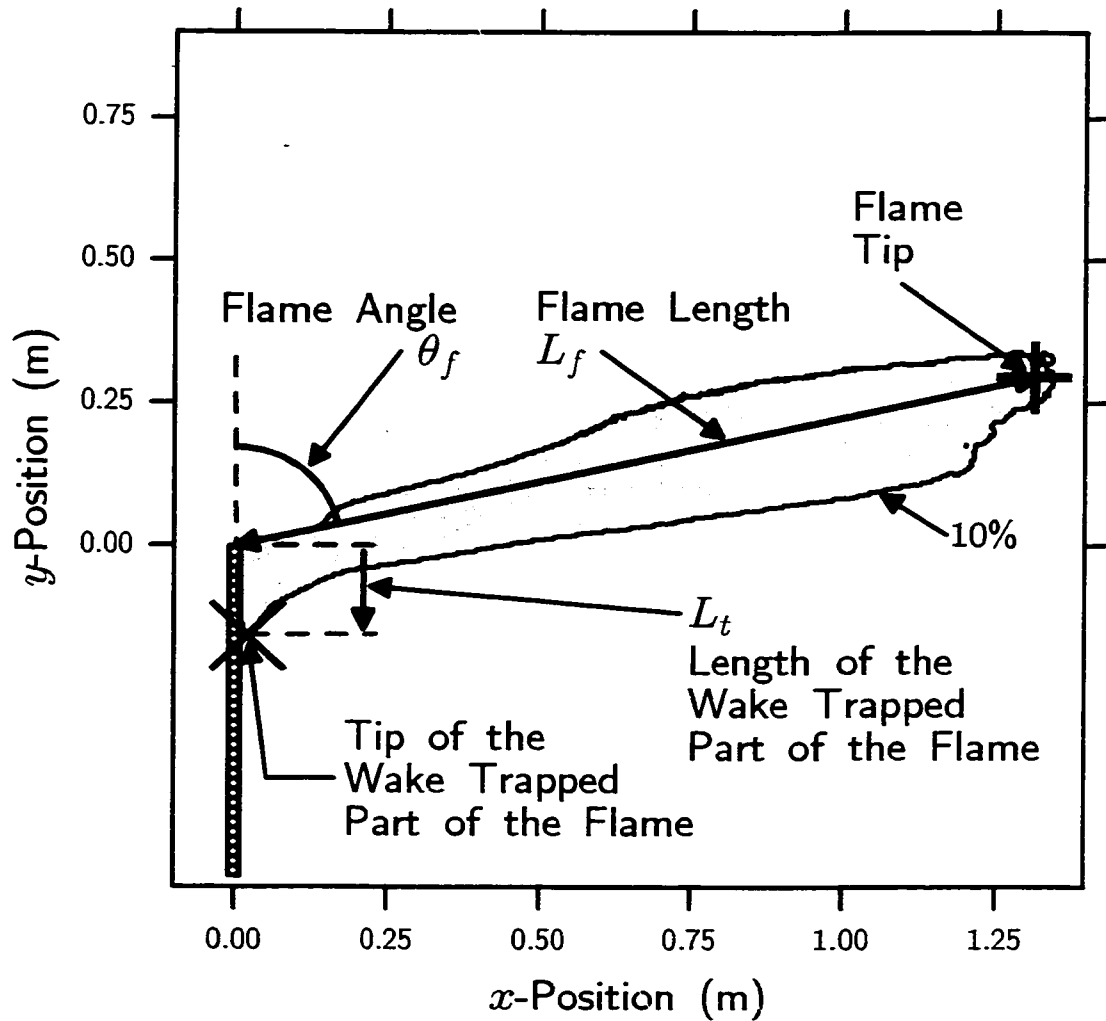
Figure 2.12: The length of the mean flame in Figure 2.11 was defined as the length of the chord connecting the stack exit centreline to the *flame tip*. Flame tip in this figure, and in the results presented is defined at the 10th percentile contour. A small discrepancy in the position of the flame tip is due to the irregular shape of the end of the flame, see Appendix C. The flame angle, $\theta_f$ is the angle that the flame length makes with the vertical. The length of the wake-trapped part of the flame, $L_t$, is the distance from the top of the stack to the lowest point of the flame.
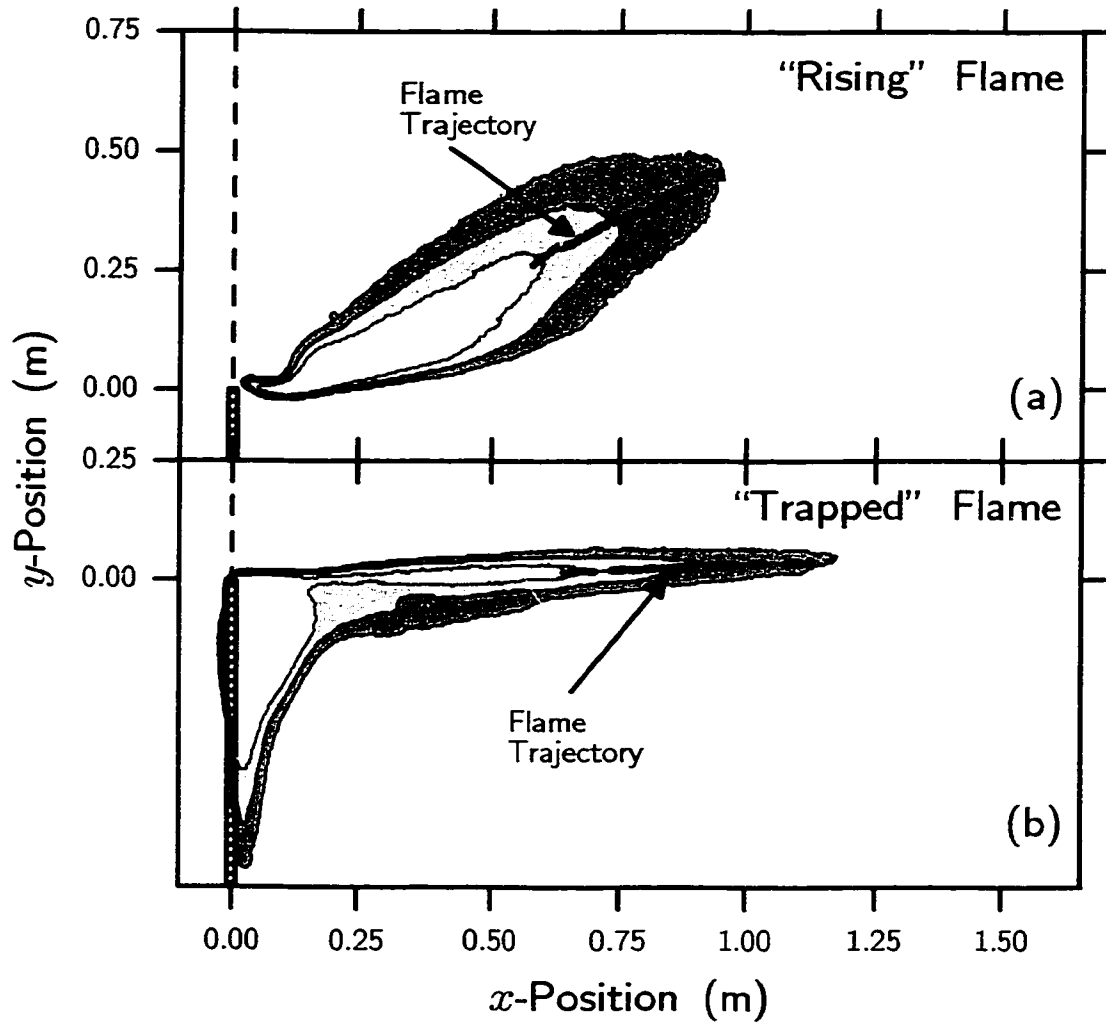
Figure 2.13: These are the calculated flame trajectories for a propane fuelled jet of $V_j = 1\,\mathrm{m/s}$ with: (a) $U_\infty = 1\,\mathrm{m/s}$ ($R = 1.3$); (b) $U_\infty = 8\,\mathrm{m/s}$ ($R = 0.022$). Different regimes in trajectory can be observed in these images. The flame trajectory is, in (a) dominated by buoyancy, "rising"; (b) dominated by cross flow momentum, "trapped".
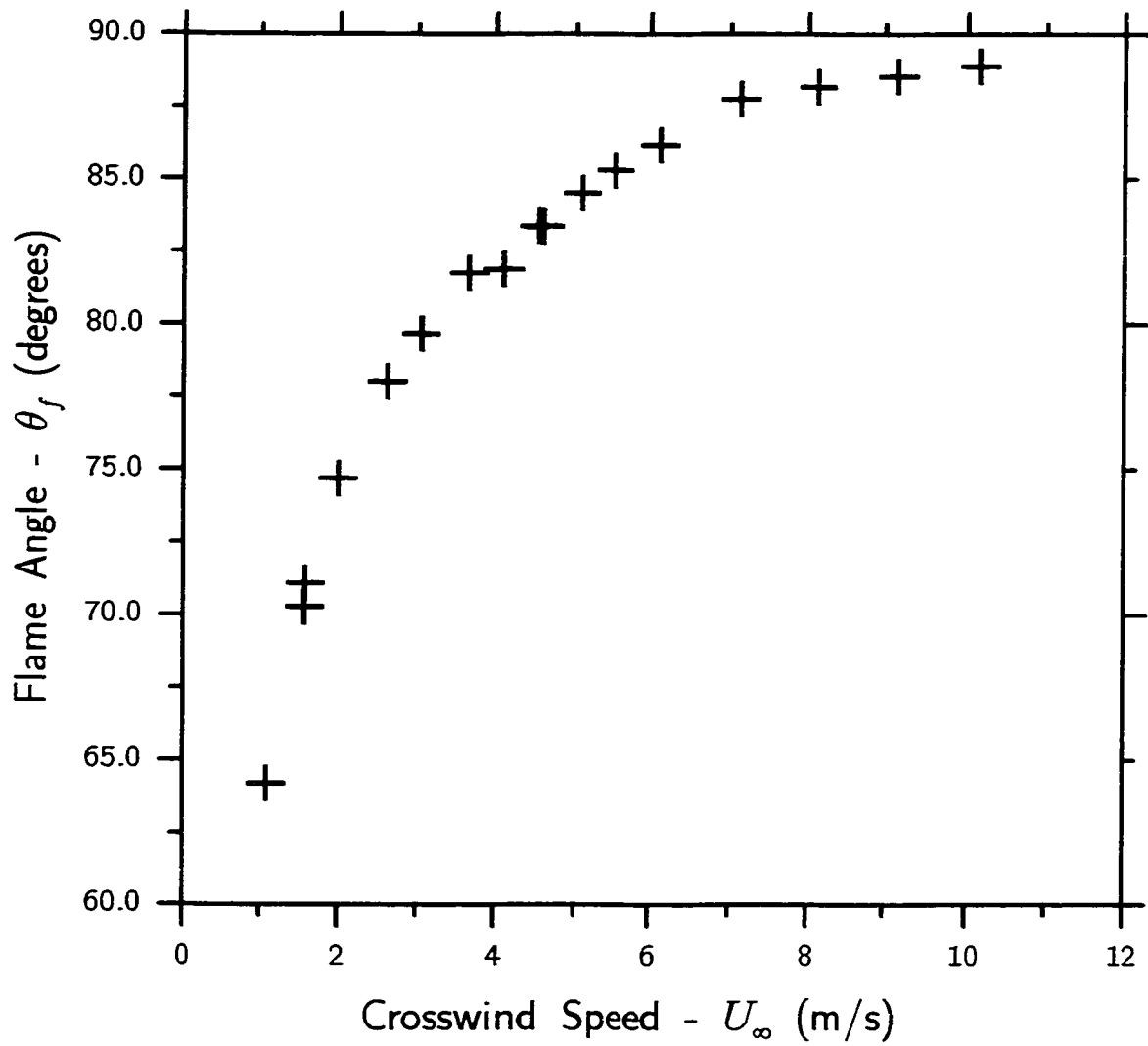
Figure 2.14: Flame angle appears to approach an asymptote at 90° as cross flow velocity increases.
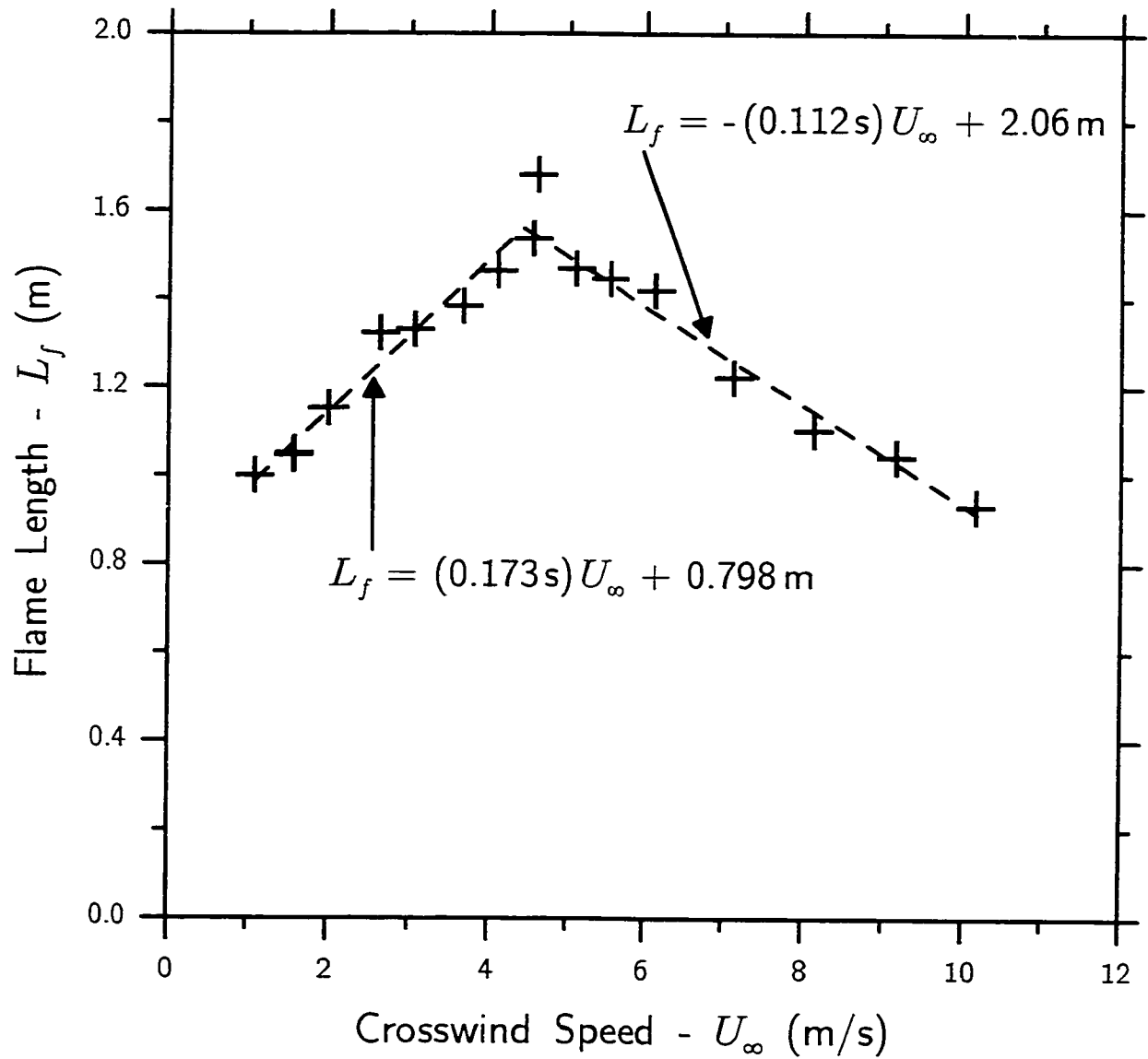
Figure 2.15: Flame length shows a local maximum with cross flow velocity over the range considered. Data reported are for a $V_j = 1$ m/s undiluted propane jet from the $d_s = 22.1$ mm stack.
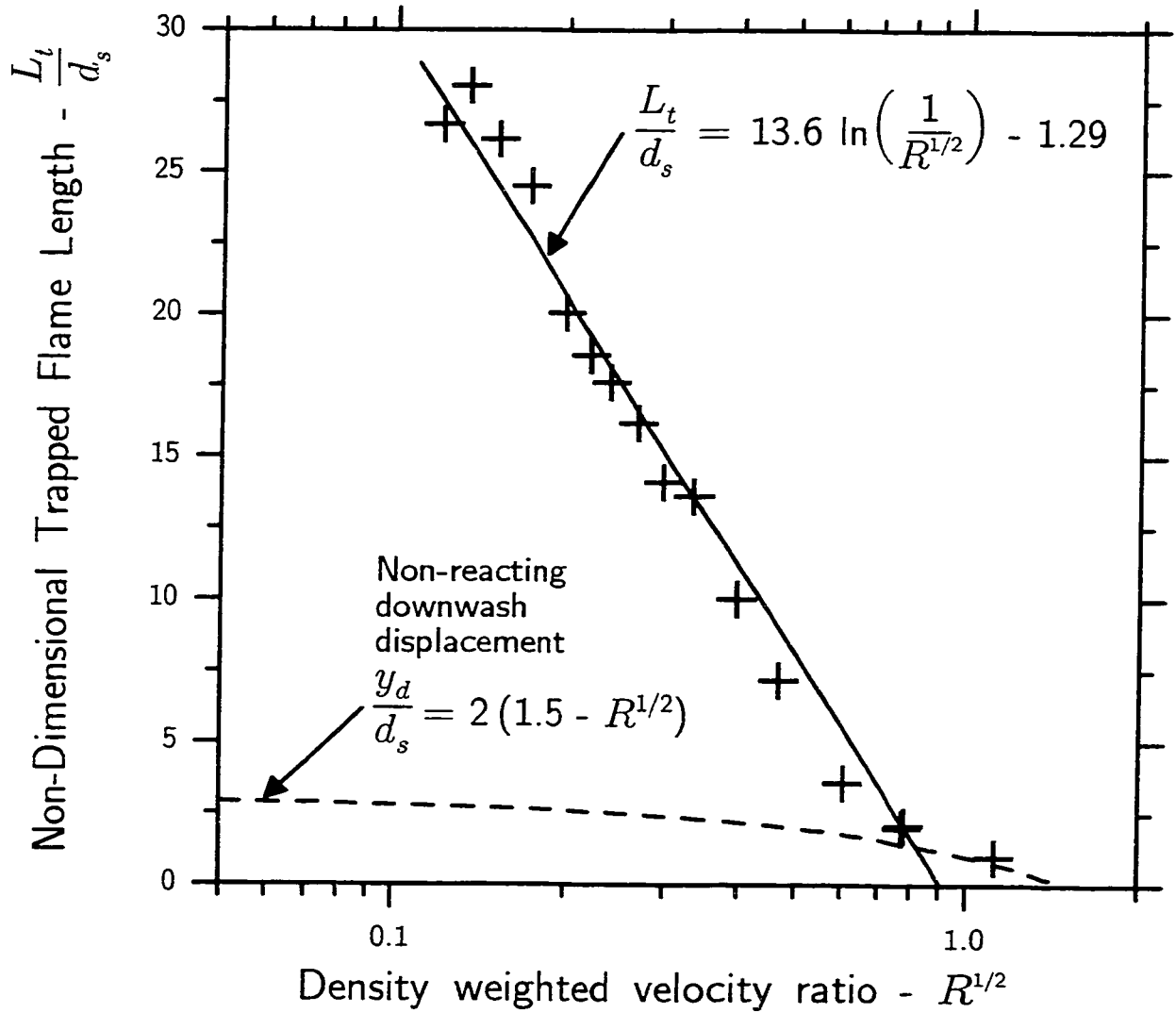
Figure 2.16: The length of the wake trapped part of the flame, $L_t$ is a function of the momentum flux ratio, $R$, which is also the case for the downwash of a non-reacting jet. The downwash displacement for non-reacting momentum jets (Briggs, 1976) shows a linear dependence on $\sqrt{R}$.

# Chapter 3

# Modelling the Length of a Jet Diffusion Flame in Cross Flow

## 3.1 Introduction

Jet diffusion flames were first considered experimentally and modelled by Burke and Schumann (1928). The primary feature of their model for this simplest case of a free laminar flame is that the factor limiting combustion is the diffusion of oxygen into the jet. This idea was extended to turbulent jets by Hawthorne, Weddell and Hottel (1949), and it was supposed that the combustion limiting factor is the entrainment of air by jet turbulence. This has been the basis, for the past 50 years, for the phenomenological modelling of turbulent jet diffusion flames by many investigators, including Hawthorne, Weddell and Hottel (1949); Steward (1970); Becker and Liang (1978); Heskestad (1999). Of particular interest is the observation made by Hawthorne, Weddell and Hottel (1949) and discussed by Becker and Liang (1978) of the effect of jet turbulence on the visible flame. Turbulent fluctuations cause fluctuations in concentration, which in turn cause fluctuations in the shape of the flame. This "smears" the time-averaged tip of the flame, making it difficult to determine

the location of the flame tip. The method for measuring flame length presented in Chapter 2 partially overcomes this difficulty, by defining the length of the flame in terms of its probability of occurrence in ensembles of independent images. It is also important to note the scatter in published data, and the resulting discrepancies between the models of different investigators. Heskestad (1999) presents data from many previous investigations 'collapsed' on a log plot, which exhibits about a 30-50 % scatter in flame length data. Heskestad (1999) also compares the model with existing correlations for flame length in the momentum limit, finding discrepancies of about 50 % for models where flame length is taken to be proportional to the stoichiometric ratio (by mass) of ambient air to fuel, and a factor of 2 for a form which takes flame length to be proportional to (stoichiometric ratio + 1).

A natural extension of these studies is the turbulent diffusion flame in a cross flow. Although not studied as extensively as flames in quiescent environments, the turbulent jet diffusion flame in cross flow has been studied experimentally and modelled by different investigators. The model by Brzustowski (1975) is most widely cited. It was developed by treating the flame as a bent-over round jet with uniform properties and assuming a one-step chemical reaction. It was also suggested that the rate of reaction is proportional to the rate of entrainment, as has been done for jet diffusion flame in quiescent environments. Numerical solution found that flame length was dependent primarily upon the assumed constant of proportionality between the rate of reaction and the rate of entrainment, the entrainment coefficient, and the Froude number, $Fr$. The Froude number is found $Fr = Ri^{-1/2}$, where $Ri$ is the Richardson number, which is the ratio of buoyant to inertial forces acting on a particle. In practice, however, this reaction rate model was found to be accurate only in predicting the near field trajectory of the flame (Brzustowski, Gollahalli and Sullivan, 1975; Gollahalli,

Brzustowski and Sullivan, 1975) because predicted flame lengths were at least an order of magnitude too short (Brzustowski, 1975).

Brzustowski (1976) presented a design oriented method for predicting flame lengths based on cold-flow concentration correlations for hydrocarbon jets. The application of this model is limited to higher jet to cross flow velocity ratios, $V_j/U_\infty > 20$ for propane, $R > 600$, (cf., Gollahalli, Brzustowski and Sullivan (1975)) where jet momentum dominates over buoyancy.

Kalghatgi (1983) adopted a more quantitative approach and collapsed flame lengths by a non-dimensional length scale (flame length divided by the density weighted source diameter) and the inverse of the ratio of jet to cross flow velocities, $(V_j/U_\infty)^{-1}$. The measurements used were conducted for a variety of fuels and stack sizes over the momentum flux ratio range $3 < R < 7 \times 10^3$:

$$R = \frac{\rho_j V_j^2}{\rho_\infty U_\infty^2}$$

(3.1.1)

where $\rho_j$ and $\rho_\infty$ are the densities of the jet and cross flow respectively. Kalghatgi (1983) determined that over this range, flame length is independent of buoyancy forces (i.e., Richardson number independent).

Both the models of Brzustowski (1976) and Kalghatgi (1983) have been shown to have some success in predicting flame length for $R > 1$. There are, however, practical jet diffusion flames that operate outside of this regime. One common example is continuous gas flaring that occurs in the energy and petroleum industries. These flares typically operate in a regime where $R \sim 1$. This is the regime of interest in the present study. Neither the model of Brzustowski (1975) or Kalghatgi (1983) have been successfully applied over the range momentum flux ratios considered here.

More recently, investigators have measured flame lengths in the range of mo-

mentum flux ratios of interest (i.e., $R \leq 1$). Huang and Chang (1994b) observed non-monotonic behaviour in flame length in propane flames around $R \lesssim 1$. Kostiuk et al. (2000) presented flame lengths also for propane over a range of stack sizes within $10 \times 10^{-3} \leq R \leq 1.9$. Kostiuk et al. (2000) also presented a model relating the time scale for a particle of fuel to travel the length of the flame, to the external time scale and collapsed their data over a range of stack diameters ($d_s = 10.8$, $16.7$, $22.1$, and $33.3$ mm).

The present investigation develops a model for jet diffusion flames in cross flow applicable to, but not exclusive to low $R$. The functional form of this model is then compared with new data collected over the range $5.9 \times 10^{-3} \leq R \leq 4.6$. Variables such as cross flow ($U_\infty$) and jet exit ($V_j$) velocities, stack diameter ($d_s$), and dilution of the fuel with an inert compound, were all changed.

## 3.2   A Simple Model for Predicting Flame Length

The model presented here for the important physical processes involved in setting the size of the flame, was deliberately kept simple and consists of only four main concepts. The starting place for the model is an assumed shape for the flame with its size being set by the mass balance of oxygen ($O_2$) required for stoichiometric combustion and the rate this $O_2$ arrives at the flame surface. This base case was then further evolved to include the effects of dilution and cross flow.

### 3.2.1   Flame Geometry

In order to model the jet diffusion flame, it was first necessary to make some assumption about its shape. Kalghatgi (1983) modelled the shape of high velocity ratio,

$V_j/U_\infty > 4$ ($R > 3$), jet diffusion flames as the frustum of a cone (i.e., a cone with the tip removed). The results showed that the cone half angle varied from 5° to 2.8° at the lowest observed velocity ratio. It was also noted that with increasing cross flow velocity relative to the jet velocity, the flame became nearly cylindrical in shape.

In the experiments described in Chapter 2, it was observed that certain mean flame shapes lent themselves to being described as a cylinder (e.g., Figure 2.12). As a first approximation then, the flame is modelled as the surface of a cylinder (with no burning on the circular ends), with mean length $L_f$ and diameter $d_f$, defined in Figure 3.1. This model does not directly consider any fragmentation as seen in some of the instantaneous flame images (Figure 2.7), nor the wake trapped part of the flame that was observed at smaller momentum flux ratios (Figure 2.7). As the mean flame length is the characteristic dimension of interest, these more complicated geometries can be dealt with by letting $d_f$ take some equivalent value such that mean flame length, $L_f$, and mean flame area, $A_f$ reflect actual values.

Because a diffusion flame is being modelled, the surface of the model cylinder is a thin reaction zone, where a stoichiometric mixture exists, with fuel on the inside and oxidant on the outside, as is also shown on Figure 3.1. The surface area of the cylinder,

$$A_f = \pi d_f L_f \qquad\qquad (3.2.1)$$

determines the size of the mean flame.

For scaling purposes, it is assumed that the shape of this cylinder, which will be a function of flow conditions, is geometrically similar. This geometric similarity means that $d_f$ changes in proportion to $L_f$, so that $d_f = K_G L_f$, where $K_G$ is the geometric parameter depending on flow conditions. The area of the flame, $A_f$, can

then be expressed as a function of only its length, $A_f = \pi K_G L_f^2$. This assumption of geometric similarity is tested against experimental data in Section 3.6.

## 3.2.2   Oxygen Mass Balance at the Flame Surface

The size of the mean flame should be related to the amount of fuel provided at the source, because at steady state (i.e., $dL_f/dt = 0$) fuel is being consumed at the flame surface at the same rate that it is being supplied at the source. The modelling of the visible flame can be greatly simplified by considering the analogous cold flow problem. The shape of the flame can be defined as the surface where just enough ambient air has been entrained to create a stoichiometric mixture. Then, assuming that the gradient of fuel concentration is very large at the flame surface, the concentration of fuel is uniform across the fuel stream right up to the flame surface, where it is consumed. With this assumption, the factor limiting combustion (i.e., the consumption of fuel) is the rate at which air arrives at the flame surface, as first suggested by Burke and Schumann (1928), referring to diffusion into free laminar flames. Hawthorne, Weddell and Hottel (1949) extended this idea for turbulent flames by suggesting that the entrainment of air was the limiting factor. This simplifies the analysis because the fuel needs only to be considered in terms of its stoichiometric air requirements, initial conditions $\rho_j$ and $V_j$ at the stack exit and cross flow velocity. For a stable flame then, a parameter ($\dot{m}_{O_2}''$, $kg/m^2s$) is introduced, which represents the mean oxygen mass supply rate per unit area to the mean flame surface. By following the air, rather than the fuel into the flame reaction zone, the difficult task of having to deal with heating (and the associated density changes) experienced by the fuel gas inside the flame cylinder is avoided. Since the required amount of oxygen is directly proportional to the type of fuel and its supply rate, a mass-rate oxygen balance with

the supplied oxygen at the flame surface results in

$$\underbrace{\pi K_G \dot{m}''_{O_2} L_f^2}_{\mathcal{A}} = \underbrace{(\pi/4)\, K_S \rho_j V_j d_s^2}_{\mathcal{B}}$$

(3.2.2)

where term $\mathcal{A}$ is the total rate of $O_2$ consumed over the modelled flame surface area, and term $\mathcal{B}$ is the total rate of $O_2$ required based on fuel supply rate. $K_S$ is the stoichiometric ratio by mass of oxygen to fuel.

$$K_S \equiv \frac{\dot{m}_{O_2}}{\dot{m}_f}$$

(3.2.3)

where $\dot{m}_{O_2}$ is the rate at which $O_2$ arrives at the flame surface (i.e., $\dot{m}_{O_2} = \int_{A_f} \dot{m}''_{O_2} dA$) and $\dot{m}_f$ is the rate of fuel supply at the source.

The treatment of the per unit area rate of arrival of $O_2$ at the mean flame surface, $\dot{m}''_{O_2}$, marks the difference between the present model and some of the more recent ones. It is assumed, like Burke and Schumann (1928), that diffusion is the limiting factor.

A fuel specific flame constant can then be defined as,

$$K_f^2 = \frac{K_S}{4 K_G \dot{m}''_{O_2}} \qquad \left(\frac{\mathrm{m^2 s}}{\mathrm{kg}}\right)$$

(3.2.4)

and flame length, $L_f$, is solved,

$$L_f = K_f \left(\rho_j V_j\right)^{1/2} d_s$$

(3.2.5)

It is also assumed in this mass balance analysis that all of the fuel is consumed by the flame (i.e., combustion efficiency is 100 %). The validity of this assumption is currently under investigation by Bourguignon, Johnson and Kostiuk (1999); Johnson and Kostiuk (2000); Kostiuk et al. (2000).

## 3.2.3 Effect of Fuel Dilution

The extended case of fuel dilution can also be considered in this model. In that case, where part of the fuel is replaced with an inert gas, the cold flow field is defined by the properties of the jet (i.e., $\rho_j$ and $V_j$). For relatively small amounts of dilution then, it is assumed that the diluent does not significantly affect the overall combustion or diffusion processes. By giving emphasis to the diffusion of oxygen from the air side, this dilution case is simplified considerably because it is not necessary to deal with diluted fuels separately. The effect of dilution is to change only the stoichiometric air requirements of the fuel. The stoichiometric constant $K_S$ (Equation 3.2.3) is reconsidered in terms of the fuel concentration in the jet,

$$K_S \equiv \frac{\dot{m}_{O_2}}{C_f \dot{m}_j} \tag{3.2.6}$$

where $C_f$ is the concentration of fuel in the jet

$$C_f = \frac{\rho_f Q_f}{\rho_j Q_j} \tag{3.2.7}$$

and $\dot{m}_j$ is the total mass flow rate of the jet ($\dot{m}_j = \rho_j Q_j$); $\rho_j$ and $Q_j$ are respectively the density and volume flow rate of the jet, and $\rho_f$ and $Q_f$ are those of the fuel component. The effects on flame length can be predicted from the conservation of mass relation developed in Equation 3.2.5, which results in

$$\frac{L_f}{C_f^{1/2}} = K_f \left(\rho_j V_j\right)^{1/2} d_s \tag{3.2.8}$$

It can be seen in Equation 3.2.8 that the predicted effect of dilution is only to scale down the size of the flame while maintaining geometric similarity.

## 3.2.4 Effect of a Cross Flow on Flame Length

The model to this point is not a function of the rate at which the entrained air causes the plume of fuel and combustion products to stretch in the flow direction, thereby affecting the mean flame length, $L_f$. The reason that this stretching occurs is because with balanced fuel supply and consumption rates, discussed in Section 3.2.2, (i.e., $dL_f/dt = 0$), the volume of entrained $O_2$ (and air) must be constant. It was assumed in Section 3.2.2 that the mean mass flux of $O_2$ to the mean flame surface ($\dot{m}''_{O_2}$) was also constant. So for the volume of consumed $O_2$ to remain constant, flame area must also remain constant. From Equation 3.2.1, flame diameter must be inversely proportional to flame length, $d_f \propto L_f^{-1}$ for constant area. Instantaneous images of the flame presented in Figure 2.7 support this.

Having considered the spatial requirements for the appropriate amount of mixing for stoichiometric combustion above, the temporal requisite can now be considered. It has already been established that the surface area of the model flame must be constant for a given fuel supply rate. Once again applying the assumption of the constant flux of oxygen to this surface ($\dot{m}''_{O_2}$), requires that a constant amount of time ($\tau_M$) is required for enough $O_2$ to mix in and react with all of the fuel. By the time the fuel jet has entrained enough air to bend over, which is shortly after it exits the stack, the fuel jet is travelling at the cross flow velocity $U_\infty$. Over the constant mixing time, $\tau_M$, the fuel will advect some distance downstream proportional to $\tau_M U_\infty$. So the shape and diffusion assumptions require that changes in mean flame length, $L_f$, are directly proportional to changes in $U_\infty$. This constant of proportionality, which appears as a time scale, is

$$K_U = \frac{\partial L_f}{\partial U_\infty} \tag{3.2.9}$$

This stretching effect will be added to the quiescent case given in Equation 3.2.8, and the predicted flame length as a function of cross flow velocity is given as

$$\frac{L_f}{C_f^{1/2}} = K_f \left(\rho_j V_j\right)^{1/2} d_s + K_U U_\infty \qquad (3.2.10)$$

Support for the linear increase of flame length with cross flow velocity was observed in Figure 2.15. However, in Figure 2.15 there is also a region where flame length decreases with increasing cross flow velocity. This phenomenon is not predicted by the 'stretching' argument given above. Fortunately, the decrease in $L_f$ with $U_\infty$ also appears to be linear, so the constant $K_U$ should still apply, however with a different value.

## 3.3   Experimental Results

The facility and methodology described in Chapter 2 were used to test this model experimentally.

### 3.3.1   Flame Length Data

Three sets of experiments are presented here to test four of the six different components of the model in Equation 3.2.10: scaling with stack size ($d_s$), jet exit velocity ($V_j$), and dilution of the fuel ($C_f$). Each case was examined over a variety of cross flow velocities ($U_\infty$).

**Scaling with $d_s$**

For the first series, a single jet exit velocity ($V_j = 1$ m/s) of undiluted propane fuel was used for the series of stack diameters: $d_s = 10.8, 16.7, 22.1,$ and $33.3$ mm, described in

68

detail in Chapter 2. Figure 3.2 shows how flame length changes with stack diameter over the range of cross flow velocities, $1 \lesssim U_\infty \leq 13\,\text{m/s}$. The important trend to observe in these data is that a local maximum in flame length occurs at a different cross flow velocity for each $d_s$. This means that normalising flame length by a virtual source diameter (i.e., density weighted), like Kalghatgi (1983) for $3 < R < 7 \times 10^3$, will not collapse the data because the peaks will not align.

## Scaling with $V_j$

Velocity scaling was done with the single $d_s = 22.1\,\text{mm}$ stack and undiluted propane fuel with mean jet exit velocities: $V_j = 0.50$, $0.76$, $0.99$, $1.5$, and $2.0\,\text{m/s}$. Figure 3.3 shows flame length as a function of jet exit speed over the range of cross flow velocities, $1 \leq U_\infty \leq 14\,\text{m/s}$. Similar to different stack sizes, local maxima in flame length occur at different cross flow velocities for varying $V_j$. Huang and Chang (1994b) also observed non-monotonic behaviour in flame length for propane jet diffusion flames in cross flow over the range $R < 5.5$. They found a local minimum in flame length that occurred at higher cross flow velocities as $V_j$ was increased.

## Scaling with $C_f$

The last variable considered was fuel dilution. The jet was introduced to the flow by the 22.1 mm stack, with an exit velocity of 1.0 m/s. Jet composition was set to 0.0 %, 20 %, and 40 % by volume $CO_2$ diluent. Further dilution was impractical because diminished flame luminosity made measurement of flame length problematic. For this special case, the mass and volume fractions are essentially equal, because propane and $CO_2$ have nearly identical molecular weights. For each of these fuel dilutions, data were taken over the range of cross flow velocities $U_\infty = 1\,\text{m/s}$ to

10 m/s. Figure 3.4 shows how diluting the fuel with an inert gas that has the same molecular weight as the fuel affects flame length over the range of cross flow velocities. It is important to note that the variables $\rho_j$ and $\rho_f$ were held constant. These results are particularly important because the behaviour of diluted flames in cross flow has not yet been reported. In Figure 3.4 note that dilution does not appear to affect the cross flow velocity at which the local maximum in flame length occurs, unlike the stack diameter, and jet exit velocity.

## 3.3.2 Comparing Experimental Data with the Model

In order to facilitate plotting, Equation 3.2.10 was rearranged to the form

$$\underbrace{\left(\frac{1}{C_f}\right)^{1/2} \frac{L_f}{U_\infty}}_{\mathcal{Y}} = K_f \underbrace{(\rho_j V_j)^{1/2} \frac{d_s}{U_\infty}}_{\mathcal{X}} + K_U \tag{3.3.1}$$

This suggests a simple linear correlation between the chosen Cartesian variables $\mathcal{X}$ and $\mathcal{Y}$, where $K_f$ is the slope and $K_U$ is the $\mathcal{Y}$-intercept. For simplicity, the ratio of the square-root of the jet flow rate to the cross flow velocity, $(\rho_j V_j)^{1/2} d_s/U_\infty$ will be further addressed in the text as the flame shape parameter $\psi_f$.

Figure 3.5 shows the data plotted with respect to the variables suggested by Equation 3.3.1. Immediately we see that all of the data collapse to a single curve. In order to reflect the actual behaviour of the flame length, this curve was considered as a pair of line segments meeting at a discontinuity that occurs at $\psi_f = 6.74 \times 10^{-3}$ $(\mathrm{kg\,s/m^2})^{1/2}$. The reason that this discontinuity is required is apparent when reconsidering Figures 3.2, 3.3, and 3.4. The discontinuity occurs at the local maximum flame length (i.e., when $L_f$ changes from increasing to decreasing with $U_\infty$). This is reflected in the collapsed data by the change of slope.

70

The best fit lines for both regimes of the data were found by minimising error with respect to flame length, $L_f$, and then choosing the intersection point by minimising the sum of the residuals. Other optimisation methods were also tested. One involved choosing the point of intersection based on maximising the product of the correlation coefficients of the two lines. Another method was to minimise the error in time scale for a fuel particle travelling the length of the flame

$$\tau_{L_f} = \left(\frac{1}{C_f}\right)^{1/2} \frac{L_f}{U_\infty} \tag{3.3.2}$$

(i.e., the $y$-axis in Figure 3.5). Of the methods considered, the chosen one has the largest root mean square error in flame length, but it was felt that it more accurately represented the rates $K_U$ and the conditions for local maximum flame length. The resulting lines are described by

$$\left(\frac{1}{C_f}\right)^{1/2} \frac{L_f}{U_\infty} = 69.6 \; (\text{m}^2\text{s/kg})^{1/2} (\rho_j V_j)^{1/2} \frac{d_s}{U_\infty} - 0.105 \, \text{s} \tag{3.3.3}$$

$$\left(\frac{1}{C_f}\right)^{1/2} \frac{L_f}{U_\infty} = 28.7 \; (\text{m}^2\text{s/kg})^{1/2} (\rho_j V_j)^{1/2} \frac{d_s}{U_\infty} + 0.171 \, \text{s} \tag{3.3.4}$$

and represent flames that shorten and lengthen with increasing $U_\infty$. All terms in Equations 3.3.3 and 3.3.4 are time scales (i.e., have units of seconds), however the incorporation of the unknown $\dot{m}''_{O_2}$ into the flame constant, $K_f$, requires that the slope in Equation 3.3.1 be dimensional.

The lengthening of the flame is caused by the advection of the fuel downstream by the cross flow and is discussed in Section 3.2.4. The shortening of the flame is due to: fuel burned in the recirculating wake of the stack, fragmentation of the flame, and a decrease in combustion efficiency. These mechanisms are discussed in Section 3.5.2. In the collapsed form of the data, Figure 3.5, the intercepts of the lines represent the rate of change of flame length with cross flow velocity, $K_U$, and the slopes are the

71

flame constant, $K_f$. Putting these results into the form of Equation 3.2.10 gives

$$\frac{L_f}{C_f^{1/2}} = 28.7 \; \left(\text{m}^2\text{s/kg}\right)^{1/2} (\rho_j V_j)^{1/2} \, d_s + (0.171 \text{ s}) \, U_\infty \tag{3.3.5}$$

$$\frac{L_f}{C_f^{1/2}} = 69.6 \; \left(\text{m}^2\text{s/kg}\right)^{1/2} (\rho_j V_j)^{1/2} \, d_s - (0.105 \text{ s}) \, U_\infty \tag{3.3.6}$$

where the stoichiometry constant, $K_S$, for propane is 3.65. The rate at which oxygen arrives at the flame surface, $\dot{m}''_{O_2}$ is not known for the present investigation. Each of Equations 3.3.5 and 3.3.6 apply over a subrange of the data collected. Equation 3.3.5 applies while the flame shape parameter, $\psi_f > 6.74 \times 10^{-3}$ $(\text{kg s/m}^2)^{1/2}$ and Equation 3.3.6 while $\psi_f < 6.74 \times 10^{-3}$ $(\text{kg s/m}^2)^{1/2}$. These lines agree with the data within a r.m.s. error of 15 %, which corresponds to a mean error of 8.5 %. At this point, it is important to recall that existing models for flame length without cross flow disagree with each other by up to a factor of 2 (Heskestad, 1999).

**Experimental Uncertainty**

Uncertainties occur because the wind speed in the experimental facility is not perfectly steady. Error is quoted at the 95 % confidence interval (i.e., two standard deviations). In examining the variables in the two axes in Figure 3.5, the common factor is the cross flow velocity, $U_\infty$, which had an r.m.s. uncertainty of 5.7 %. Stack diameter, $d_s$, has negligible uncertainty.

The terms $\rho_f$, $\rho_j$, $Q_f$, $Q_j$, and $V_j$ all have uncertainties, not only because of limitations in the instrumentation and equipment, but also because of the nature of the problem being examined. In Chapter 2, it was shown that over the range of conditions considered the flame was often stabilised directly in the wake of the stack, and combustion occurred directly on the leeward side of the stack. This heated the side of the stack enough that for severely wake-trapped flames, the stack was

72

noticeably bent into the cross flow. This would have the dual effect of preheating the fuel and orienting the jet slightly off perpendicular to the cross flow. It is not a trivial matter to predict the amount of preheating and the conditions of the jet (i.e., $\rho_j$, $V_j$, etc.) at the exit, but if Equation 3.2.10 is reconsidered, we see that the important parameters are in fact the mass flow rates of the fuel component and of the actual jet, which do not change with preheating. The resulting uncertainty in the concentration of fuel in the jet, $C_f$, is less than 1 % for non-unity $C_f$. The uncertainty in the mass flux of the jet, $\rho_j V_j$ is also less than 1 %. It is not expected that the bending of the stack had a significant effect on the actual flame length because the bending itself was small and the mixing processes that control the shape and size of the flame occur over a length scale that is at least an order of magnitude larger than that over which this phenomena will have the most effect (i.e., the diameter of the stack).

Factors contributing to error in the calculated flame length include: resolution of the camera, bending of the stack due to heating by severely wake-trapped flames, and the statistical method of calculating flame length. The resolution is of least concern here, since it is about 100 times less than the length of the flame.

The bending of the stack, is not as insignificant in the calculated flame length. In the most extreme cases, the top of the stack was displaced by no more than one or two stack diameters upstream. Because the stack does not appear in the flame images, and the only images of it are when it is cold, it is not possible to correct the data for this effect. It does not affect the statistics (i.e., the location of the peak of the flame) because of the 2 minute warm up period allowed before any data was taken, but it does affect the calculated length since the actual exit of the stack is further upstream than in the cold case where the stack exit centreline is determined. No corrections were made for the deflection of the stack, but the error caused by stack

bending should be no more that 5 % in its worst case (i.e., a $2d_s$ displacement for the shortest flame).

The statistical method by which the flame length was calculated provides really the only way to put a bound on the expected error in $L_f$. Since the calculated length is based on fitting a line to the relationship between flame length and threshold, the fit statistics were used to define the error in calculated flame length, yielding an r.m.s. value of about 2.5 %. This value was less than the potential error due to stack bending, so a realistic estimate for error in measured flame length is about 2.5 % to 7.5 %.

## 3.4 Model Predictions for Flame Length

Figure 3.5 shows the data and model in collapsed form, however in this form the behaviour of the model relative to the actual data is difficult to follow, so the model has also been plotted with the raw data on Figures 3.2, 3.3, and 3.4. Referring first to the stack diameter scaling series, Figure 3.2 shows that the model accurately predicts the case of $d_s = 22.1$ mm, $V_j = 1$ m/s case, overpredicting by a few percent at larger stack sizes, but underpredicting by about 100 % for the worst case at the smaller stack. The constant line slopes support the model and the cross flow velocity at maximum flame length is predicted within 1 m/s. Comparing these results with those for $V_j$ scaling in Figure 3.3, there is much better agreement at the higher fuel flow rates, and up to 50 % underprediction at the lowest flow rate. Brzustowski (1976) also observed that his model for flame length underpredicted the length of propane flames by up to a factor of 2 for velocity ratios $V_j/U_\infty < 20$. In Figure 3.3, the locations of the peaks are also better predicted, but between the two figures, it is clearly apparent

that the curvature in Figure 3.5 is because the transition that changes the flame from lengthening to shortening with $U_\infty$ is gradual over a small range of $\psi_f$, rather than the abrupt discontinuity predicted by the model. The result is that the conditions at local maximum flame length are not predicted perfectly. The model does, however include a mechanism that accounts for the shifting of the maximum length with $U_\infty$.

Figure 3.4 shows the best agreement between the data and the model. This result is particularly interesting because it supports the supposition that different fuels might be handled simply by modifying the stoichiometry constant, $K_S$, and the rate of oxygen consumption at the flame surface, $\dot{m}''_{O_2}$.

## 3.5 Change in Flame Length with Cross Flow Velocity

Figures 3.2, 3.3, 3.4, and 3.5 all show a discontinuity (within the $U_\infty$ resolution of the data) where flame length goes from increasing with cross flow velocity, to decreasing with cross flow velocity. This does not necessarily contradict the gradual trend seen in Figure 3.5 because other variables ($V_j$ and $d_s$) may be responsible for the 'smear' of the transition region of flame lengthening to shortening in Figure 3.5. Equation 3.3.1 suggests that this change in the behaviour of flame length with cross flow velocity will be reflected in the $\mathcal{Y}$-intercept of Figure 3.5, and it was found that flame length increases with cross flow velocity at a rate of 0.171 s and decreases at a rate of $-0.105$ s. Possible physical mechanisms for the increasing and decreasing $L_f$ phenomena are presented, however no attempt was made to quantify these phenomena in a way that would allow one to predict the rates of flame length increase and decrease with $U_\infty$.

### 3.5.1 Rate of Flame Length Increase with Increasing $U_\infty$

A mechanism for the linear lengthening of the flame with cross flow velocity based on the constant rate of $O_2$ consumption at the mean flame surface was presented in Section 3.2.4. The data support this argument over the range

$\psi_f > 6.74 \times 10^{-3} (\text{kg s/m}^2)^{1/2}$.

The data suggest that the rate of change of flame length with cross flow velocity is the time scale, $K_U = 0.171$ s during the lengthening process, and is valid over all scaling parameters considered. Considering only the lengthening part of the data, the model agrees within an r.m.s. error of 4.1 %.

### 3.5.2 Rate of Flame Length Decrease with Increasing $U_\infty$

After the local maximum in flame length at $\psi_f = 6.74 \times 10^{-3} (\text{kg s/m}^2)^{1/2}$, the length of the flame begins to decrease with cross flow velocity at a rate of 0.105 s as shown on Figures 3.2, 3.3, and 3.4. The model agrees in the flame length shortening regime with an r.m.s. error of 20 %. The present study identifies three phenomena that contribute to this shortening trend, two of which are illustrated in Figure 3.6.

**Flame Pockets and Increase in Surface Area**

The supposition that flame length decrease is due in part to the fragmentation of the flame at higher wind speeds was reported by Kostiuk et al. (2000). The binary instantaneous images in Figure 3.6 (a) show that the flame surface is wrinkled by the vortices formed in the shear layer between the bent over jet and the air stream. As the windspeed $U_\infty$ increases, the vorticity of the $z$-direction (horizontal transverse) vortices in the cross flow $(\partial U/\partial y)$ increases until it overcomes the $x$-direction vortices

in the fuel plume, fragmenting the flame surface. Figures 3.6 (b) and 3.6 (c) show that wake-stabilised flames are stable as a whole flame with $U_\infty$ to the point where the intensity of the stack wake shear layer vortices is sufficient to break off pockets of flame. It was expected, and observed, that the location where the flame starts to fragment moves closer to the stack with further increases in $U_\infty$. The presence of these detached flame pockets clearly alters the geometry of the flame, so that an appropriate model could include flame surface spheres of diameter $d_f$ in addition to the cylindrical flame surface attached to the stack. This combination has more surface area per unit volume than a cylinder alone (i.e., an increased surface area density), so a shorter flame length (length of cylinder plus spheres) is sufficient to consume the same rate of fuel supplied.

In the present study, flame fragmentation was quantified by examining the size distribution of these flame pockets in the individual flame images. Figure 3.7 shows the frequency distribution function of flame pocket size (imaged flame area) for three different cross flows. The most important thing to observe is the high probability of occurrence of large pockets of flame (note the log scale for pocket size). These large areas are the main body of the flame that remains attached to the stack. The second thing of note is the change in trend in the occurrence of the small flame pockets with cross flow velocity. At lower cross flow velocities the tendency is to smaller flame pockets, but as cross flow velocity increases, this tendency shifts towards larger flame pockets as expected.

Referring to Figure 3.6, fragmentation appears to be not only a function of the number of these separated pockets, but also of their size relative to the main flame body. To compare fragmentation at different conditions, flame pocket size was normalised by the size of the main, stack attached body of flame. Figure 3.8 shows the

distribution of the normalised flame pocket sizes, where the change in flame pocket size distribution relative to the essentially *unfragmented* $U_\infty = 1$ m/s case is evident. With increasing cross flow velocity, there are the noticeable trends of the decrease of relatively small flame pockets ($< 1\%$ of main flame body area) by a factor of about 2, and the increase in larger flame pocket size ($> 1\%$ of main flame body area) also by a factor of about 2. Since surface area is proportional to the cross-section area on the video images, it is evident that the small flame pockets do not contribute significantly to the consumption of fuel. The larger pockets will certainly consume a significant amount of the fuel, and thus change the geometry away from the cylindrical flame assumed by the model.

The existence of these detached pockets of flame could affect the calculated flame length, by influencing the mean flame image. Since they are not attached to the stack, the flame pockets will advect downstream at approximately the same speed as the cross flow. This translation will affect the mean flame image (i.e., the size of the regions of flame occurrence probability) because larger pockets will exist longer and travel further than small ones. In order to fully quantify this effect, flame pocket location must be examined as well as size. These spatial effects are not examined here.

Another interesting observation that can be made is that near the local maximum flame length, which is predicted to occur at 4.2 m/s, the occurrence of relatively large flame pockets ($> 10\%$ of the main flame body) drops almost to zero. This suggests that part of the reason the flame is at its longest is that the fuel is being consumed almost entirely by the main, stack attached flame, which is not as spatially efficient as the fragmented flame.

## Trapped Fuel Burned Directly in the Recirculating Wake of the Stack

Figure 3.6 also shows that as $U_\infty$ is increased, more fuel gets trapped and burned directly in the wake of the stack. Figure 3.9 is the mean flame image of a 1 m/s jet of propane from the 22.1 mm stack in an 8 m/s cross flow ($R = 0.022$) and the probability of flame occurrence contours show that this is a regularly occurring phenomenon. As more fuel is consumed in this recirculation region, the axisymmetric tail is required to consume less fuel, and so it becomes shorter. This can be thought of in terms of the cylindrical model, by a larger diameter $d_f$ and shorter length $L_f$. The size of this wake-trapped part of the flame, $L_t$, was discussed in Chapter 2.

## Effect of Combustion Inefficiency on Flame Length

Recent studies by Johnson and Kostiuk (2000); Kostiuk et al. (2000) have shown that the carbon conversion "combustion" efficiency of the flame, $\eta_C$, is strongly dependent on $U_\infty$ within the range considered in the present study. The efficiency has been shown in these references to scale as

$$\eta_C = \eta_C \left[ \frac{U_\infty}{(gV_j d_s)^{1/3}} \right] \tag{3.5.1}$$

The data presented here have a range of values on the right side of Equation 3.5.1 from 1.5 to 19, so based on Figure 8 in Kostiuk et al. (2000), combustion inefficiencies range from 0 to about 3.5 %. Kostiuk et al. (2000) showed by compositional analysis that the unburned hydrocarbons that create the inefficiencies are mostly in the form of unburned fuel, rather than as partially burned hydrocarbon products. This strongly suggests that the $U_\infty$ dependent inefficiency is due to the stripping off and diluting of fuel before it reacts. In the present study it was inferred from this, that the effect of the inefficiency at high cross flow velocities is similar to that of dilution, where the

cold flow field does not change, but there is less fuel supplied for the reaction, and the flame length shortens. Based on these results, it is expected that at the highest value of Equation 3.5.1 in this set of experiments, 96-97 % of the fuel is consumed by the flame. If this is treated as dilution (e.g., 96 % fuel with 4 % non-reacting diluent) only about a 2 % shortening of the flame due to inefficiency is expected.

## 3.6  Geometric Similarity

Figures 3.10, 3.11, and 3.12 test the validity of the geometric similarity assumption discussed in Section 3.2.1 for the range of variables considered. Each shows a series of three different flame shapes, defined by the 10 % probability of flame occurrence, with flames of different size scaled by the flame length. The parameter by which similarly shaped flames are chosen is the flame shape parameter $\psi_f$.

Figure 3.10 shows the scaling of the flame shape with stack diameter, $d_s$ for three different values of the flame shape parameter $\psi_f$ which represent three relatively different flame shapes. Note that flame shapes that end in a vertical line a short distance from the peak are those from flames for which the stack was located upstream (see Figure 2.1) of the camera's field of view because the flame was too large to capture in the field of view, so only the tip was imaged. The flame shape parameter, $\psi_f$ is used here only for scaling the shape of the flame, and makes no assumptions about the trajectory of the flame. In Figure 3.10 (a) the images were taken at different cross flow velocities (i.e., over a range of $1\,\text{m/s} \le U_\infty \le 3\,\text{m/s}$). Despite the variation in flame angle, $\theta_f$, the scaled shapes of the flames are similar. As $\psi_f$ decreases in Figure 3.10 (b) and Figure 3.10 (c) the geometric similarity assumption begins to break down at the smallest stack diameter. In the recirculation zone directly

in the wake of the stack, the flame attached to the $d_s = 10.8\,\text{mm}$ stack does not have the same shape as the others. The transition zone, discussed by Gollahalli and Nanjundappa (1995), has a much lower curvature, and also a shorter downwash length, $L_t$ along the stack, than for the larger $d_s$ flames. The breakdown at the smallest scale has some important implications for previous investigations (e.g., Huang and Chang (1994a,b); Gollahalli and Nanjundappa (1995)) that were done at a smaller scale. The present results suggest that scaling upwards from $d_s = 16.7\,\text{mm}$ is reasonable, however, results from smaller scales may not be applicable to larger stacks.

Jet exit velocity scaling in Figure 3.11 works much better, but again, at the smallest value of $\psi_f$, the wake trapped part of the flame for the lowest $V_j$ is noticeably smaller than the others. With this exception, the flames scale quite well in the near stack region.

Figure 3.12 shows scaling with fuel mixture dilution. This scaling works well despite a 30 % difference in actual flame length. At the smallest value of $\psi_f$, the imaging technique is starting to show its limitations, where in the near stack region the light blue flame does not image as well, as discussed in Chapter 2.

## 3.7   Implications of Constant $K_f$

The flame constant $K_f$ was defined in Equation 3.2.4 as being the square root of the ratio of a stoichiometry constant $(K_S)$ to the product of the geometric constant $(K_G)$ and the rate of oxygen arrival at the flame surface $(\dot{m}''_{O_2})$. Because propane was the only fuel in this investigation, the stoichiometry constant was not varied, so the change in $K_f$ observed in Figure 3.5 is due to a change in the product $K_G\dot{m}''_{O_2}$. In defining the geometry parameter, $K_G$, geometric similarity was used to set the relationship

between flame length, $L_f$, and an equivalent flame diameter, $d_f$, for the cylindrical model. While nearly all of the flame shapes show the assumed geometric similarity property, some of the flame images presented in this study (e.g., Figure 3.10 (c) and Figure 3.11 (c)) do not resemble the cylindrical model. Also not taken into account in the model was the fragmentation of the flame, which changed the geometric relationship between flame length and diameter. Much of the change in $K_f$ can be attributed to change in the geometric constant, which suggests that the assumption that $\dot{m}''_{O_2}$ is set by diffusion and is constant, is valid in the present investigation.

## 3.8 Summary and Conclusions

A simple model is developed that predicts the length of bent-over propane jet diffusion flames in cross flow over the range of momentum flux ratios $5.9 \times 10^{-3} \leq R \leq 4.6$. The flame length model has the form

$$\frac{L_f}{C_f^{1/2}} = K_f \left(\rho_j V_j\right)^{1/2} d_s + K_U U_\infty \tag{3.8.1}$$

where $K_f$ and $K_U$ were determined experimentally.

It is further shown that the appropriate parameter to represent the shape of the flame over this range of $R$ is

$$\psi_f = \left(\rho_j V_j\right)^{1/2} \frac{d_s}{U_\infty} \tag{3.8.2}$$

rather than the density weighted source diameter and the velocity ratio (Kalghatgi, 1983) or the momentum flux ratio (Brzustowski, 1976). Further, the model and data correlation supports the assumption that the mass flux of oxygen transported to a unit area of the flame surface $(\dot{m}''_{O_2})$ is constant. This constant oxidant flux has important implications for developing models for combustion efficiency.

# References

Becker, H. A. and Liang, D. (1978), Visible Length of Vertical Free Turbulent Diffusion Flames, *Combustion and Flame*, 32:115–137.

Bourguignon, E., Johnson, M. R., and Kostiuk, L. W. (1999), The Use of a Closed-Loop Wind Tunnel for Measuring the Combustion Efficiency of Flames in a Cross Flow, *Combustion and Flame*, 119:319–334.

Brzustowski, T. A. (1975), The Turbulent Diffusion Flame in a Cross-Wind, *Proceedings of the Fifth Canadian Congress of Applied Mechanics*, pages 605–606.

Brzustowski, T. A. (1976), Flaring in the Energy Industry, *Progress in Energy and Combustion Science*, 2:129–141.

Brzustowski, T. A., Gollahalli, S. R., and Sullivan, H. F. (1975), The Turbulent Hydrogen Diffusion Flame in a Cross-Wind, *Combustion Science and Technology*, 11:29–33.

Burke, S. P. and Schumann, T. E. W. (1928), Diffusion Flames, *Proceedings of the Combustion Institute*, 1:2–11.

Gollahalli, S. R., Brzustowski, T. A., and Sullivan, H. F. (1975), Characteristics of a Turbulent Propane Diffusion Flame in a Cross-Wind, *Transactions of the CSME*, 3(4):205–214.

Gollahalli, S. R. and Nanjundappa, B. (1995), Burner Wake Stabilized Gas Jet Flames in Cross-Flow, *Combustion Science and Technology*, 109:327–346.

Hawthorne, W. R., Weddell, D. S., and Hottel, H. C. (1949), Mixing and Combustion in Turbulent Gas Jets, *Proceedings of the Combustion Institute*, 3:266–288.

Heskestad, G. (1999), Turbulent Jet Diffusion Flames: Consolidation of Flame Height Data, *Combustion and Flame*, 118:51–60.

Huang, R. F. and Chang, J. M. (1994a), Coherent Structure in a Combusting Jet in Crossflow, *AIAA Journal*, 32(6):1120–1125.

Huang, R. F. and Chang, J. M. (1994b), The Stability and Visualized Flame and Flow Structures of a Combusting Jet in Cross Flow, *Combustion and Flame*, 98(3):267–278.

Johnson, M. R. and Kostiuk, L. W. (2000), Efficiencies of Low Momentum Jet Diffusion Flames in Crosswinds, *Combustion and Flame*, In Press.

Kalghatgi, G. T. (1983), The Visible Shape and Size of a Turbulent Hydrocarbon Jet Diffusion Flame in a Cross-wind, *Combustion and Flame*, 52:91–106.

Kostiuk, L. W., Majeski, A. J., Poudenx, P., Johnson, M. R., and Wilson, D. J. (2000), Scaling of Wake-Stabilized Jet Diffusion Flames in a Tansverse Air Stream, *Proceedings of the Combustion Institute*, 28, In Press.

Steward, F. R. (1970), Prediction of the Height of Turbulent Diffusion Buoyant Flames, *Combustion Science and Technology*, 2:203–212.
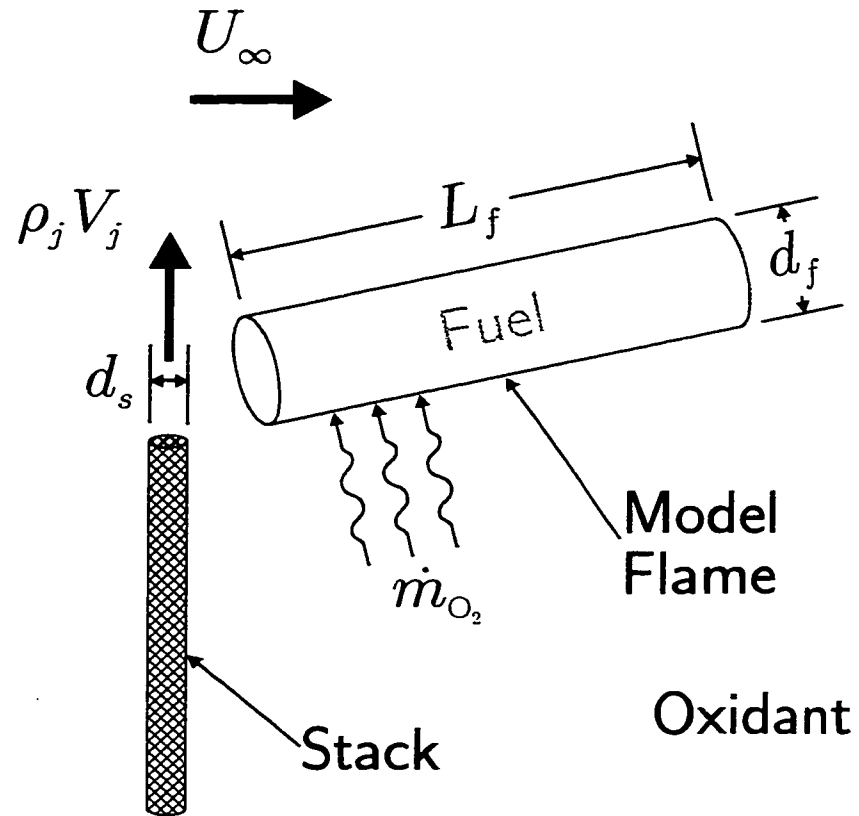
Figure 3.1: The proposed shape for the modelled flame is the surface geometrically similar cylinder, with fuel on the inside and oxidant on the outside.
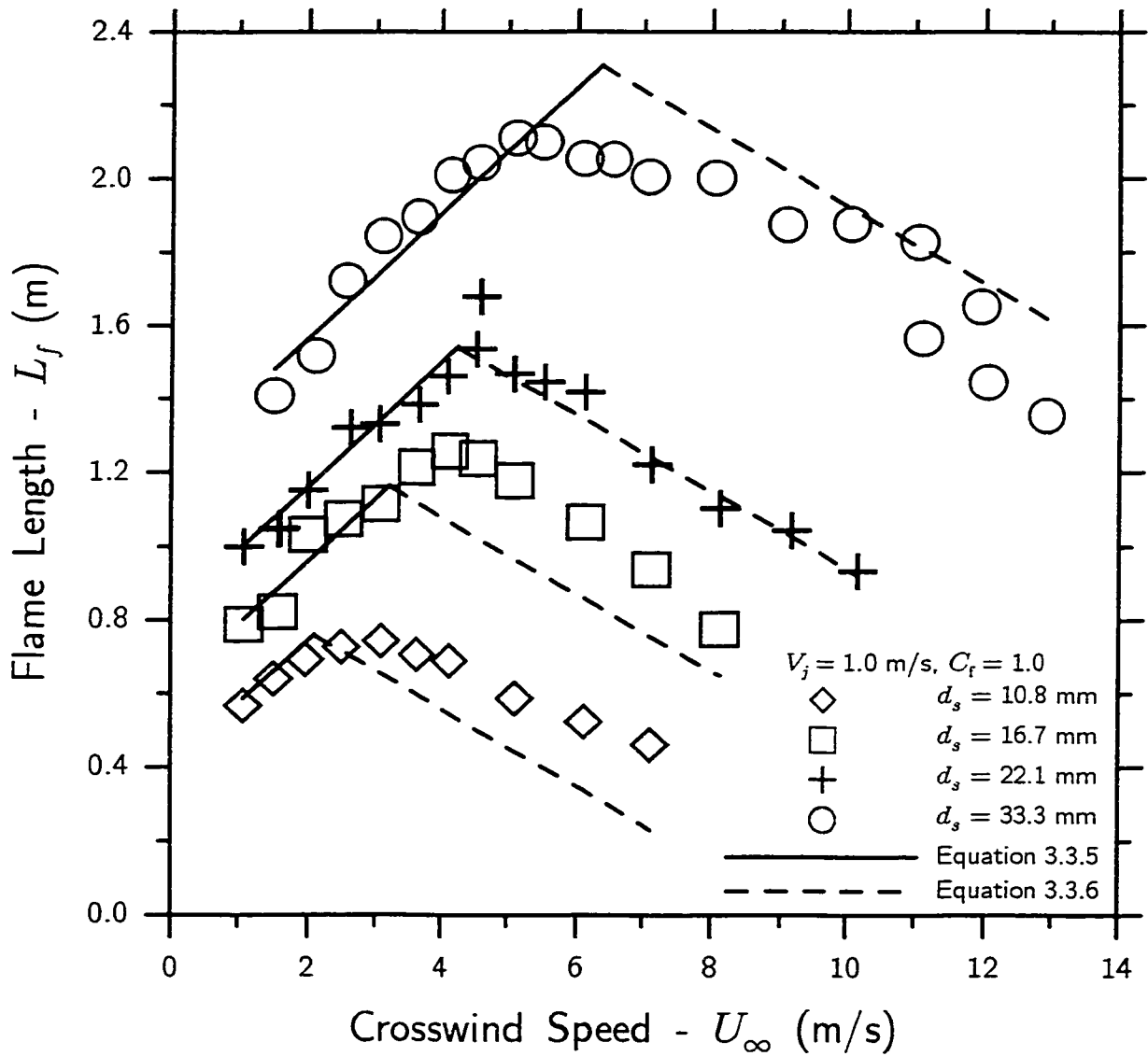
Figure 3.2: Stack diameter scaling data compared with the model for a $V_j = 1.0$ m/s jet of undiluted propane fuel. The model is presented as a pair of lines where Equation 3.3.5 represents the lengthening of the flame, and Equation 3.3.6 models the shortening.
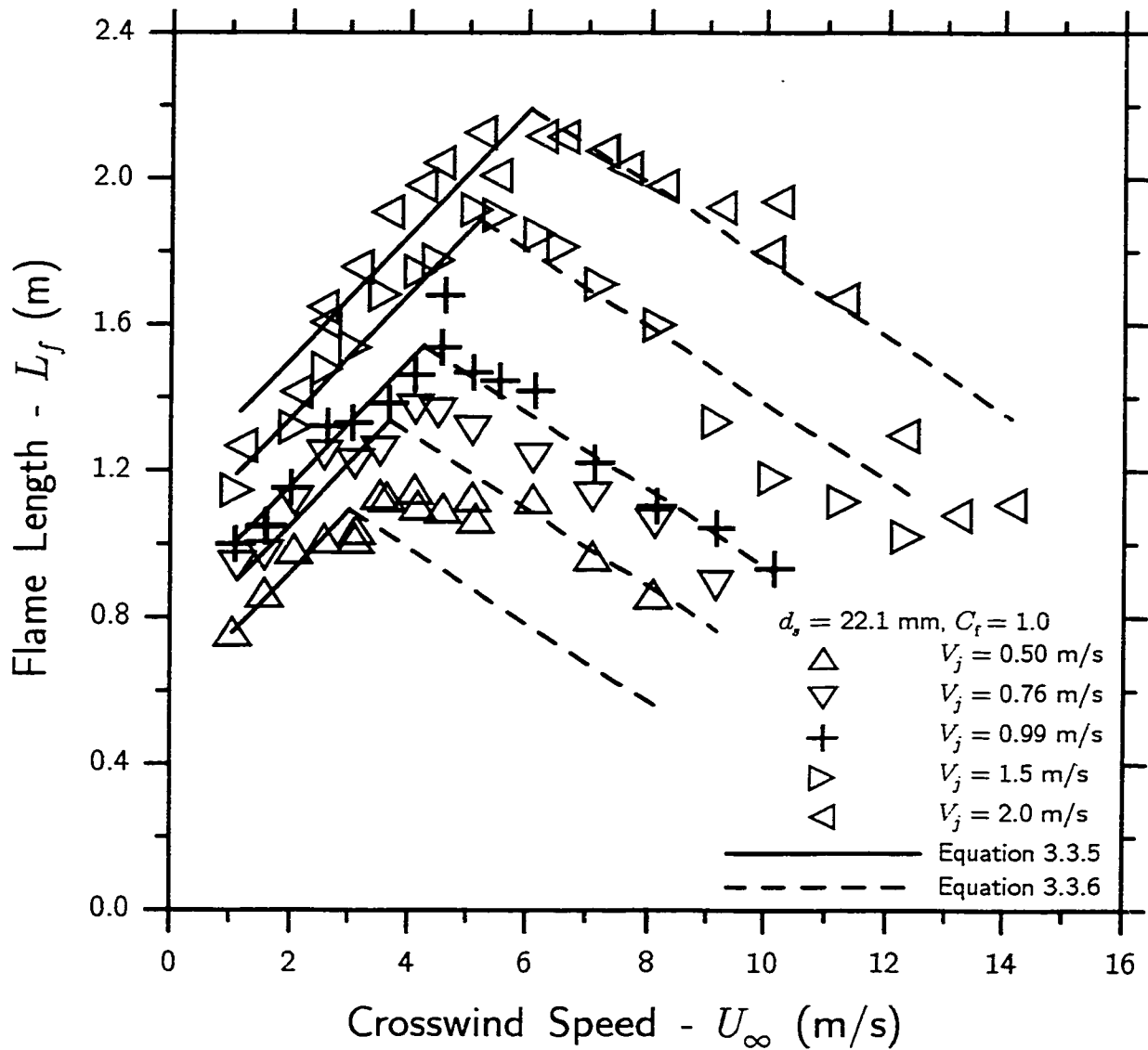
Figure 3.3: The jet exit velocity scaling data for undiluted propane compared with the cylindrical flame model. The model is presented as a pair of lines for the lengthening (Equation 3.3.5) and shortening (Equation 3.3.6) of the flame.
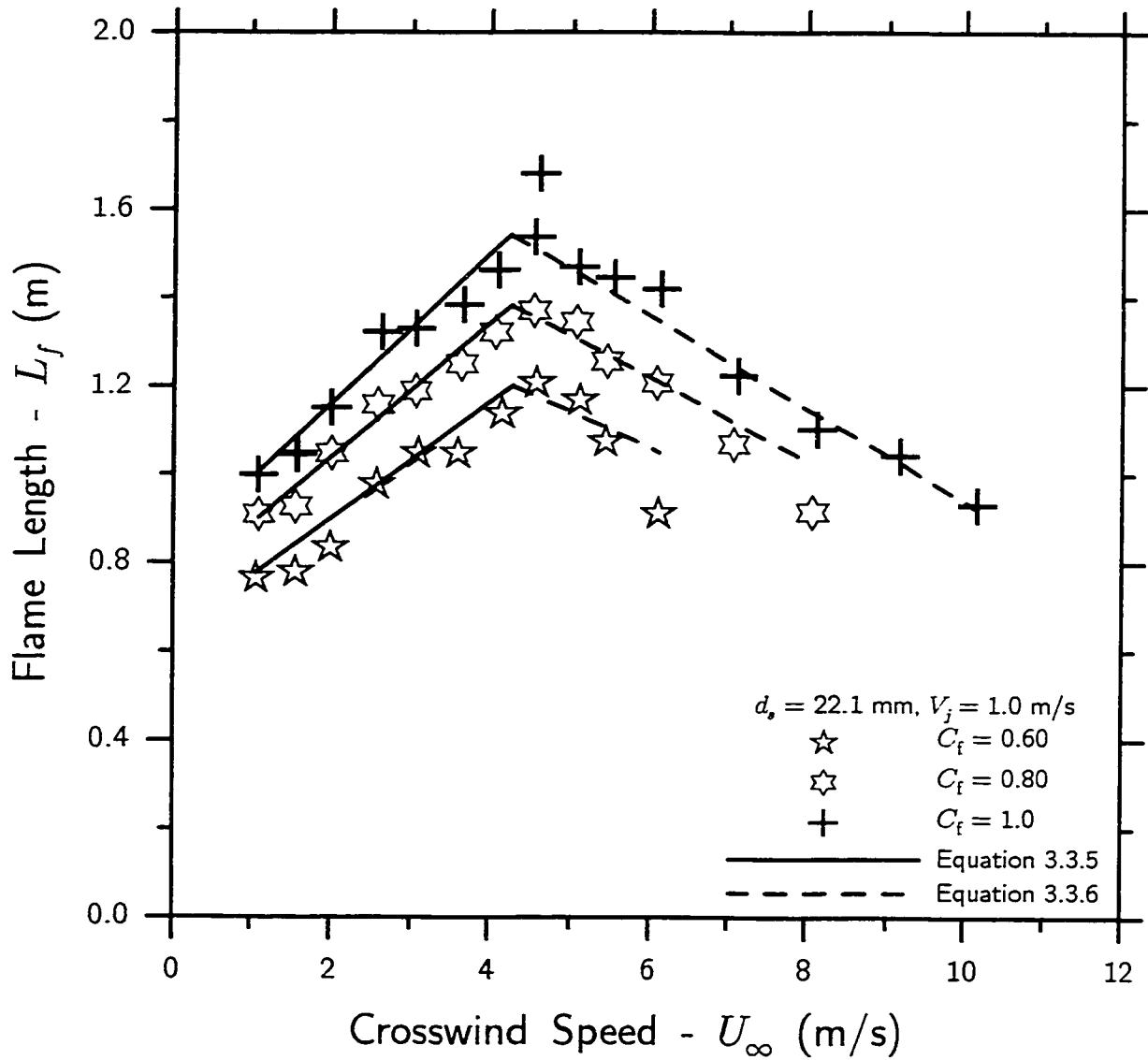
Figure 3.4: Data for a $V_j = 1.0\,\text{m/s}$ jet of diluted propane fuel compared with the model. The model is presented as a pair of solid lines for the lengthening (Equation 3.3.5) and shortening (Equation 3.3.6) of the flame.
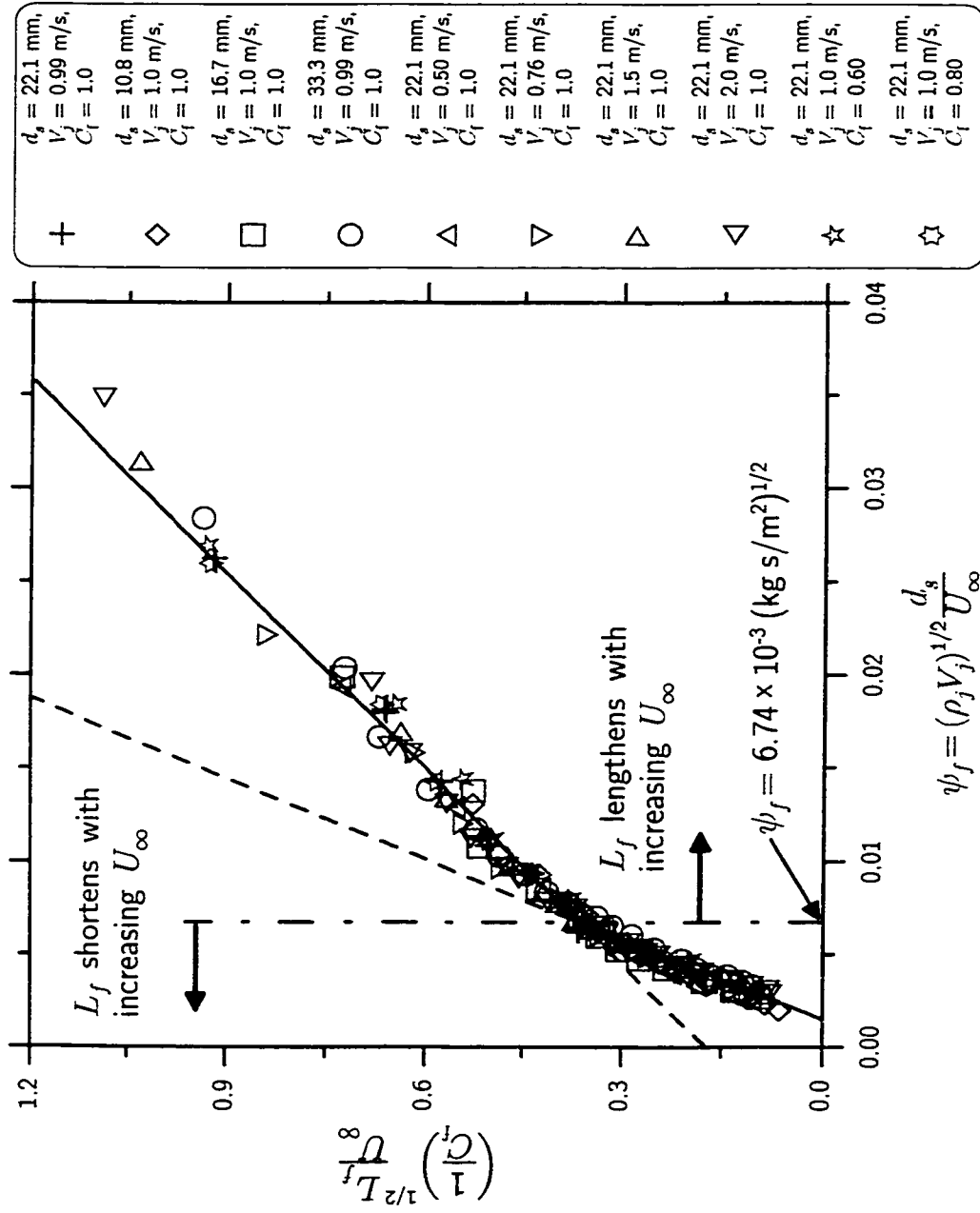
Figure 3.5: Flame length data plotted with respect to the variables suggested by Equation 3.3.1. Two lines are fitted to the collapsed data to reflect the discontinuity observed at the local maximum flame length, which occurs at $\psi_f = 6.74 \times 10^{-3}$ (kg s/m²)$^{1/2}$.
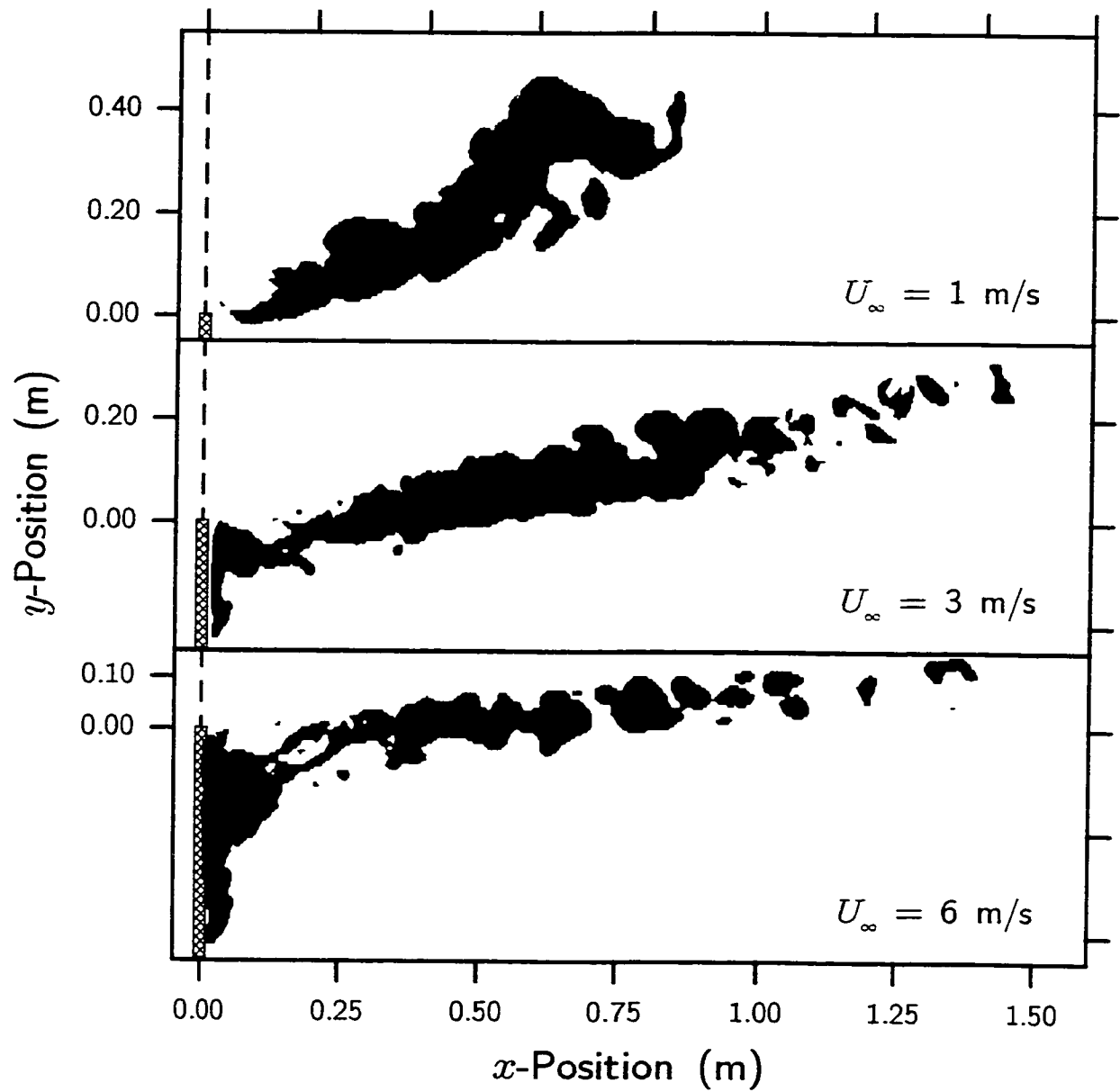
Figure 3.6: Visually observable mechanisms of flame shortening include fragmentation of the flame and fuel being burned directly in the wake of the stack.
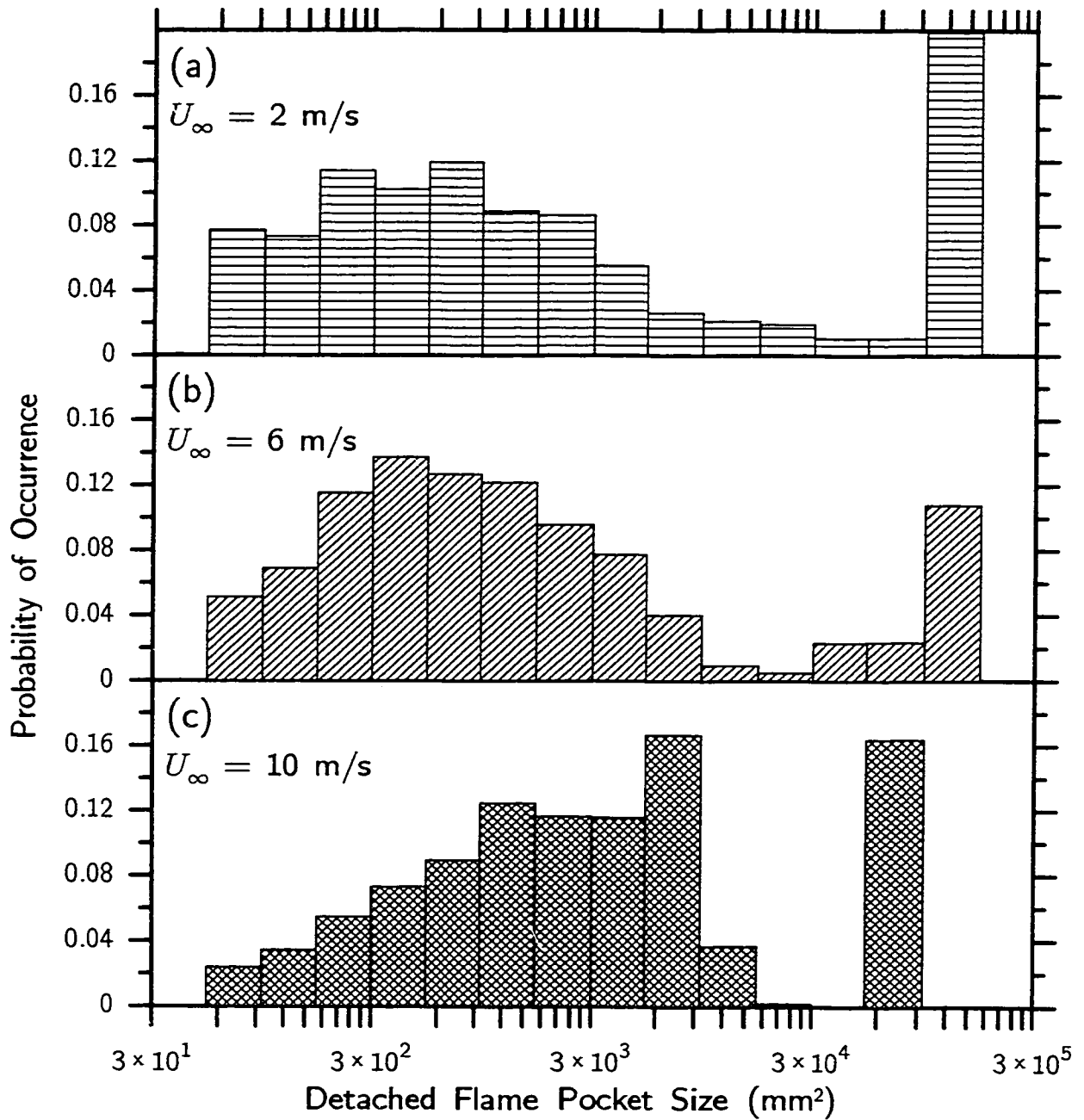
Figure 3.7: The probability distribution of the size of individual flame pockets over a range of cross flow velocities. Frequently occurring large pockets of flame are the main flame bodies that are attached to the stack. Smaller pockets of flame represent fragmentation.
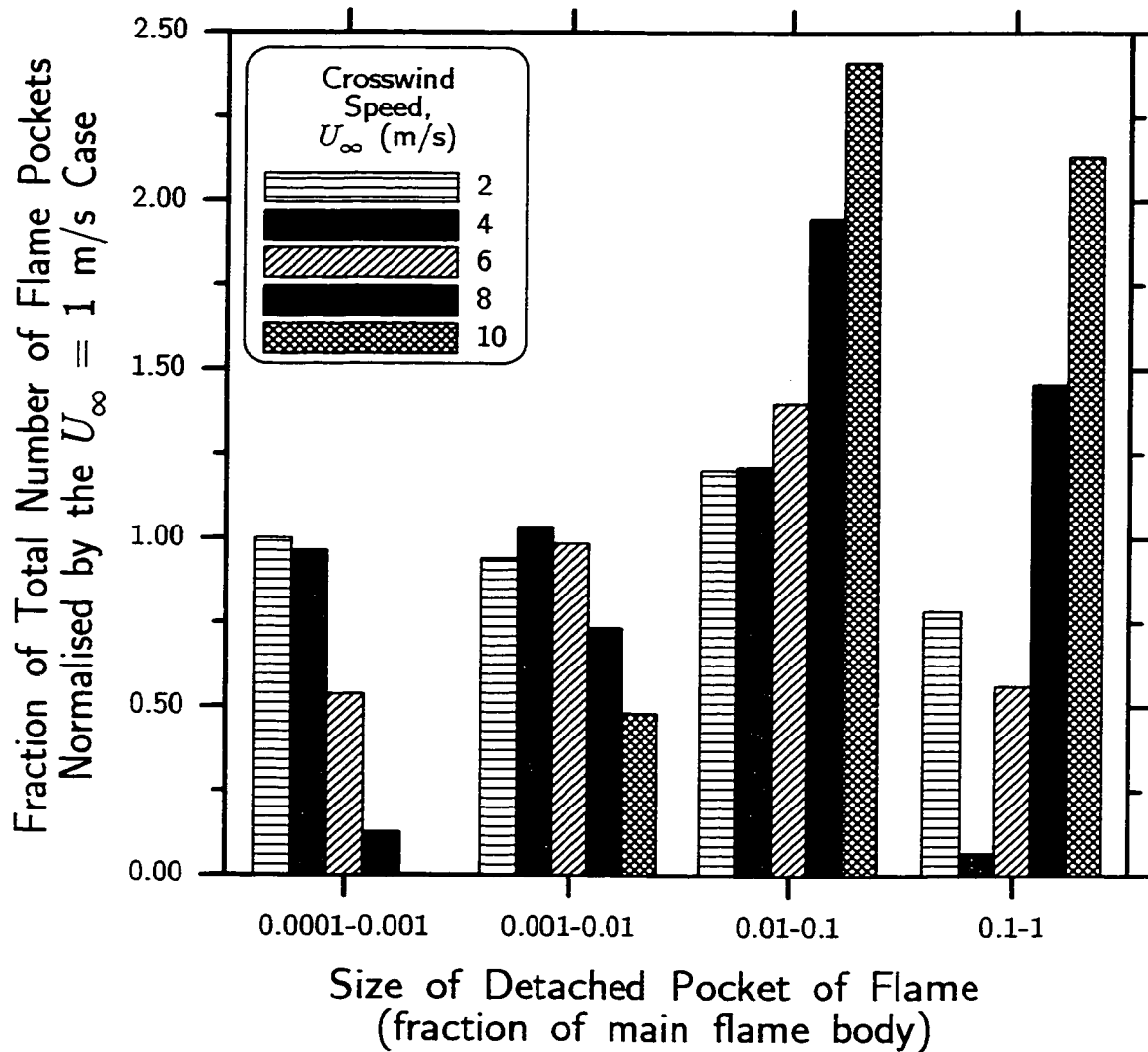
Figure 3.8: The change in the distribution of different flame pocket sizes with cross flow velocity. Flame pocket size is expressed as a fraction of size of the main, stack attached flame (which is not included in the data). Large separated pockets of flame occur more frequently at higher cross flow velocities.
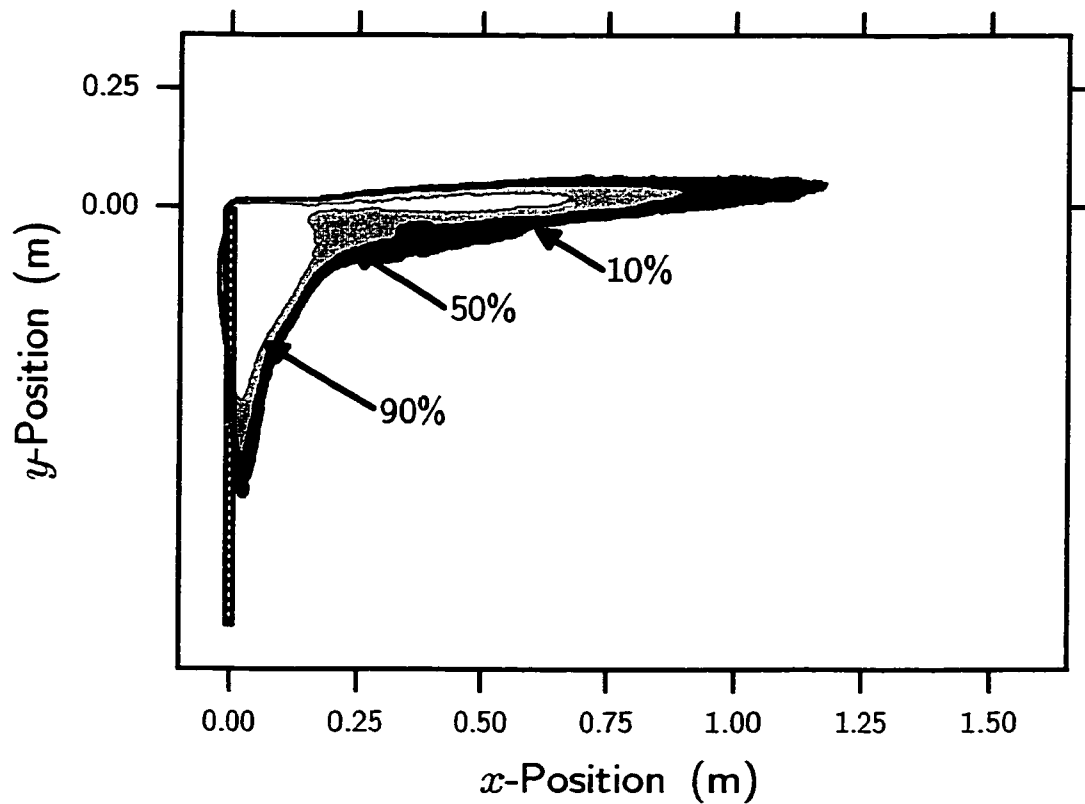
Figure 3.9: The mean flame image of a severely wake trapped flame shows that a significant amount of flame exists regularly directly in the recirculating wake of the stack. The image also gives an indication of the bending of the stack due to heating of the leeward side. The conditions at which this image was taken were: $d_s = 22.1$ mm, $V_j = 1$ m/s, and $U_\infty = 8$ m/s. Contours are mapped to define the regions of 90 %, 50 %, and 10 % probability of flame occurrence.
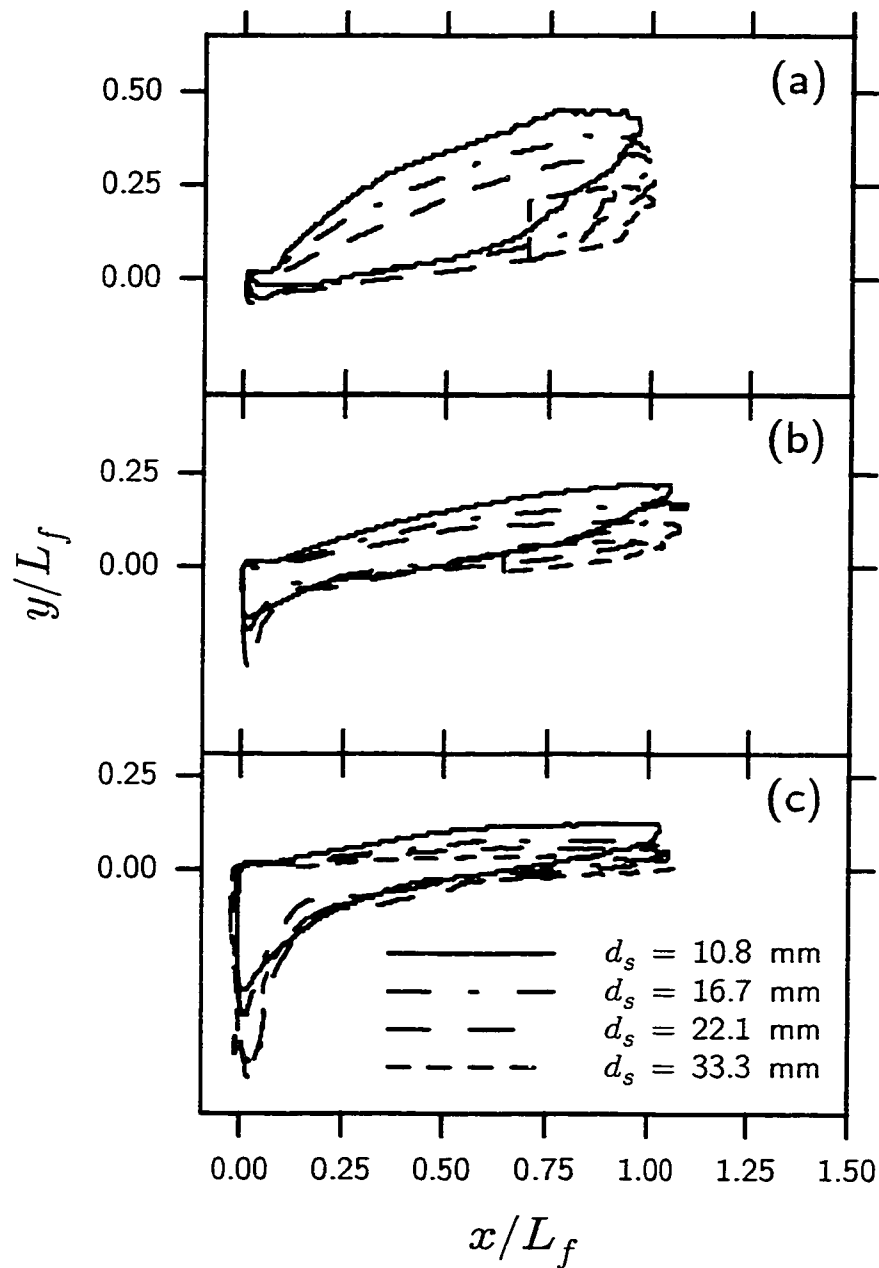
Figure 3.10: Flame shapes collapse reasonably well over a range of stack sizes, with the exception of the smallest stack, which does not follow the same trend at smaller values of the flame shape parameter $\psi_f$. (a) $\psi_f = 0.013$ to $0.014$ $(kg\,s/m^2)^{1/2}$ , (b) $\psi_f = 0.0053$ to $0.0060$ $(kg\,s/m^2)^{1/2}$, (c) $\psi_f = 0.0034$ to $0.0036$ $(kg\,s/m^2)^{1/2}$.
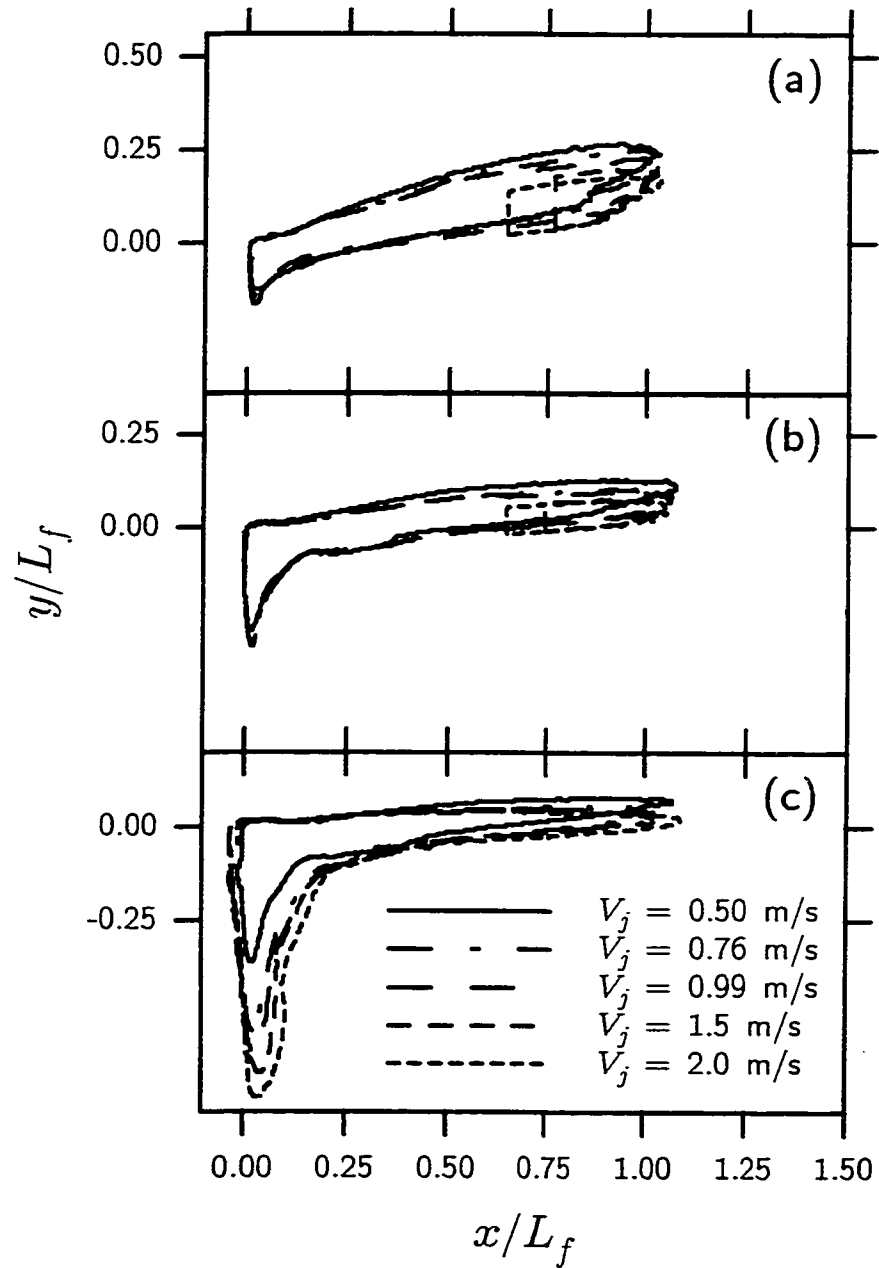
Figure 3.11: Flame shapes scale better with jet exit velocity than with stack size. The different trajectories are still observable at higher values of the flame shape parameter $\psi_f$. (a) $\psi_f = 0.0093$ to $0.0099$ $(\mathrm{kg\,s/m^2})^{1/2}$ , (b) $\psi_f = 0.0047$ to $0.0050$ $(\mathrm{kg\,s/m^2})^{1/2}$, (c) $\psi_f = 0.0031$ to $0.0033$ $(\mathrm{kg\,s/m^2})^{1/2}$.

Figure 3.12: Flame shapes scale best with dilution. All flame also appear to have the same relative trajectory. (a) $\psi_f = 0.018 \, (\mathrm{kg\,s/m^2})^{1/2}$ , (b) $\psi_f = 0.0069$ to $0.0070 \, (\mathrm{kg\,s/m^2})^{1/2}$, (c) $\psi_f = 0.0047 \, (\mathrm{kg\,s/m^2})^{1/2}$.

# Chapter 4

# Summary and Conclusions

A methodology has been presented which allows the investigator to make an unambiguous measurements of flame trajectory and length. Along with this technique a semi-empirical model has been developed for predicting the length the flame. This model was comp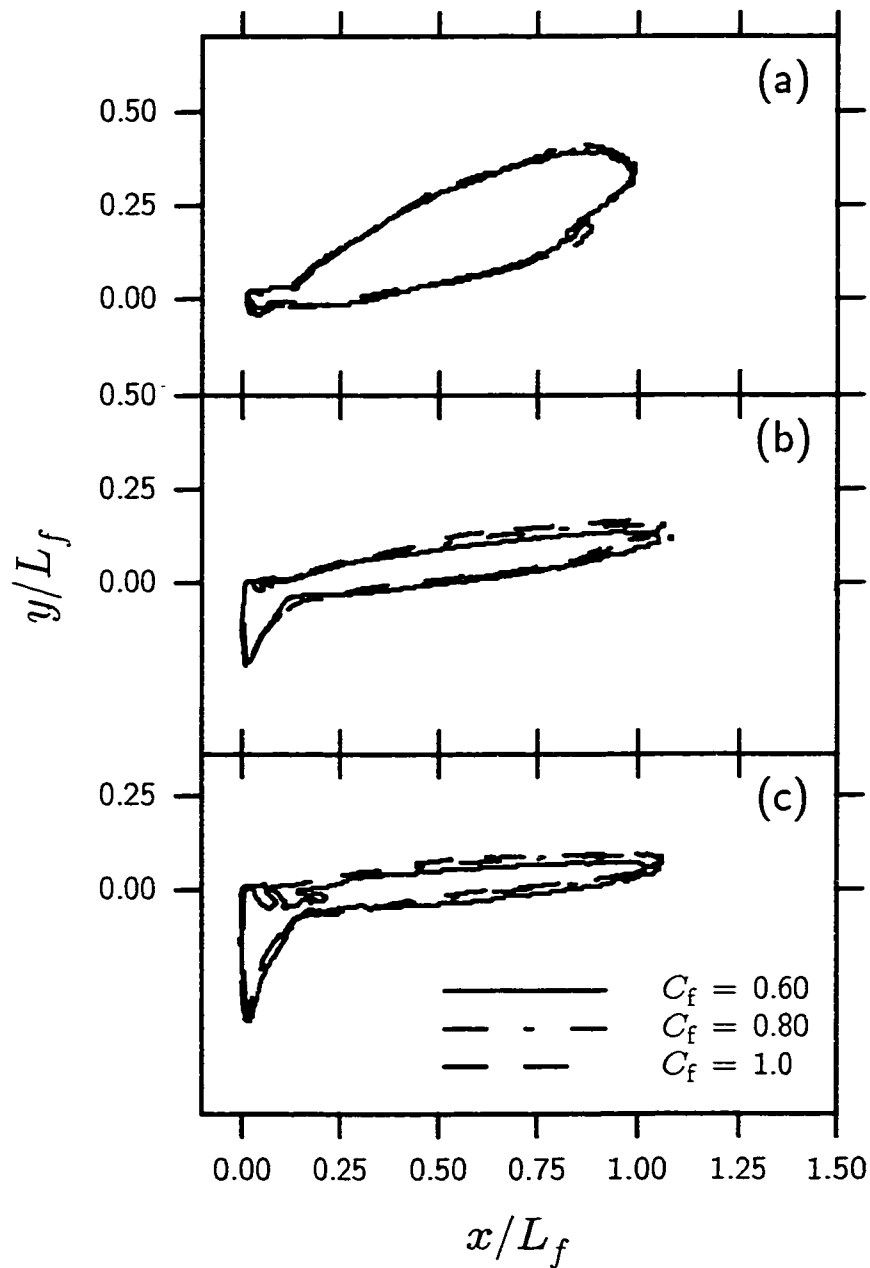ared with data for a propane fuelled flame, changing such variables as cross flow velocity ($U_\infty$), jet exit velocity ($V_j$) and composition ($C_f$), and stack diameter ($d_s$), and it was shown that the model accurately predicted flame length.

## 4.1   Summary of the Measurement Methodology

The first paper (Chapter 2) "Measuring the Trajectory and Length of a Jet Diffusion Flame in Cross Flow" presented a straightforward experimental procedure for measuring both flame trajectory and flame length. These measurements are based on the statistical mean flame. The trajectory follows the path at which the flame is most likely to occur, and the flame length is defined as the chord between the stack exit centreline and the point where flame is expected to occur at least 10 % of the time. Flame length was determined by extrapolating flame lengths determined at several thresholds to a threshold of zero intensity as a way of ensuring consistency and re-

peatability of results. This is in contrast to more traditional measurements of flame trajectory and length, which are typically based on a single long exposure photograph (e.g., Brzustowski, Gollahalli and Sullivan (1975); Huang and Chang (1994b)). The new methodology was used in an initial investigation of the effect of cross flow velocity over a range $1 \leq U_\infty \leq 10$ m/s on flame trajectory and flame length for a propane jet issuing at $V_j = 1$ m/s from a $d_s = 22.1$ mm stack.

## 4.1.1 Conclusions from the Measurement Methodology

For the range of experimental conditions explored in this initial investigation, several phenomena were observed. Two basic flame trajectory shapes were observed that appear to correspond with a buoyancy dominated "rising" plume and a cross flow momentum dominated "trapped" plume. The results for flame length showed a non-monotonic relationship with cross flow velocity, similar to those of Gollahalli, Brzustowski and Sullivan (1975) and Huang and Chang (1994b) but at a much lower momentum flux ratio. A local maximum flame length of about 1.6 m, or about 70 $d_s$ occurred at a wind speed of 4.4 m/s. The rate of flame length increase was about 50 % greater than its rate of decrease with $U_\infty$. The new methodology resulted in consistent and repeatable (within about 5 %) flame length data. Other observations made, include that with increasing $U_\infty$, more fuel gets drawn into and burned in the recirculation region directly in the wake of the stack, and the onset of this wake trapped flame occurs at about $R = 1$.

## 4.2 Summary of the Simple Flame Length Model

The second paper (Chapter 3) "Modelling the Length of a Jet Diffusion Flame in Cross Flow" describes a simple, physically based model for the size of the flame. The model is based on the assumptions that the shape of the flame can be modelled as the surface of a geometrically similar cylinder and that flame length, $L_f$, will change linearly with cross flow velocity by stretching. It was also supposed that the rate of fuel consumption per unit flame surface area is constant and proportional to the rate at which $O_2$ arrives at the flame surface, with the constant of proportionality being fuel specific. The rate at which $O_2$ arrives at the flame surface is set by molecular diffusion and not by flow turbulence. With these simplifications, and doing a mass rate balance on the oxygen required for stoichiometric combustion and the rate at which it arrives at the flame surface yields

$$\frac{L_f}{C_f^{1/2}} = K_f \left(\rho_j V_j\right)^{1/2} d_s + K_U U_\infty \tag{4.2.1}$$

where $K_f$ and $K_U$ were experimentally determined constants. The mechanism for flame length increase with $U_\infty$ was clearly that with higher cross flow velocity, the fuel was advected further downwind before it mixed enough to be completely consumed. The mechanisms of flame length decrease were not so clear because decreasing flame length with $U_\infty$ implies an increase in flame diameter and the 'stretching' assumption does not predict this. Three likely possibilities for the decrease in $L_f$ with increasing $U_\infty$ were considered: fuel consumed in the recirculation zone in the wake of the stack, fragmentation of the flame, and a decrease in conversion efficiency. The flame length model was compared with a range of data, changing stack size ($d_s$), jet exit velocity ($V_j$), fuel composition ($Q_f/Q_j$), and cross flow velocity ($U_\infty$).

## 4.2.1 Conclusions from the Simple Flame Length Model

Over the range of experimental conditions considered $(5.9 \times 10^{-3} \le R \le 4.6)$, the data collapse with respect to the variables suggested by the data to a combination of two lines, each representing the lengthening or the shortening of the flame. Two experimental constants were determined for the lengthening and shortening of the flame, and it was found that a local maximum in flame length occurs when the flame shape parameter, defined by

$$\psi_f = (\rho_j V_j)^{1/2} \frac{d_s}{U_\infty} \tag{4.2.2}$$

is $\psi_f = 6.74 \times 10^{-3}$ $(\text{kg s})^{1/2}/\text{m}$ for propane flames in air. This shape parameter can also be used to pick out similarly shaped flames regardless of their size. The geometric similarity assumption was used to derive $\psi_f$, and it was by this parameter that the geometric similarity assumption was tested and proved to be valid. This result differs from the findings of Kalghatgi (1983) and Brzustowski (1976), who did experiments at higher momentum flux ratios.

A study of the fragmentation of the flame revealed that as cross flow velocity increases, there is a greater occurrence of relatively large (i.e., greater that 10 % of the imaged size of the main flame body) separated flame pockets. The increasing occurrence of these pockets contributes to the shortening of $L_f$ because they increase the surface area density of the flame. The consumption of fuel in the recirculation region in the wake of the stack was also determined to be an important contributor to flame length decrease, but the magnitude of that importance was not quantified. Both fragmentation and trapping of the flame violate the cylindrical geometrically similar assumption, however these effects cause little change in the linear variation of $L_f$ with $U_\infty$. A decrease in the amount of fuel consumed at higher cross flow velocities

(Kostiuk et al., 2000) was determined to have a nominal effect on flame length.

## 4.3 Future Work

The data presented in these papers cover a large range, extending into those expected in application to solution gas flaring. Only two parameters were not realistic: stack size and fuel composition. Built into both models are provisions for scaling the results to full scale application. Four different stack sizes were considered, but were all collapsed on the same model lines, so it is not unreasonable to suggest that these results will apply to the full scale. Ideally, full scale testing should be done to confirm this supposition.

Fuel specific variables were also used in the flame length model and produce a dilution term $(C_f)$, a stoichiometric constant $(K_s)$, and a an oxygen diffusion rate $(\dot{m}''_{O_2})$. It is in this area where future work should be directed. Conditions considered in the present study only had the dilution term appearing as a volume fraction, instead of the mass fraction dependence expected by the model, because the diluent and the fuel had the same density. A diluent with a density different than the fuel gas should be used to determine the validity of the mass fraction assumption in the model. Also, a different fuel should be investigated to see if the stoichiometric and fuel processing constants show the expected behaviour.

As part of the future work, it is hoped that the variables can be considered over a broader range, in an effort to find the physical limitations of the model presented. The extension towards the full scale case is important in determining applicability. During the course of this investigation, and in the study by Johnson and Kostiuk (2000), it was observed that towards the smaller scale $(d_s)$ stacks, the appearance

of the flame began to change. In the present investigation the geometric similarity assumption began to fail for the smallest stack, $d_s = 10.8$ mm, and Johnson and Kostiuk (2000) observed that flames from a $d_s = 5.0$ mm stack had different colour than those from larger stacks. It is important to pursue this direction, not only to place limits on the present results. but to qualify the results of other investigators (e.g., Huang and Chang (1994a,b) and Gollahalli and Nanjundappa (1995)).

An interesting direction that should be pursued is that future experiments could be done at conditions to match the flame shape parameter, $\psi_f$. This would allow the investigator to better quantify the limits of the geometric similarity assumption and also to build a 'catalogue' of flame shapes that could be used for reference in design.

Since the model presented here predicts only the size of the jet diffusion flame, the next logical step beyond modelling size, is to predict the position of the flame. It would be interesting to see how applicable standard, non-reacting plume rise equations would be to the reacting flow case, especially given the present finding that the rate $(\dot{m}''_{O_2})$ at which $O_2$ arrives at the flame surface can be assumed constant, whereas standard non-reacting plume rise models (Briggs, 1975; Weil, 1988) assume that entrainment is proportional to the vertical rise velocity of the plume.

The final place that this research should lead is in determining the size of the wake trapped part of the flame. The location of the flame tip could be found based on the present flame length model, and a yet-to-be-developed trajectory model. The length of the wake trapped flame is the last parameter required for a designer to be able to make a fairly accurate estimate of the size and shape of the flame, allowing for informed decisions when it comes to material and location choices for a flare stack.

# References

Briggs, G. A. (1975), Plume Rise Predictions, In *Lectures on Air Pollution and Environmental Impact Analyses*, chapter 3, pages 59–111. American Meteorological Society.

Brzustowski, T. A. (1976), Flaring in the Energy Industry, *Progress in Energy and Combustion Science*, 2:129–141.

Brzustowski, T. A., Gollahalli, S. R., and Sullivan, H. F. (1975), The Turbulent Hydrogen Diffusion Flame in a Cross-Wind, *Combustion Science and Technology*, 11:29–33.

Gollahalli, S. R., Brzustowski, T. A., and Sullivan, H. F. (1975), Characteristics of a Turbulent Propane Diffusion Flame in a Cross-Wind, *Transactions of the CSME*, 3(4):205–214.

Gollahalli, S. R. and Nanjundappa, B. (1995), Burner Wake Stabilized Gas Jet Flames in Cross-Flow, *Combustion Science and Technology*, 109:327–346.

Huang, R. F. and Chang, J. M. (1994a), Coherent Structure in a Combusting Jet in Crossflow, *AIAA Journal*, 32(6):1120–1125.

Huang, R. F. and Chang, J. M. (1994b), The Stability and Visualized Flame and Flow Structures of a Combusting Jet in Cross Flow, *Combustion and Flame*, 98(3):267–278.

Johnson, M. R. and Kostiuk, L. W. (2000), Efficiencies of Low Momentum Jet Diffusion Flames in Crosswinds, *Combustion and Flame*, In Press.

Kalghatgi, G. T. (1983), The Visible Shape and Size of a Turbulent Hydrocarbon Jet Diffusion Flame in a Cross-wind, *Combustion and Flame*, 52:91–106.

Kostiuk, L. W., Majeski, A. J., Poudenx, P., Johnson, M. R., and Wilson, D. J. (2000), Scaling of Wake-Stabilized Jet Diffusion Flames in a Tansverse Air Stream, *Proceedings of the Combustion Institute*, 28, In Press.

Weil, J. C. (1988), Plume Rise, In Venkatram, A. and Wyngaard, J. C., editors, *Lectures on Air Pollution Modeling*, chapter 3, pages 119–166. American Meteorological Society.

# Appendix A

# Stack Exit Velocity Profiles

As mentioned throughout the text, one possible limitation of the data is that it will not scale to larger full size applications (i.e., solution gas flaring). In order to minimise complications that might arise during the scaling up process, conditions were made as similar to 'real' conditions as possible. Because of the size of the scaled-down model stacks, there arose the concern that the flow coming out of the model stacks would be different than that of full scale stacks.

## A.1   Expected Jet Exit Velocity Profile for Full Size Stacks

A typical flare stack is constructed of a steel pipe that is about 10 m long with an inner diameter of about 10 cm (i.e., $L_s/d_s \approx 100$). For the range of fuel compositions (varying degrees of dilution of propane by $CO_2$) and jet exit velocities ($0.50 \leq V_j \leq 2.0$ m/s) considered here, we can expect values of the jet Reynolds number, defined by

$$Re_j = \frac{V_j d_s}{\nu_j} \tag{A.1.1}$$

104

to be in the range $12 \times 10^3 < Re_j < 46 \times 10^3$. This is well within the range considered to be turbulent flow. For this range of $Re_j$ then, we can expect an entrance length to achieve fully developed turbulent flow of 21 to $26d_s$, even at the extreme case to which we expect to apply the model, $V_j = 6 \, \text{m/s}$, this only increases to $32d_s$, so it is expected the the flow at the exit of the stack will be fully developed turbulent (Munson, Young and Okiishi, 1994). The velocity profile can also then be expected to follow the $\frac{1}{6}$ to $\frac{1}{7}$ power law velocity profile for turbulent flows.

## A.2 Jet Exit Velocity Profile for Scaled-Down Model Stacks

Given the range of stack sizes that could be used for the experiments, it is expected that the range of $Re_j$ considered would be at most 1/3 that expected in the full size case. This places the flows from the model flare stacks squarely in the transition between laminar and turbulent flow, with some cases existing in the turbulent regime ($2500 \lesssim Re_j \lesssim 10 \times 10^3$). To obtain a velocity profile similar to that expected in the full scale, it was necessary to provoke an early onset of turbulence within the model stacks. This was done by adding a plug with an orifice upstream of the stack exit as in Figure 2.4. The sudden expansion of the flow following the orifice causes the flow to decelerate non-uniformly and instabilities result. Some trial and error was required to get the plug into a location where it achieved reasonable results. Figure A.1 shows an example of the resulting velocity profile compared with the ideal $\frac{1}{7}$ power law turbulent profile, and a laminar profile which the flow would have resembled without the plug. Still the profile does not match the $\frac{1}{7}$ power law, but it is more reasonable than the laminar result.

The reason that the model stack velocity profile is 'flatter', resembling a much higher $Re_j$ flow, is because of the level of turbulence still existing at the stack exit. Near the sudden expansion, a particular amount of flow energy is converted to turbulent kinetic energy. This energy is dissipated by viscosity, and eventually the flow would return to a velocity profile very similar to that it had before the orifice plug. The point of the plug, however, was to change the velocity profile in the first place, so it was necessary to locate the plug such that the flow still had a turbulent profile at the stack exit. While the point chosen is clearly not the $\frac{1}{7}$ power law profile desired, it did allow for uniformity amongst the different flow rates, which was also important. Figures A.2 and A.3 show that the velocity profile is relatively independent of $Re_j$ over the range of flow rates and stack sizes considered.

Figures A.4 and A.5 show that turbulence intensity in the flow is similar among the different flow rates and stack sizes considered. This suggests that the turbulence at the exit is at about the same point in decay amongst the different conditions, again reducing the number of variables that could impact the results.

The velocity and turbulence measurements were made with a laser Doppler velocimeter, using natural gas seeded with oil as the working fluid. Natural gas was used because it is safer to use than propane, and the kinematic viscosity ($\nu$) of air is too low to reliably reproduce the required Reynolds numbers. Flow rate was set to result in $Re_j$ similar to those expected of propane at the exit velocities of interest.

# References

Munson, B. R., Young, D. F., and Okiishi, T. H. (1994), *Fundamentals of Fluid Mechanics*, chapter 8, pages 455–534, John Wiley & Sons, Inc., 2nd edition.
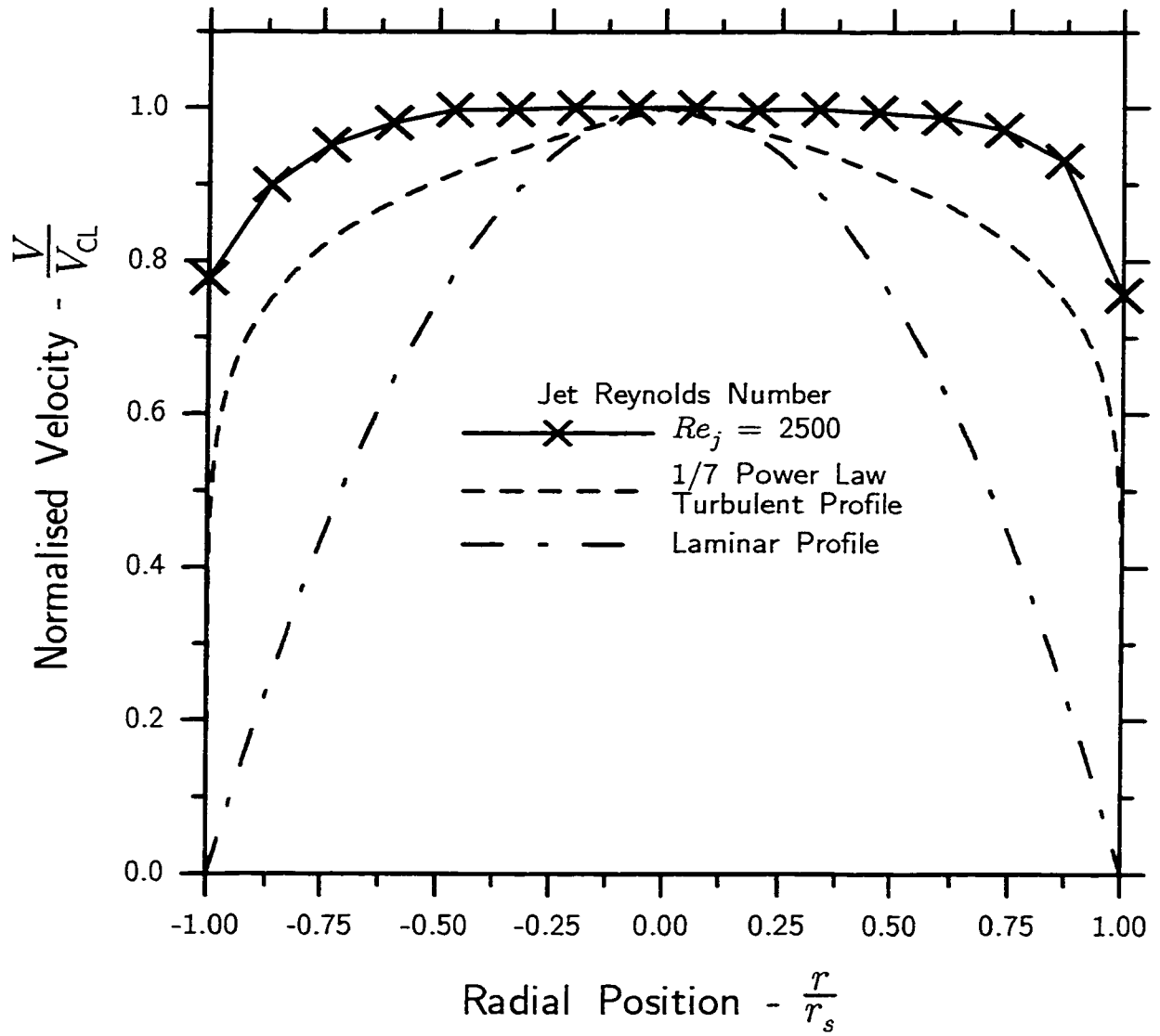
Figure A.1: The presence of the orifice plug results in a turbulent exit velocity profile at the exit of the stack, at a Reynolds number where a laminar profile is expected.
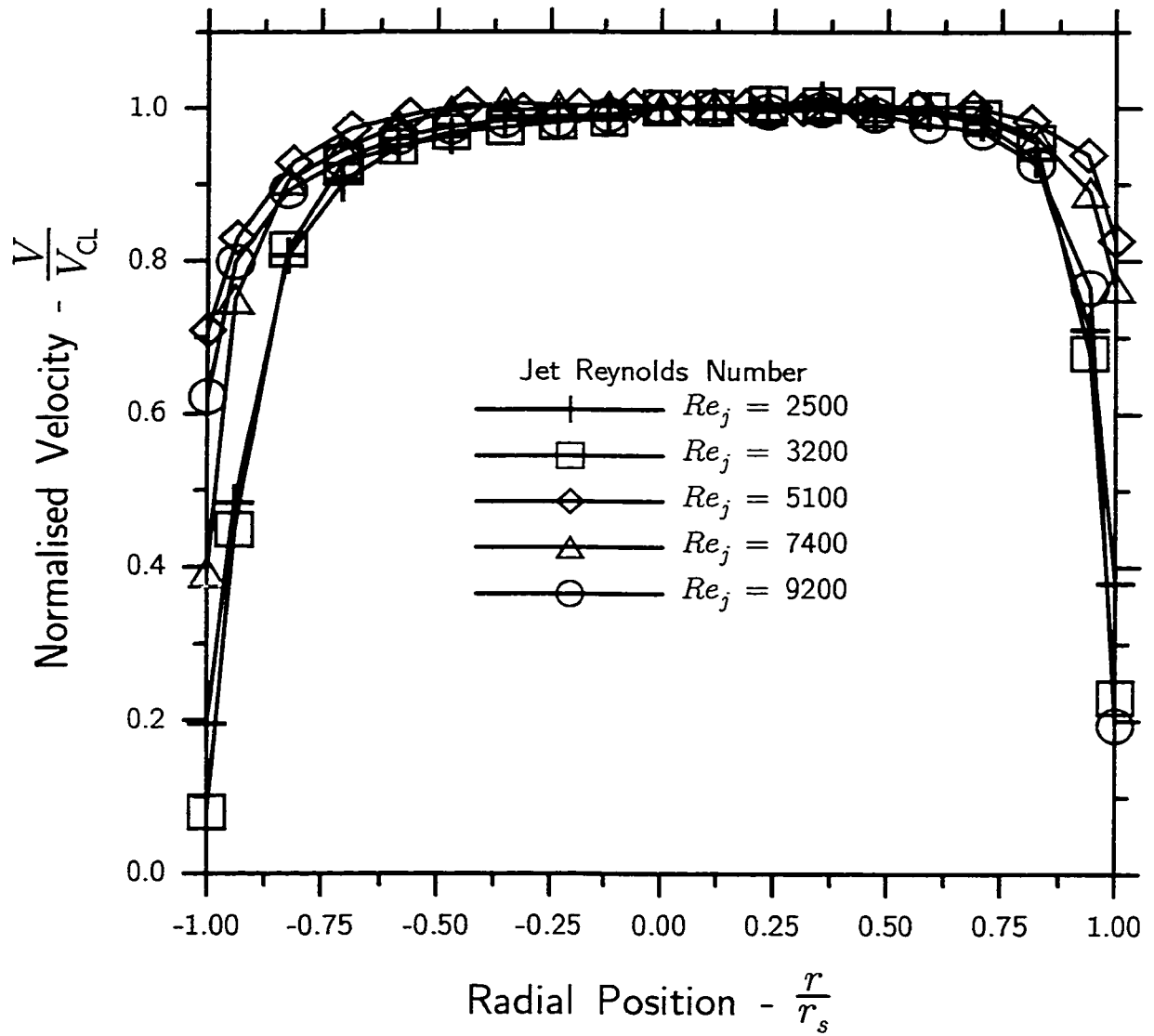
Figure A.2: The jet exit velocity profiles are similar for all exit velocities considered for the $d_s = 22.1$ mm stack.
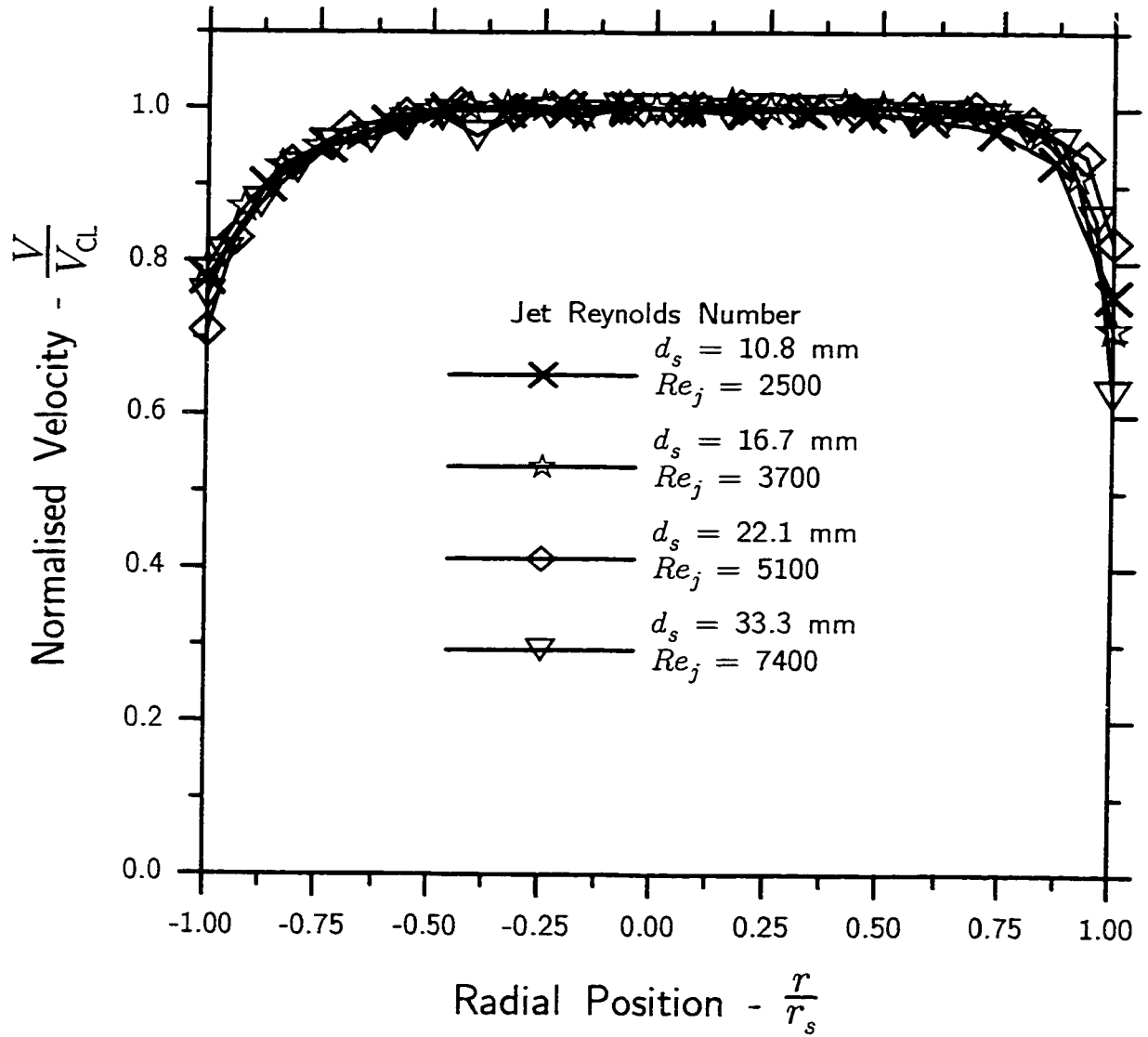
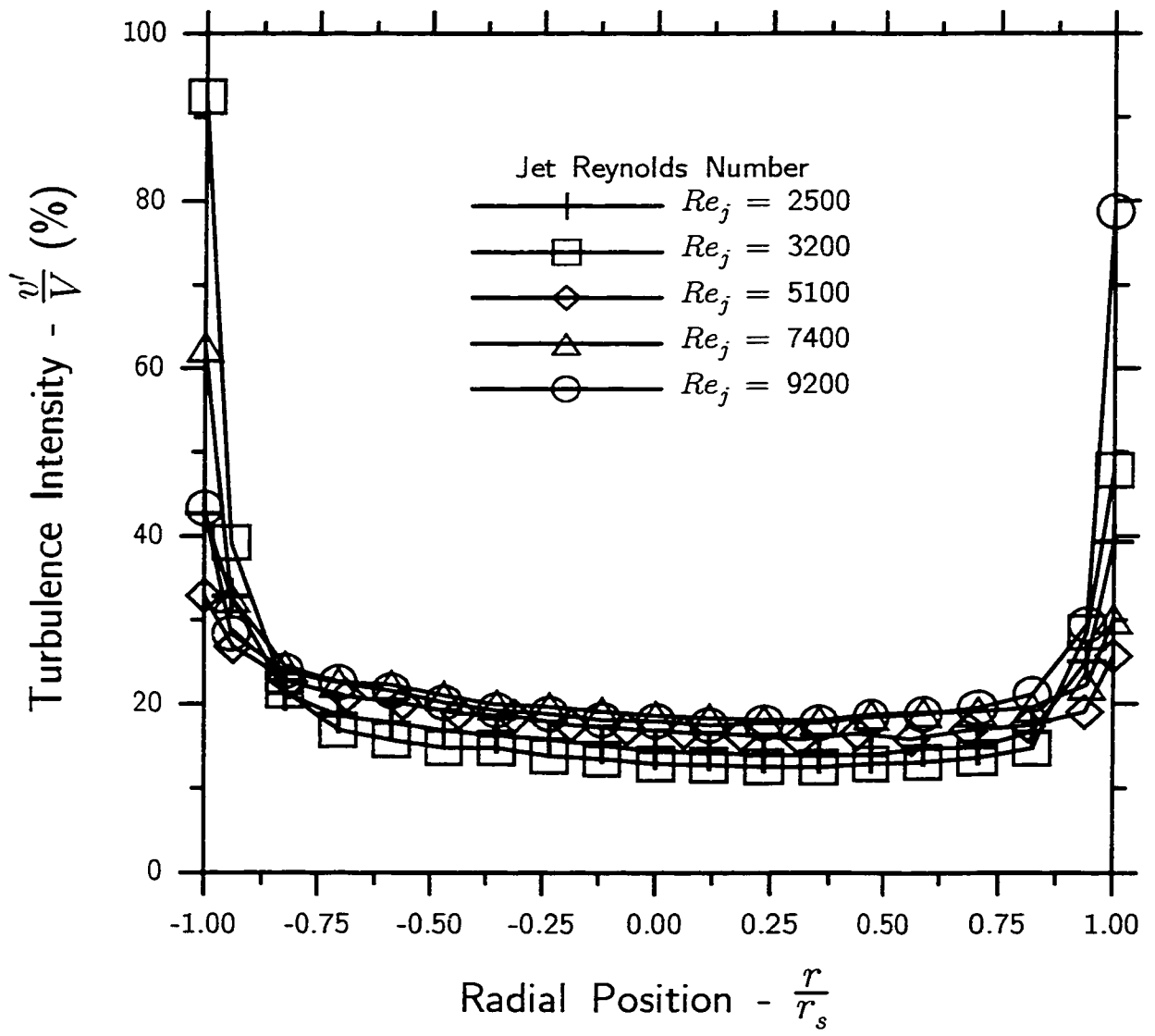Figure A.3: The plug ensures similar jet exit velocity profiles among the different stack sizes for $V_j = 1\,\mathrm{m/s}$.

110

Figure A.4: Turbulence intensity at the stack exit is independent of $Re_j$ over the range considered for the $d_s = 22.1\,\mathrm{mm}$ stack.
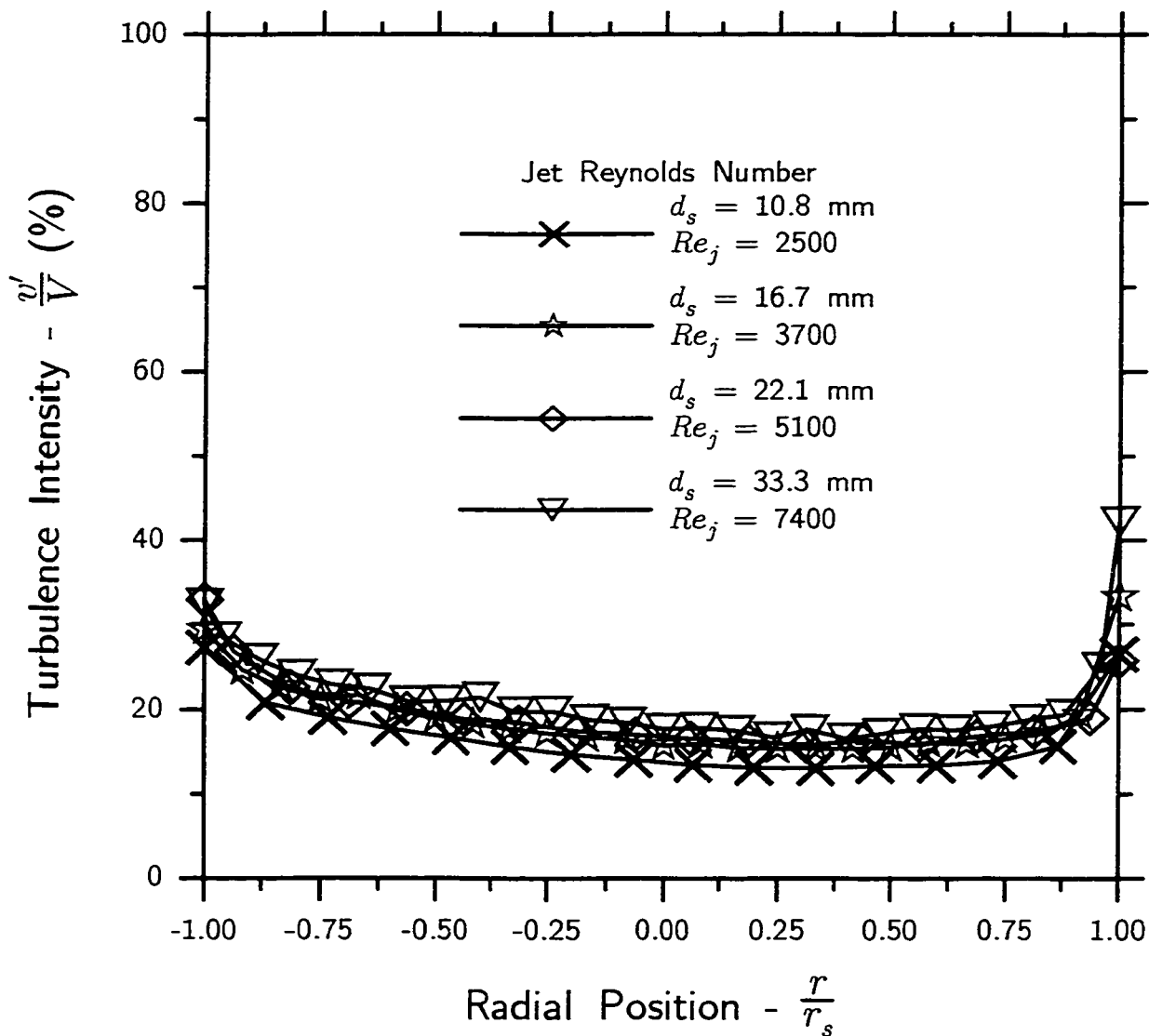
Figure A.5: Turbulence intensity at the stack exit is the same for the different sized stacks because the plugs were placed in the same location relative to the exit and stack size in each case.

# Appendix B

# Difficulties with Geometric Centrelines

One of the problems that has been present in many previous investigations of flame trajectory is the method in which it was determined. Several investigators have used long exposure photographs (e.g., Brzustowski, Gollahalli and Sullivan (1975); Gollahalli, Brzustowski and Sullivan (1975); Huang and Chang (1994)) to determine the centreline trajectory of the flame. Only Huang and Chang (1994) state explicitly that the centreline was found from the geometry of the image, and this is presumably how it was done by the other investigators. The problem with this method is that it is extremely difficult to find the actual geometric centreline from the image, and so a shortcut is typically used, by taking vertical or horizontal 'slices' of the image and finding the centreline based on either of those. Unfortunately these are inherently biasing depending on the co-ordinate system used. Figures B.1 (a) and (b) show some of the problems associated with this method, for the geometry of the flames in question. Figure B.1 (a) shows that the apparent trend can change substantially depending on whether vertical or horizontal slices are used. The trajectory defined by the vertical slices appears to be nearly linear along its entire length (as suggested

by the model), and even lines up with the peaks of some of the contours of flame occurrence probability. The trajectory suggested by the horizontally based centreline is somewhat different. The trajectory follows the cross flow for about the first third of the flame length, after which point, the flame rises linearly, like that of the vertical slices, only at a noticeably higher rate. Part of the difficulty is determining which, if either, of these reasonably represents what is actually occurring.

Figure B.1 (b) shows a second problem with these methods: flame trajectory will be dependent on the contour of flame occurrence probability at which it is determined. Unlike the previous case, both horizontally and vertically based centrelines show similar trends over much of the flame. As the tip is approached, however, both bend upwards, but at different places, because of the different shapes of the upper and lower surfaces towards the flame tip. If one considers either case individually and visualises the resulting trajectory if the 50 % contour is used, instead of the 10 % contour, it can be expected that the upturn of the trajectory will happen nearer the stack. This cannot be the case in reality, however, because the flame does not know which contours the investigator is using to determine the centreline!

The choice of defining centreline on the scalar property of the probability of flame occurrence (as described in Chapter 2) eliminates these problems.

# References

Brzustowski, T. A., Gollahalli, S. R., and Sullivan, H. F. (1975), The Turbulent Hydrogen Diffusion Flame in a Cross-Wind, *Combustion Science and Technology*, 11:29–33.

Gollahalli, S. R., Brzustowski, T. A., and Sullivan, H. F. (1975), Characteristics of a Turbulent Propane Diffusion Flame in a Cross-Wind, *Transactions of the CSME*, 3(4):205–214.

Huang, R. F. and Chang, J. M. (1994), The Stability and Visualized Flame and Flow Structures of a Combusting Jet in Cross Flow, *Combustion and Flame*, 98(3):267–278.
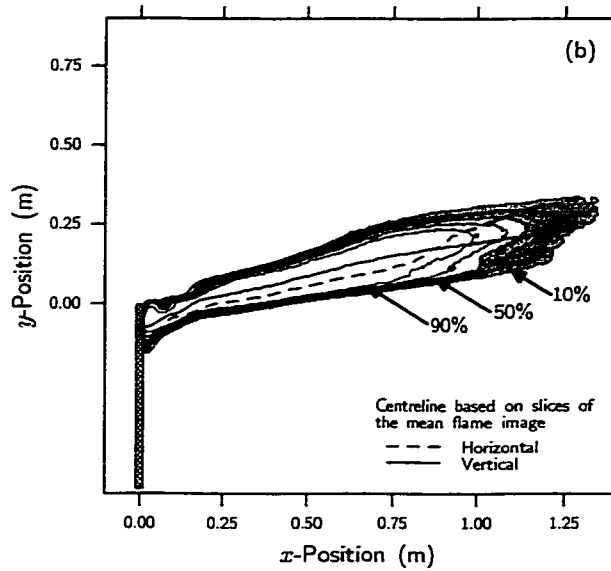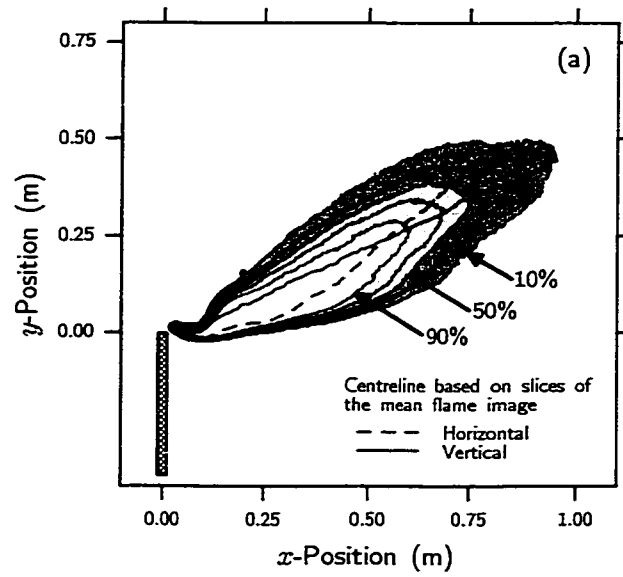
Figure B.1: Geometric centrelines are found by the midpoint of horizontal and vertical slices of the mean flame image at the $10^{th}$ percentile contour. These methods suggest inconsistent trends in flame trajectory for different flame geometries. (a) $R = 1.25$; (b) $R = 0.219$.

# Appendix C

# A Technique for Measuring the Length of a Flame

This appendix is meant to walk the reader through the processes of determining flame trajectory and flame length. The image processing techniques are discussed and the choices made are rationalised. All examples come from the same case used in defining flame trajectory (Figure 2.11) and flame length (Figure 2.12).

## C.1 Distinguishing Flame from Background

Images of the flame were collected with a monochrome analogue CCD camera. The output signal from the camera was digitised to 10 bits and saved in digital form, as described in Chapter 2. The resulting data files were simply a list of the light intensities, ranging from 0 for no signal to 1023 for overload, for each pixel in the camera. The first step in finding the flame trajectory was to look at the recorded data and determine which part of the image represented flame, and which did not. Figure C.1 shows the process of that determination. Figure C.1 (a) shows the cumulative distribution of the number of pixels with threshold intensity choice. The data show what is expected from a high contrast image: two regions which are relatively insensitive

to threshold choice, with a relatively steep gradient between them. The first plateau (i.e., at low intensity) represents the combined areas of the background and the flame. At higher threshold choices, the background no longer shows up, and only the flame remains. The ideal choice for a threshold then, is the point at which the background is no longer in the image, but most of the flame remains (because flame area does decrease as higher thresholds are chosen). To help find this point, this flame area distribution curve is processed to find its derivative (i.e., the rate of change of flame area with threshold choice) as shown in Figure C.1 (b). This derivative was then normalised with flame area in Figure C.1 (c) to give the rate of change as a fraction. The choice of threshold was based on this marginal change and was chosen to be the intensity at which the change of flame area with threshold choice is less that 1.0 %. As shown in Figure C.1 this threshold typically captures the entire flame, and very little background. The choice of 1.0 % may depend on the ambient light conditions, but worked well in this situation.

## C.2   Determining Flame Trajectory

As described in Chapter 2, a threshold is determined and applied to each of the images in the set. The mean flame image is the sum of these binary images, to result in an image where pixel intensity varies from zero to the number of constituent images indicating the probability of flame occurrence at that point. Contours were mapped to different regions of probability of flame occurrence in Figure 2.11 and it was decided to use the peaks of these contours to describe the trajectory of the flame.

Accurately and reliably finding these 'peaks' was not a trivial matter. Since the term peak has the connotation of representing a local minimum in curvature, this

condition was chosen to define the peak of a contour. Looking at the contours in Figure 2.11, three main 'peaks' can be observed: one at the exit of the stack, one at the bottom of the wake trapped part of the flame, and one at the tip of the flame. Since only the tip of the flame was of interest, the regions near the stack were not considered in the analysis. This present two questions: how much of the remaining part of the flame should be considered and what type of equation should be used to describe this remaining contour.

Again, looking back to Figure 2.11 and covering up the quarter of the flame nearest the stack, one can, will little imagination, imagine fitting a polynomial to the remaining part of the flame. This is a reasonable idea, both because the shape lends itself to being described by a polynomial, but also because depending on the order of the polynomial, it can describe fairly complex geometry. Figure C.2 shows how two different order polynomials conform to the contour near the tip of the flame. The 4$^{th}$ order polynomial 'fits' the data better than the parabola, and chooses a flame tip nearer the actual. The problem with the higher order polynomial can be seen away from the tip, closer to the limits of the fitted data. On the lower surface of the flame, the fitted curve begins to turn in on itself, but this effect is not seen in the parabola. It is most likely an effect of combination of the high order polynomial and the parametric form of the equation. Having this added curvature allows for a better fit, but there is now also the chance that this end curvature will be greater than that at the peak, and the wrong location will be chosen if the decision is based only on curvature. For this reason, a parabolic parametric equation was chosen to describe the curvature of the contour.

In Figure C.2 the reliability of the parabolic equation was illustrated, but it also underestimated the flame length. Figure C.3 illustrates how this limitation can be

overcome. Figure C.3 shows how using different amounts of the contour for fitting affects the determined location of the flame tip. The choice of how much of the contour to use was based on the flame length, which was approximated by creating a chord between the left and rightmost pixels on the contour. For the 3/4 case then, 3/4 of the way along the flame length chord from the tip of the flame, the contour was cut by a ray extending normal to the flame length chord. As illustrated in Figure C.3, as less of the contour was used, the parabola more closely approximated the tip of the flame, and a more accurate location for flame tip was chosen. The 1/8 of contour fitted curve represents the case used for the entire data set. It was determined that this most accurately represented the tip of the flame for a variety of flame shapes. At the limiting case (i.e., as the portion of the contour used approaches zero), not enough data would be available for a good 'fit', and the peak could end up in the noise at the tip of the flame.

The trajectory of the flame was then found by connecting the peaks of the contours as described in Chapter 2 and illustrated in Figure 2.11.

## C.3  Determining Flame Length

In Chapter 2 it was stated that flame length was defined at the 10th percentile contour. Figure C.4 illustrates the dependency of flame length on the choice of this contour. As expected, flame length decreases as it is defined at contours of higher probability of occurrence. Over much of the range, the relationship between the two even appears to be linear, except near both extremes. The regularity of this relationship suggests that flame length could be reasonably extrapolated out to a probability of zero percent occurrence for an extreme case scenario. The choice of 10 % was made, however,

because as indicated above it is a statistically representative point, and it still falls on the linear part of the curve. There is not enough data to be able to tell whether or not the departure from linearity at small percentages of flame occurrence probability exists or not.

Figure C.5 shows that instead of extrapolating flame length to zero percent of flame occurrence probability, it was extrapolated to a threshold of zero intensity. The processing required for this was somewhat different that for determining flame trajectory. Instead of calculating an optimum threshold as described above, a series of constant thresholds were applied to the data. The lower bound for these thresholds was 300, which was well out of the region where there was still background in the image. Flame length was then extrapolated from this series as illustrated in Figure C.5. The advantage of this approach is that it eliminates the difficult to optimise, light dependent experimental variables, like camera settings. It also provides a more robust measurement of flame length for repeatability of experiments in different locations, or with different equipment.
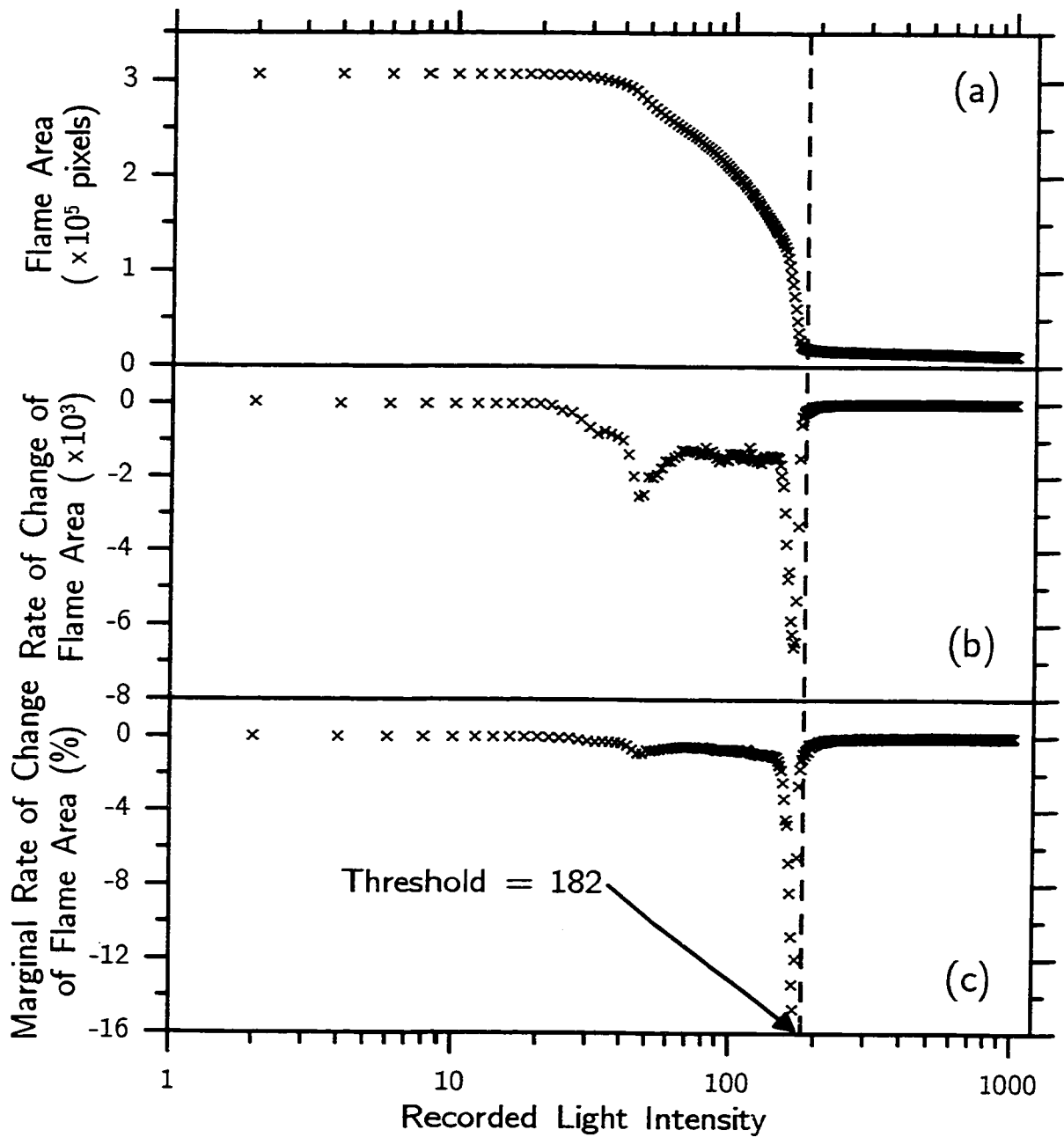
Figure C.1: The 3 trends of interest in choosing a threshold: (a) apparent flame area as a function of threshold; (b) the rate of change of flame area with threshold, the derivative of (a); (c) the marginal rate of change of flame area with threshold. The threshold is defined where the marginal rate of change of flame ares is less than 1.0 %.
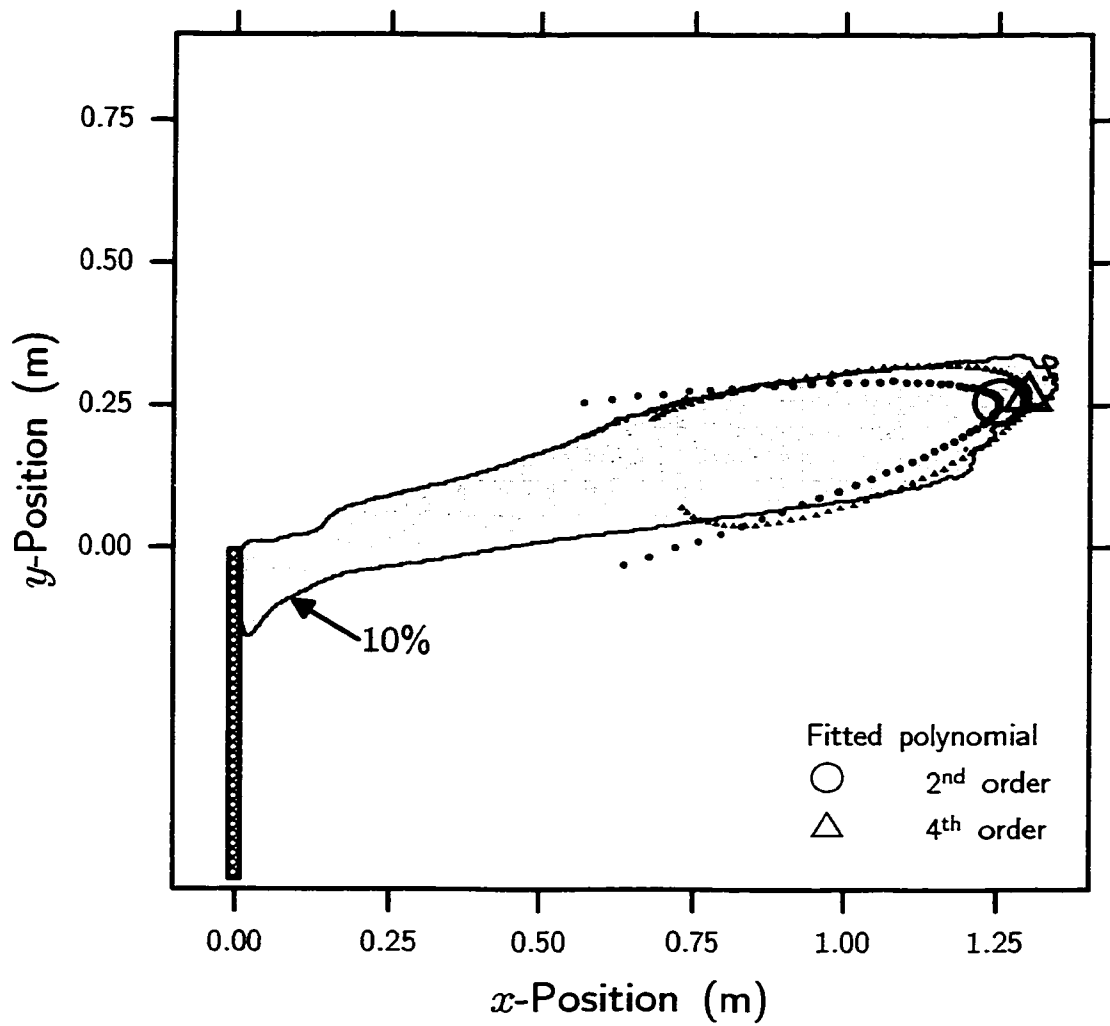
Figure C.2: Higher order polynomials more accurately conform to the contour of flame occurrence probability, but introduce artifacts that may influence the results. A parabola is fitted to the contours to find the peak.
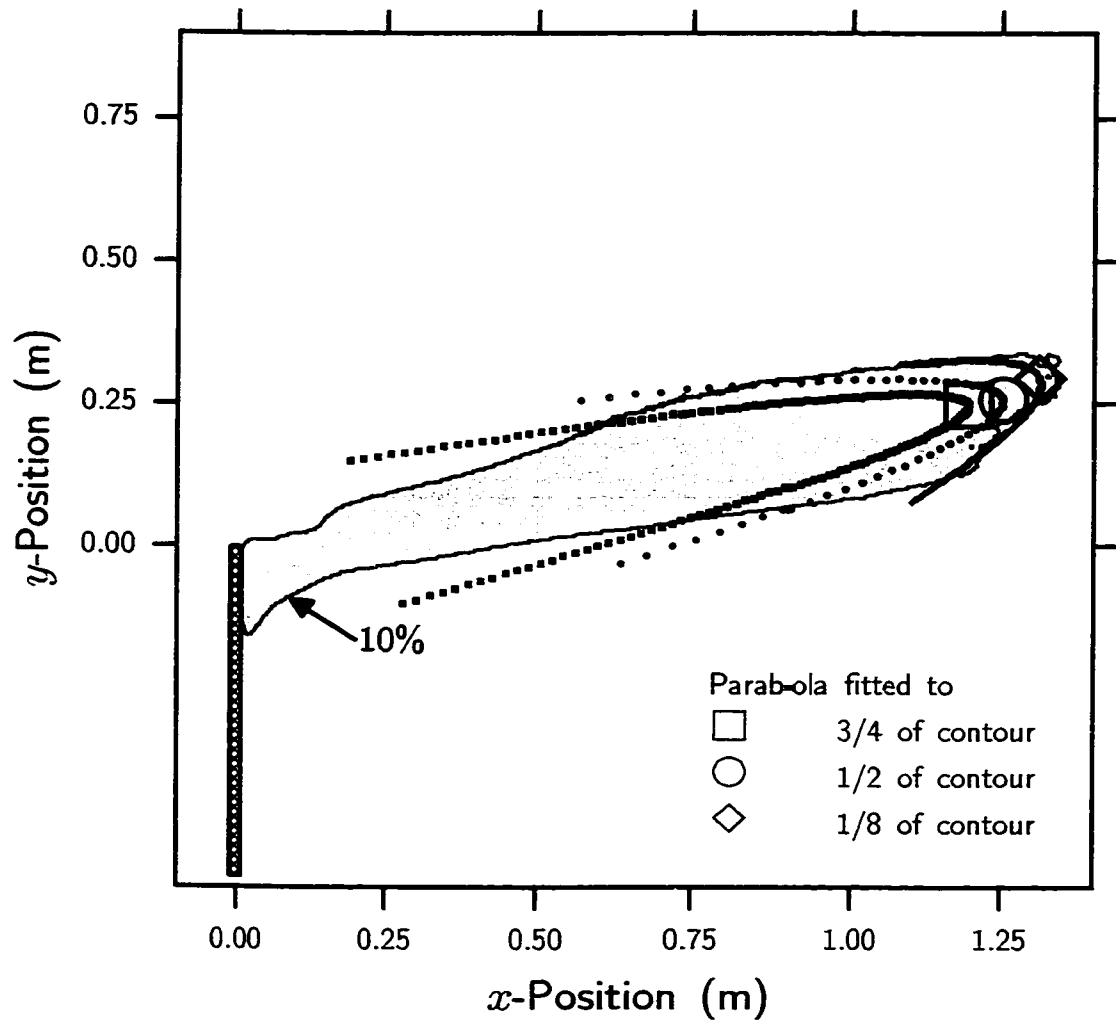
Figure C.3: The calculated position of the peak of the contour becomes more accurate as less of the contour is fitted with the parabola. In the extreme, however, there is not enough data for a good curve 'fit'. 1/8 of the contour is fitted with a parabola in practice.
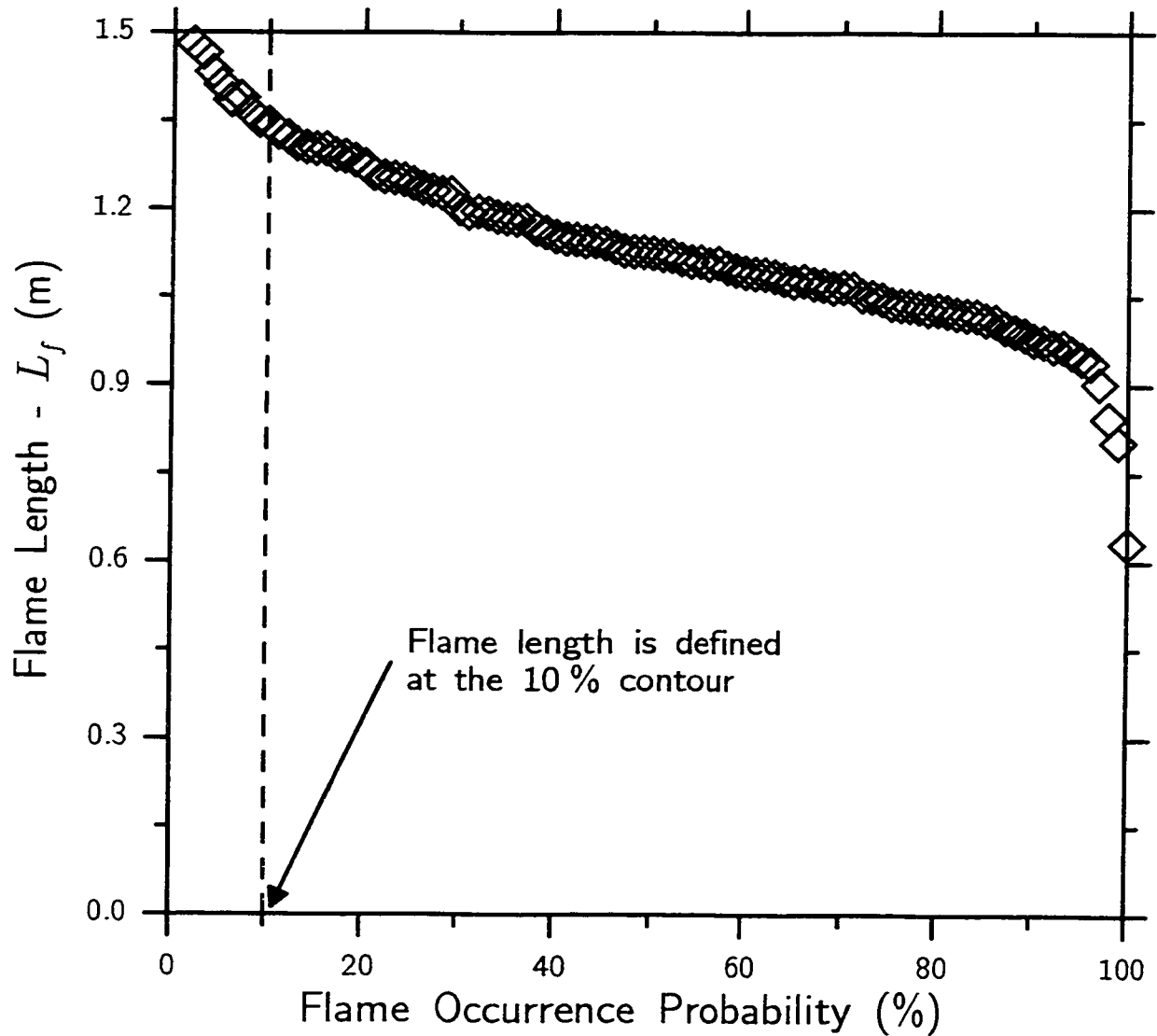
Figure C.4: Flame length decreases linear as it is defined at contours of higher probability of flame occurrence, except at very high and very low probabilities. Flame length is defined at the 10th percentile contour because not enough data is available to determine if the departure from linearity at small probabilities actually exists.
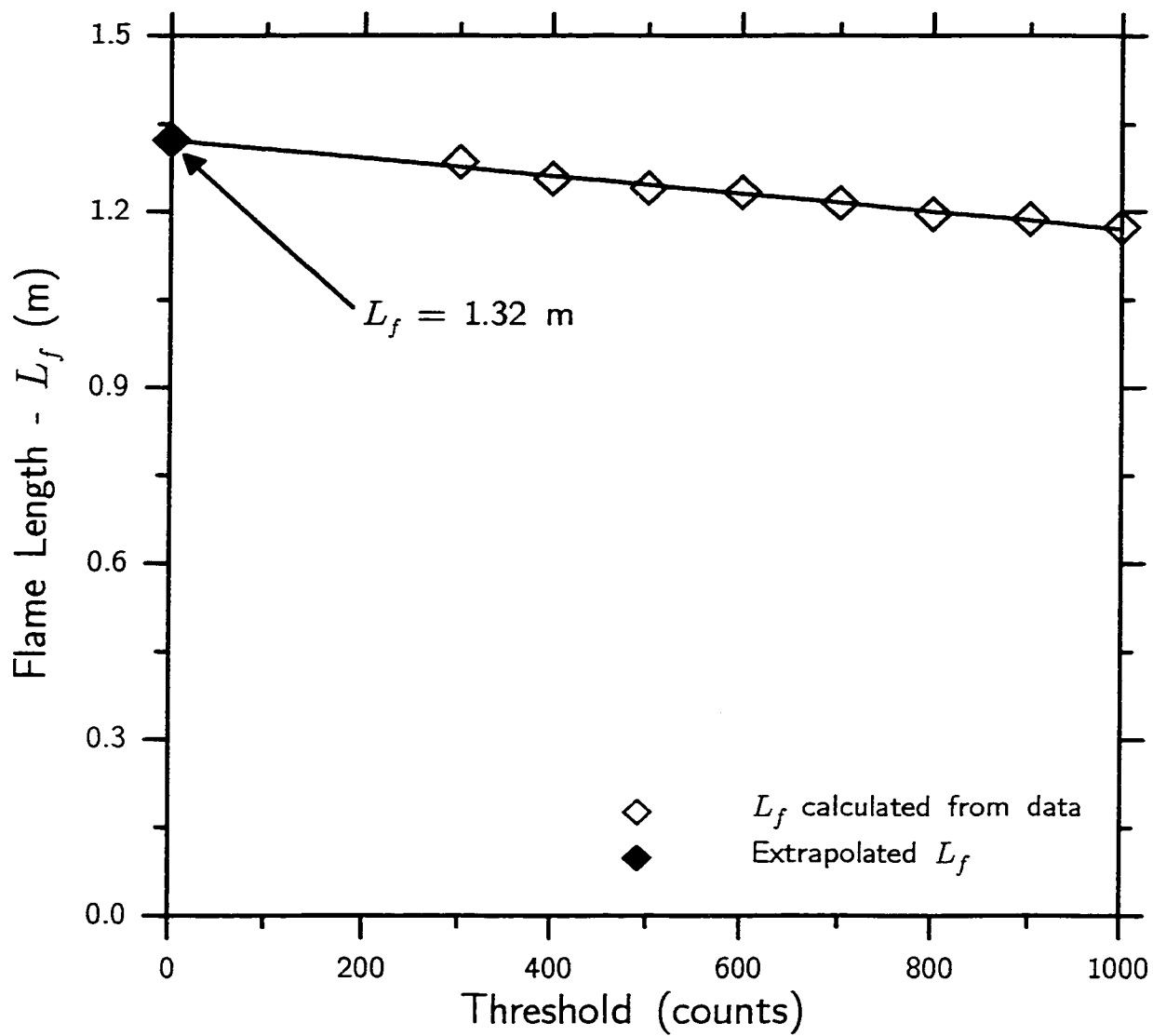
125

Figure C.5: Flame length is extrapolated to a threshold of zero counts.